Title

Quantum dot heterojunction solar cells: the mechanism of device operation and impacts of quantum dot oxidation

Author

Ihly, Rachelle

Publication Date

2014

UNIVERSITY OF CALIFORNIA,
IRVINE

Quantum dot heterojunction solar cells: the mechanism of device operation and impacts of quantum dot oxidation

DISSERTATION

submitted in partial satisfaction of the requirements
for the degree of

DOCTOR OF PHILOSOPHY

in Chemistry

by

Rachelle Ihly

Dissertation Committee:
Assistant Professor Matthew D. Law, Chair
Professor Reginald M. Penner
Professor Robert M. Corn

2014

DEDICATION

To my family and friends, for all of your support and encouragement.
I especially thank my Parents and Grandparents.

To those dedicated in the development and fight for clean and sustainable energy sources,
for an Earth without lasting and detrimental effects resulting from climate change.

"We, the people, still believe that our obligations as Americans are not just to ourselves, but to all posterity. We will respond to the threat of climate change, knowing that the failure to do so would betray our children and future generations. Some may still deny the overwhelming judgment of science, but none can avoid the devastating impact of raging fires and crippling drought and more powerful storms.

The path towards sustainable energy sources will be long and sometimes difficult. But America cannot resist this transition, we must lead it. We cannot cede to other nations the technology that will power new jobs and new industries, we must claim its promise. That's how we will maintain our economic vitality and our national treasure -- our forests and waterways, our croplands and snow-capped peaks. That is how we will preserve our planet, commanded to our care by God. That's what will lend meaning to the creed our fathers once declared."

—President Barack Obama, Second Inaugural Address, January 2013

TABLE OF CONTENTS

Page

LIST OF FIGURES

LIST OF TABLES

ACKNOWLEDGMENTS

I would like to thank my Ph.D. Advisor, Prof. Matt Law, for his guidance and help throughout my graduate studies. He has encouraged my research and allowed me to grow as a research scientist. His guidance and instruction have been invaluable to the development of my scientific career and I appreciate his patience and dedication.

I would also like to thank Professor Robert Corn and Professor Reginald Penner for serving as my committee members for both my qualifying exam and thesis defense. Both encouraged my edification of the chemistry and physics related to my research projects.

I thank each of the group members of Law Research, especially Dr. Yao Liu, Dr. Markelle Gibbs, Dr. Brandon Mercado, Dr. Sean Seefeld and Jason Tolentino. Their support and assistance at UCI and beyond have been greatly valued.

At the National Renewable Energy Laboratory, I extend out a special thank you to Dr. Joseph Luther, Dr. Matthew Beard, Dr. Sanjini Nanayakkara and Dr. Jianbo Gao for their collaborative efforts in the scanning Kelvin probe microscopy project. All have been there to support and advise me when I collected data for my Ph.D. thesis.

I thank the Department of Energy (DOE, Award DE-SC0003904) and the Center for Advanced Solar Photophysics (CASP), an Energy Frontier Research Center funded by the DOE, Office of Science, Office of Basic Energy Sciences Program for funding the research during my graduate studies.

I also thank the American Chemical Society and ACS Nano for allowing me to reuse parts of "The photothermal stability of PbS quantum dot solids" *ACS Nano* **2011**, *5*, 8175–8186 (http://dx.doi.org/10.1021/nn2033117) in Chapter 2 and Appendix A of this thesis.

CURRICULUM VITAE

Rachelle Ihly

EDUCATION

Ph. D. in Chemistry, 2008–2014
University of California, Irvine
Research Advisor: Assistant Professor Matt Law
Thesis: "Quantum dot heterojunction solar cells: the mechanism of device operation and impacts of quantum dot oxidation"
Research Synopsis:

- **Photothermal stability of PbS quantum dots:** Thin-films of PbS or PbSe quantum dots are utilized as absorber layers in colloidal quantum dot solar cells. Changes in energy levels and doping profiles by quantum dot oxidation and size change and desorption of stabilizing ligands can result in poor device stability in air. For this reason, the photothermal stability of PbS quantum dot thin-films in air and nitrogen was investigated as a function of QD size. A primary degradation mechanism for films exposed to air was determined and is caused by quantum dot oxidation, which manifests changes to the optical band-gap with a unique size-dependence. Stabilization of quantum dots films for all sizes was accomplished by infilling the solid with atomic layer deposition alumina to prevent quantum dot oxidation, providing robust, air-stable films.
- **Solar cell device operation:** In a collaborative effort between UCI and the National Renewable Energy Laboratory, scanning of active cross-sections of ZnO/PbS heterojunction solar cells using scanning Kelvin probe microscopy was accomplished. Solar cell device operation was investigated by measuring the electrical potential and electric field profiles across the junction. Operating band-diagrams as a function of applied bias, illumination, and device architecture were obtained.

Bachelor of Science, Chemistry, 2003–2007
Colorado State University
Research Advisor: Assistant Professor Alan Van Orden
Research Synopsis:

- **DNA hairpin folding:** The objective of the project was to better understand secondary structure formation and folding dynamics of DNA stem-loop hairpins. Fluorescence fluctuation spectroscopy (FFS) was utilized to provide hairpin-folding reaction kinetics over the applicable reaction time scale with fluorescence fluctuations caused by conformational changes between a fluorescent dye and its complementary quencher attached to either end of the hairpin. Our results show hairpin-folding reaction occurs through a three-state mechanism with a partially folded intermediate.

FELLOWSHIPS & AWARDS

- Center for Advanced Solar Photophysics Collaboration Prize, 2014.
- Honorable Mention, National Science Foundation Graduate Research Fellowship Program, 2010.
- Highest honors for undergraduate research presentation at Colorado State University Celebrate Undergraduate Creativity Showcase, 2007.

- National Science Foundation Research Experience for Undergraduates (REU), Colorado State University, 2006.
- Colorado State University President's Forum for Emerging Leaders, 2005.

PUBLICATIONS

- *Ihly, R.*; Nanayakkara, S. U.; Gao, J.; Zhang, J.; Luther, J. M.; Law, M. "Scanning of PbS quantum dot solar cell cross-sections with Kelvin probe microscopy reveals diffusion-based operation" Manuscript in preparation.
- Liu, Y.; Tolentino, J.; Gibbs, M.; *Ihly, R.*; Perkins, C. L.; Crawford, N.; Hemminger, J. C.; Law, M. "PbSe quantum dot field-effect transistors with air-stable electron mobilities above 7 cm^2 V^{-1} s^{-1}" *Nano Lett.* **2013**, *13*, 1578–1587.
- *Ihly, R.*; Tolentino, J.; Liu, Y.; Gibbs, M.; Law, M. "The Photothermal Stability of PbS Quantum Dots Solids" *ACS Nano*, **2011**, *5*, 8175–8186.
- Liu, Y.; Gibbs, M.; Puthussery, J.; Gaik, S.; *Ihly, R.*; Hillhouse, H.; Law, M. "Dependence of Carrier Mobility on Nanocrystal Size and Ligand Length in PbSe Nanocrystal Solids" *Nano Lett.,* **2010**, *10*, 1960–1969.
- Jung, J.; *Ihly, R.*; Scott, E.; Yu, M.; Van Orden, A. "Probing the complete folding trajectory of a DNA hairpin using dual beam fluorescence fluctuation spectroscopy" *J. Phys. Chem. B,* **2008***, 112,* 127–133.

CONFERENCE & POSTER PRESENTATIONS

- **Conference Talk**: Ihly, R.;Nanayakkara, S. U.; Gao, J.; Zhange, J.; Luther, J. M.; Law, M. 2014 Spring Materials Research Society Meeting "Scanning of active colloidal quantum dot solar cell cross-sections reveals mechanism of device operation" San Francisco, CA: April, 2014.
- **Conference Talk**: Ihly, R.; Nanayakkara, S. U.; Gao, J.; Zhang, J.; Luther, J. M.; Law, M. 2013 Center for Advanced Solar Photophysics Annual Meeting "Scanning Kelvin probe microscopy of active ZnO/PbS heterojunction solar cells" Los Alamos, NM: July, 2013.
- **Conference Talk:** Liu, Y.; Mercado, B. M.; Ihly, R.; Gibbs, M.; Tolentino, J.; Law, M. 2012 Center for Advanced Solar Photophysics Annual Meeting "Lead chalcogenide quantum dots: towards longer carrier diffusion lengths and enhanced photocurrents" Golden, CO: August, 2012.
- **Conference Talk:** Ihly, R.; Tolentino, J.; Gibbs, M.; Law, M. 242nd ACS National Meeting, "Photothermal oxidation of PbS quantum dots" Denver, CO: August, 2011.
- **Poster:** Jung, J.; Ihly, R. "Conformational Dynamics of DNA Hairpins using Fluorescence Fluctuation Spectroscopy" Celebrate Undergraduate Research and Creativity Showcase, Colorado State University, Fort Collins, CO: April 2007.

RESEARCH EXPERIENCE AND SKILLS

Department of Chemistry, University of California, Irvine, Irvine, CA

Graduate Researcher, 2008–present

Laboratory Skills:

- Synthesized inorganic colloidal quantum dot nanocrystals (PbX quantum dots, with X = S, Se, and Te) using air-free, Schlenk-line techniques to create quantum dot solutions for thin-film processing and opto-electronic device fabrication.
- Fabricated thin-film PbS and PbSe field-effect transistors to measure carrier mobility and characterize *p*- or *n*-channel behavior.
- Fabricated and characterized ZnO/PbS heterojunction solar cells for evaluation of photovoltaic efficiency at 1-sun illumination.
- Determined the effect of intense UV light, air, and heat on the optical absorption of thin-films of PbS quantum dots treated with 1,2-ethanedithiol as a function of quantum dot size.
- Demonstrated the activated nature of oxidation by exposing nanocrystal solids to oxygen at low temperatures (~80 K) in a liquid nitrogen cooled cryostat.
- Improved the photo-thermal stability of PbS quantum dot thin-films in air by using low-temperature atomic layer deposition of alumina to protect against quantum dot oxidation.
- Prepared active cross-sections of ZnO/PbS heterojunction solar cells for study with scanning Kelvin probe microscopy to characterize operating band diagrams as a function of applied bias, illumination, and PbS layer-thickness.
- Comprehensive skill-set includes: atomic force microscopy, scanning electron microscopy, X-ray diffraction, UV-vis, Fourier transmission infrared-spectroscopy, steady state photoluminescence, inorganic nanocrystal synthesis, thin-film deposition: spin-coating and dip-coating, contact metal evaporation, and glove-box and laboratory maintenance.

Communication Skills:

- Presented research progress on a weekly basis in a clear and concise manner to communicate research progress and difficulties to group members and advisor.
- Quarterly presentation of research progress and pertinent literature results given to group members and research advisor in a formal presentation setting.
- Lead a collaborative effort between UCI and the National Renewable Energy Laboratory to study the mechanism of device operation of ZnO/PbS heterojunction solar cells with scanning Kelvin probe microscopy. Quarterly research progress presentations were organized and presented via teleconference.

TauTheta Instruments, LLC, Boulder, CO
Chemist I, 2008
Laboratory Skills:

- Performed quality control and validation testing of an optical oxygen sensor developed as a commercial product for industrial or research-based settings.
- Designed and executed validation tests including sensor accuracy, sensor lifetime, and response time for the optical gas sensor.

Communication Skills:

- Effectively presented weekly validation updates to communicate progress results and research challenges to various stakeholders including parent company, In-Situ, Inc., and product vendor, Thermo-Fisher Scientific.

Department of Chemistry, Colorado State University, Fort Collins, CO
Undergraduate Researcher, 2005–2007

Laboratory Skills:

- Prepared single-stranded DNA salt solutions for study with fluorescence fluctuation spectroscopy.
- Acquired fluorescence fluctuation spectroscopy measurements to study single stranded DNA hairpin folding reaction as a function of solution salt concentration and flow rate to determine the kinetics of the folding reaction.
- Manipulated lasers, optics, and photon detectors to achieve and maintain experimental setup to study relaxation dynamics with fluorescence fluctuation spectroscopy.

Communication Skills:

- Presented weekly research updates to fellow collaborators of the National Science Foundation Collaborative Research in Chemistry.
- Received highest honors for presenting my undergraduate research at the Colorado State University Celebrate Undergraduate Research Showcase.

ORGANIZATIONS AND COLLABORATIONS

- UCI Representative for Young Investigator Committee, Center for Advanced Solar Photophysics: Young Investigator Committee, 2012–present.
- Member, American Solar Energy Society, 2011–2012.
- Secretary, Iota Sigma Pi National Honors Society for Women in Chemistry, Calcium Chapter, Irvine, CA 2011–2012.
- Treasurer, Iota Sigma Pi National Honors Society for Women in Chemistry, Calcium Chapter, Irvine, CA 2010–2011.
- Member, Energy Frontier Research Center: Center for Advanced Solar Photophysics (CASP), 2009–present.
- Member, UCI Center for Solar Energy, 2008–present.
- Member, Iota Sigma Pi National Honors Society for Women in Chemistry, Calcium Chapter, Irvine, CA 2008–present.

TEACHING

Graduate Teaching Assistant, 2009–2011

- Taught general chemistry concepts and laboratory techniques and practices to undergraduate college students enrolled in Chemistry 1LB laboratory.
- Held weekly office hours and regularly responded to student questions through email.
- Received excellent student reviews.

OUTREACH

University of California, Irvine, Irvine, CA, 2009–present

- Organized and assisted children to make their own personal chapstick for National Science Week at the Santa Ana Zoo and UCI Wayzgoose Festival for Iota Sigma Pi National Honor Society for Women in Chemistry.
- Initiated a seminar to be given by Dr. Lori Greene to speak to women members of the Calcium Chapter of Iota Sigma Pi about her career path in renewable energy.

- Participated and assisted in organization of chemistry shows presented to elementary school children by the UCI Chemistry Club. Activities included making slime with borax, glue, food coloring, and water, freezing items such as rubber gloves and flowers in liquid nitrogen, and flaming gummy bears.

Fullerton College, Fullerton CA, 2009

- Organized activities to highlight various renewable energy technologies for college students participating in Science Saturdays GPS2 Project.
- Lead a workshop to explain how solar cells work and aided students in fabricating a titanium dioxide raspberry solar cell in-house to demonstrate the operating principle of dye-sensitized solar cells.

Colorado State University Chemistry Club, Fort Collins, CO, 2005–2007

- Provided scientific outreach to K–12 students by giving science shows at local public schools and the Discovery Science Center. Activities included making ice cream using dry ice, tie-dying clothing items, making slime with borax, glue, food coloring, and water, freezing flowers in liquid nitrogen, and a Harry Potter themed game using acid/base indicators.
- Participated in the transformation of a chemistry lecture hall to appear like a Halloween Haunted House complete with mad scientist show and other science related activities for families in the local community on an annual basis.

ABSTRACT OF THE DISSERTATION

Quantum dot heterojunction solar cells: the mechanism of device operation and impacts of quantum dot oxidation

By

Rachelle Ihly

Doctor of Philosophy in Chemistry

University of California, Irvine, 2014

Assistant Professor Matt Law, Chair

This thesis explores the understanding of the chemistry and physics of colloidal quantum dots for practical solar energy photoconversion. Solar cell devices that make use of PbS quantum dots generally rely on constant and unchanged optical properties such that band gap energies remain tuned within the device. The design and development of unique experiments to ascertain mechanisms of optical band gap shifts occurring in PbS quantum dot thin-films exposed to air are discussed. The systematic study of the absorption properties of PbS quantum dot films exposed to air, heat, and UV illumination as a function of quantum dot size has been described. A method to improve the air-stability of films with atomic layer deposition of alumina is demonstrated. Encapsulation of quantum dot films using a protective layer of alumina results in quantum dot solids that maintain tuned absorption for 1000 hours.

This thesis focuses on the use of atomic force microscopy and electrical variants thereof to study the physical and electrical characteristics of quantum dot arrays. These types of studies have broad implications in understanding charge transport mechanisms and solar cell device operation, with a particular emphasis on quantum dot transistors and solar cells. Imaging the channel potential of a PbSe quantum dot thin-film in a transistor showed a uniform distribution of charge coinciding with the transistor current voltage characteristics. In a second study, solar cell device operation of ZnO/PbS heterojunction solar cells was investigated by scanning active cross-sections with Kelvin probe microscopy as a function of applied bias, illumination and device architecture. This technique directly provides operating potential and electric field profiles to characterize drift and diffusion currents occurring in the device. SKPM established a field-free region occurring in the quantum dot layer, indicative of diffusion-limited transport. These results provide the path to optimization of future architectures that may employ drift-based transport in the quantum dot layer for enhanced charge extraction and power conversion efficiency.

INTRODUCTION

Addressing the energy challenge with clean energy technologies

As part of President Obama's Climate Action Plan, the Obama administration has developed a strategy to combat climate change and achieve energy independence and sustainability.[1] Beginning in 2012, energy imports have declined due to increased domestic energy production as part of a government initiative to relieve dependence on foreign oil. The U.S. will reduce carbon emissions by increasing its renewable energy generation capacity with an additional 10 GW installed by 2020. This target will be accomplished by the expanded use of wind, solar and other renewable energy technologies. Deployment of an additional 25 solar energy facilities, 9 wind farms, and 11 geothermal plants will generate enough power to support 4.4 million homes and ~17,000 U.S.-sourced jobs. Furthermore, the Obama administration has set an impressive goal for the U.S. to become a global leader in energy sustainability achieved with a strong emphasis in solar energy conversion. Research and development budgets for the development of clean energy technologies have increased by 30%, with a total budget of $7.9 billion in 2009.

Renewables such as solar, geothermal and wind do not emit CO_2, a powerful and harmful greenhouse gas linked to climate change. Since the industrial revolution, human activities have led to increased CO_2 levels in the atmosphere with emissions primarily from combustion of fossil fuels and coal-fired power plants.[2] In Figure 1.1 taken from the 2013 report from the International Panel on Climate Change (IPCC), an increase in CO_2 emissions is clearly observed along with a concomitant increase in the average global temperature. Increased CO_2 emissions are a primary and well-known indicator of climate change, however, many other metrics have been evaluated including the melting of the polar ice caps, increased sea levels, ocean acidification, and increased concentration of other greenhouse gases such as methane attained from the 2013 report from the International Panel on Climate Change (IPCC).

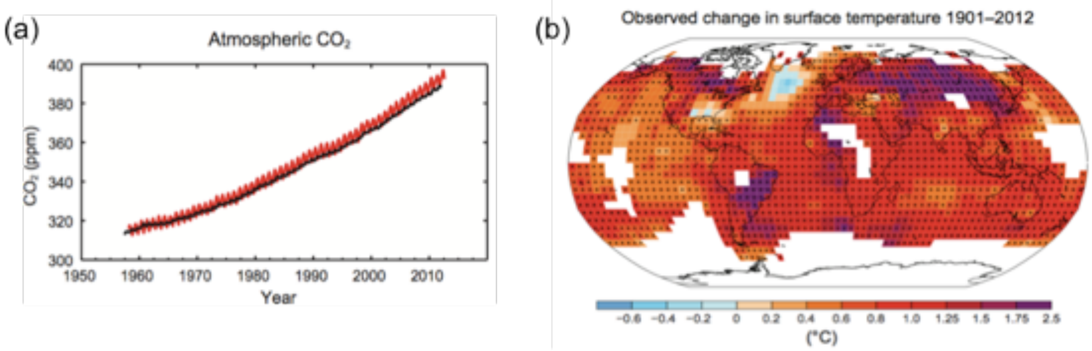

Figure 1.1 (a) Changes in carbon dioxide concentrations in the atmosphere over regions near the equator (red) and the South Pole (black) since 1958. **(b)** Surface temperature changes of the Earth observed over a 100-year period. The average global temperature has risen by 0.6-0.7 °C. Figures are from the International Panel on Climate Change Report, 2013.[2]

The report from the International Panel on Climate Change (IPCC) characterizes the changes for the above listed metrics over time, showing distinct and clear impacts from increased CO_2 levels in the atmosphere and oceans. The technical experts from the IPCC report cede that global warming and climate change is evident and a result of human impact. Continued emissions of green house gases will cause further warming and irreversible changes in climate patterns. Here, projections through the aid of climate models predict a temperature rise of a 1.5 °C by the end of the 21st century taken from the 2013 report from the International Panel on Climate Change (IPCC).[2] This increased temperature change can wreck havoc by disturbing the equilibrium of ecosystems *via* temperature and pH changes. Furthermore, the temperature change can prompt abnormal weather patterns including higher frequencies of hurricanes, drought, and heat waves.[3] In order to avoid these irreversible effects, the IPCC report encourages world leaders and policy makers to dramatically reduce CO_2 emissions to curtail and mitigate effects from climate change. Conventional energy sources such as combustion engines, coal-fired power plants and oil refineries are the major sources of CO_2 emissions in the United States.[4] As a consequence, there is a greater need for energy sources, such as renewables, that do not emit greenhouse gases, thus providing the opportunity to develop clean energy technologies.

In 2001, the total global energy consumption was ~14 terawatts (TW) and is expected to double by 2050, with a demand of ~28 TW.[5] Among the deployed renewables (wind, solar and geothermal) the capture of solar energy presents the largest potential for energy generation, with a theoretical capacity of 120,000 TW striking the Earth each hour.[6] Various ways to capture solar energy include solar thermal, solar fuels or solar photovoltaics (PV).[6] Solar thermal technologies capture incoming solar energy and use it to heat water to varying temperatures for electric power generation. Solar fuels utilize the sun's energy to drive chemical reactions. This technology attempts to mimic the process of natural photosynthesis for methanol fuel production. Another main research thrust involves generation of H_2 fuel through water-splitting reactions that are driven photo-electrochemically.[7] Solar PV generates electricity directly through the conversion of the solar flux to electrical power. The conversion of solar photons to direct electricity provides the opportunity to deploy installations from a local to grid scale (*e.g.* house, solar farm). The scope of this thesis will focus on solar PV technologies.

A solar PV cell employs an absorber material that captures a unique portion of the sunlight spectrum (Figure 1.2). Upon absorption of solar photons, the material forms electrons and holes (absence of an electron), which are efficiently transported and extracted at metal contacts for useful work in an external circuit.[8] The power conversion efficiency (PCE, η) is a metric used to assess the efficiency of converting sunlight energy to electricity.

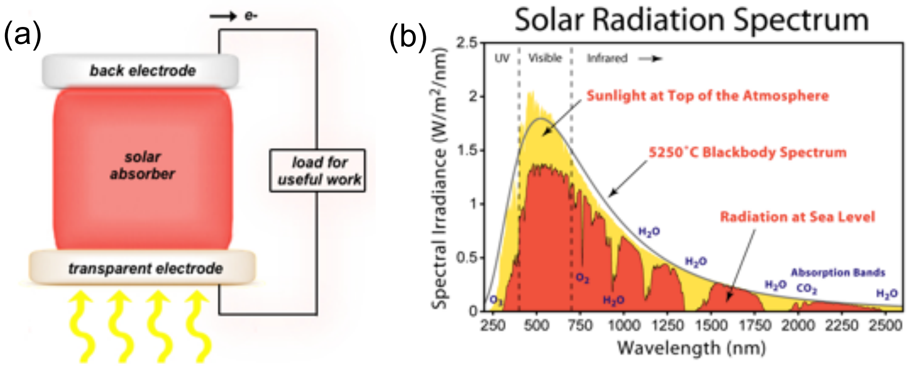

Figure 1.2. (a) Schematic of a simplified solar cell device stack. A solar absorber material is sandwiched between two conducting electrodes. Illumination is incident on the transparent electrode which creates electron-hole pairs in the absorber material. Electrons are separated and extracted at the back electrode for useful work in an external circuit. **(b)** AM1.5G spectrum of the solar flux. The radiation at sea level (red area) is comprised primarily of visible and near-infrared light, thus most solar cell absorber materials are tailored to absorb within this region. Figure is from Wikipedia Commons, http://upload.wikimedia.org/wikipedia/commons/4/4c/Solar_Spectrum.png.

A solar cell creates usable electrical power by generating a net voltage and current under illumination. Engineering energetic or kinetic asymmetry of the device architecture under illumination creates rectifying behavior, such that one type of charge carrier (electron or hole) is collected at an electrode (front or back), thus the behavior of the solar cell can be described as a photodiode. The PCE of a single junction solar cell under 1-sun illumination (AM1.5G, flux = 1000 W m^{-2}) is characterized by V_{OC}, J_{SC}, FF and using Equation 1.1.[9]

$$\eta = \frac{V_{OC} \times J_{SC} \times FF}{P_{solar}} \qquad \textit{Equation 1.1}$$

The open-circuit voltage, V_{OC}, describes the voltage of the cell when the terminals of the cell are disconnected, preventing an electrical current from flowing. The maximum measure of V_{OC} in a solar cell can be attributed to the difference quasi-Fermi level for holes and the quasi-Fermi level for electrons of the absorber material under illumination. The short circuit current density (J_{SC}) describes the amount of current flow per unit area when the terminals are connected with 0 V of applied bias. The fill-factor, FF, is a correction factor to the maximum power the cell can generate ($P = V \times I$), and accounts for non-idealities in current-voltage curves (see Figure 1.3).

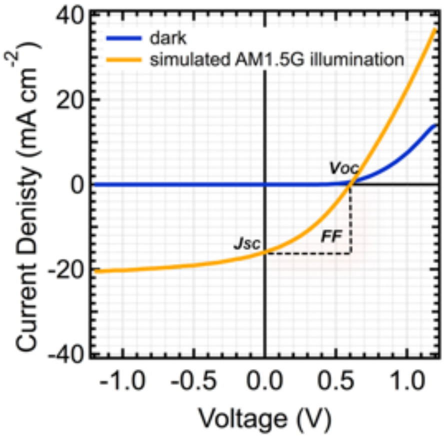

Figure 1.3. Current-voltage curves measured on a solar cell under dark and illuminated conditions using a solar simulator that generates AM1.5G solar flux (100 mW cm^{-2}). The product of the V_{OC} and the J_{SC} is the maximum power of the solar cell. There exists non-idealities in current-voltage curves due to losses of charge carriers through recombination (radiative and non-radiative processes) and resistances in the solar cell stack, including series and shunt resistances. These losses ultimately lead to reduction in overall power. In quadrant IV, the area between the illuminated curve (yellow) and the dashed lines represents this loss in power, thus reducing the efficiency of the solar cell.

The numerator in Equation 1.1 characterizes the power of the solar cell. The overall efficiency of the cell in converting solar radiation into electrical power can be determined by dividing the power of the solar cell by the power of the sun, where P_{solar} is 1000 W m^{-2}. The solar cell in Figure 1.3 has a 602 mV open-circuit voltage, a 16 mA cm^{-2} short circuit current density, and a 35% FF. If the solar cell has a perfect FF (100%), the efficiency would be ~9.6%; however, accounting for the fill-factor, the actual efficiency is 35% of the 9.6%, resulting in a PCE of 3.36%.

Crystalline silicon and other forms were the leading absorber materials in first-generation solar cells.[8,10] These cells were expensive to produce because of the high-temperatures that were required to produce thick films of ultra-pure and defect-free crystalline material resulting in solar cell module efficiencies typically >20%.[11] More recently, development of PV technologies that utilize thin-films of inorganic or organic absorber materials have reduced manufacturing costs while maintaining reasonable module efficiency, ~10-15%. [11] This second generation of PV, nicknamed thin-film PV, uses ultra-thin absorber layer films fabricated at low-temperature using solution processing such as roll-to-roll or inkjet printing.[8,12] Moreover, many of the elements used to form the solar ink are inexpensive, readily available and abundant.[13] The cost of PV installations have declined substantially, but it still remains more expensive relative to other traditional energy technologies.[14] Continuing efforts to reduce cost of solar installations can drive the technology further into full-scale deployment.

Inorganic colloidal quantum dot (CQD) materials offer the opportunity to dramatically boost PCEs. CQDs are attractive for the development of third-generation PV since their solution based syntheses can be utilized in the manufacture of thin-films using roll-to-roll or inkjet printing processes. More importantly, the lead chalcogenide (PbX, X = S, Se, Te) QD family may allow for PCEs to exceed the fundamental limit (33%) for a single junction solar cell which will be discussed in next section.

Lead chalcogenide quantum dots for solar photovoltaics

Capitalization of new and emerging fundamental photophysics may allow for a dramatic increase in PCEs and a reduction of balance of systems cost. The Shockley-Queisser (S-Q) limit of 33% details the maximum and theoretical limit of the PCE at 1-sun illumination for a single junction solar cell containing only one absorber with a band gap of ~1 eV.[15] In addition, the S-Q limit assumes that absorption of one photon leads to generation of a single electron-hole pair. PbX QD nanomaterials offer unique photophysics achieved by the quantum confinement size effect.[16,17] QDs are nanometer sized particles that exhibit quantum confinement. By squeezing a bound electron-hole pair (exciton) below its characteristic radius, the Bohr exciton radius, results in quantum confinement of the exciton. For example, the Bohr exciton radius for PbSe is 43 nm, and typical nanocrystal diameters can be synthesized from 2-10 nm, thus creating quantum confined nanoparticles.[16,18] As a result, QD nanocrystals show unique behavior in their optical and electrical properties differentiated from their bulk counterparts (Figure 1.4). For the PbX QDs, the size effect also results in slower carrier cooling due to formation of a phonon bottleneck; that is, photogenerated excitons cool much more slowly, allowing for the opportunity to collect these carriers before they thermalize.[19] This provides the opportunity to break the S-Q limit through generation of multiple electron-hole pairs per absorbed photon through multiple exciton generation (MEG). Here, MEG violates the assumption in the thermodynamic analysis of the S-Q limit by generating 2 or more electrons per absorbed photon. Theoretical PCEs have been calculated which account for MEG as a function of MEG quantum yield and the maximum theoretical efficiency for PbSe QDs with a band gap ~1 eV is 42%, roughly 10% higher than the S-Q limit.[20] MEG can dramatically improve photocurrents in devices, and has already been measured in actual solar cell that used PbSe QDs as the active layer. Here, the solar cell showed an external quantum efficiency greater than 100% indicating excess electrons were generated per absorbed photon.[21]

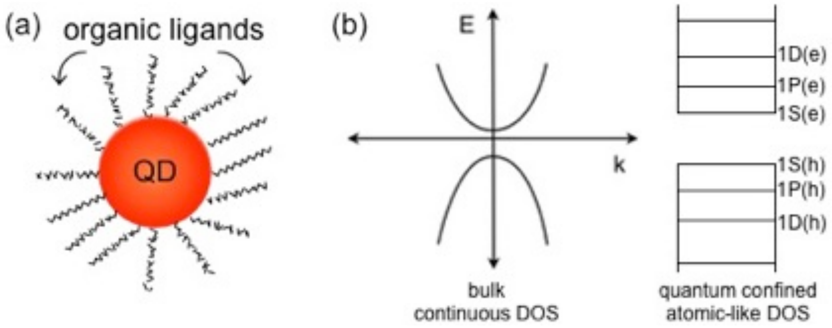

Figure 1.4. (a) Schematic of a QD nanocrystal ligated with long-chain organic molecules that provide solubility and protection against coalescence between other QDs in solution. **(b)** Band structure for bulk *vs.* quantum confined semiconductors. As a result of quantum confinement, discrete energy levels are created. The first optical transition occurs from the 1S(h) to the 1S(e) state and is often referred as the first exciton absorption energy. As the QD gets smaller in diameter, the gap between the 1S(h) and 1S(e) expands due to stronger quantum confinement exhibited by smaller-sized nanocrystals.

The structure of a QD is a nano-sized crystal that is ligated by a shell of organic surfactants that act to satisfy dangling bonds of Pb^{2+} or chalcogen (S^{2-}, Se^{2-}) species at the QD surface and provide solubility in organic solvents such as hexane or octane.[18] The extent of exciton confinement in the QD is characterized by the first exciton peak of absorption, referred to as the first exciton hereafter, and will blue-shift the optical absorption to higher energies with decreasing size of the QD.[22] Thus, the size effect allows for optical absorption and emission properties of QDs to be tuned. Specifically, the optical absorption peaks for PbX QDs can be tuned to the solar spectrum, ranging from 0.9–1.4 eV.

The PbX QDs have achieved much progress in the improvement of their optical and electronic properties,[23] which has garnered strong interest in their use as photoactive layers in solar PV devices. The promising field of "Quantum dot cells" was added to the National Renewable Energy Laboratory Device Efficiency Chart in 2008 under the category of "Emerging PV". Solar cell devices constructed with PbS and PbSe QDs have evolved from architectures that use a Schottky junction[24,25] with metal contacts to a heterojunction between *p*-type PbX QDs and *n*-type semi-transparent metal oxides (*e.g.* ZnO, TiO_2, etc.)[26-29] for reasons discussed in a later chapter. The highest certified PCE achieved for the field is 8.6%,[30] thus showing tremendous progress since the first point on the chart (3%, 2008). Many challenges still need to be addressed which will require a fundamental understanding of the chemical and physical nature of QD doping and surface chemistry and interfaces in device architectures. Furthermore, PbX QDs are air-sensitive materials[31] and air-exposure to QD solar cells has shown detrimental to PV device performance, thus complicating their practical use. Some of the instabilities known to affect QDs include oxidation, size change, and movement or desorption of stabilizing ligands that cover the QD surface. Characterization of these instabilities is necessary to develop methods to counter degradation and extend QD solar cell lifetime in air.

More recently, an intense effort has been devoted towards surface passivation of QDs using small molecule organic or inorganic treatment ligands, typically performed during solid-state film formation. A crucial objective is to understand the influence of the passivating ligands on defect sites at the QD surface, and to find ways to control it. Accordingly, opportunities for fundamental studies to address the many gaps in knowledge are numerous. It will be important going forward to gain a better understanding of how these surface treatments affect QD oxidation, doping of the QD thin-film, and the density of trap states in the optical gap.

Thesis objective and outline

This thesis aims to understand the unique chemistry and photo-physics of PbS QDs and CQD solar cell devices for efficient capture and conversion of solar energy into electricity. In particular, Chapter 2 focuses on the fundamental understanding of QD photooxidation for development of air-stable solar cell devices. In Chapter 3, the use of atomic force and scanning Kelvin probe microscopy to understand the physical and electronic properties of QD solids is covered. In Chapter 3, special attention will be paid in demonstrating SKPM as a powerful tool to understand device physics of transistors. Chapter 4 discusses the progress of the emerging QD solar cell field and provides a brief overview of how QD solar cells are constructed and characterized. Chapter 5 details cross-sectional scanning of QD solar cells to investigate the how applied potentials are distributed throughout the layers in the stack to provide a working picture of how the device operates. Finally, Chapter 6 provides conclusions of this thesis and an outlook for future work.

CHAPTER 2

QD synthesis, thin-films and optical properties

The synthesis of lead chalcogenide (PbS and PbSe) QDs has been accomplished using hydrothermal[32] and solvothermal techniques.[33] Insofar, the hot injection or solvothermal method has demonstrated superior control of nanocrystal size with great monodispersity in average diameter. This method has resulted in highly emissive QDs with desirable electronic properties for opto-electronic applications. In general, rapid injection of a relatively cool precursor solution (typically the chalcogen source) into a hot flask containing a second precursor (usually the lead source) and long chain coordinating ligands dissolved in solution creates suspended colloids of QDs. The precursors rapidly combine to form a supersaturated solution of crystal monomer (Figure 2.1) and the reaction temperature subsequently drops due to a thermal difference between the injection and flask solution. The crystal monomers combine and precipitate out of solution to form nanometer sized crystals that are solvated and stabilized by surface coverage of coordinating ligands such as organic long-chain molecules (typically oleate, $C_{18}H_{33}O_2^-$). The hot injection method achieves monodispersity of nanocrystal size due to the temporal separation of nucleation and growth events.[34,35] The dynamics of nucleation and growth are displayed in Figure 2.1c. At early times (I), rapid combination of precursors gives rise to a supersaturated solution of monomers ($S \geq 1$) resulting in the nucleation event. Upon reaching a critical super-saturation in phase II, a reduction in temperature and monomer supersaturation initiate nanocrystal growth whereby precipitation of nanocrystals is favored. Growth occurs by attachment of monomer to accessible nanocrystal surfaces requiring the dynamic removal and attachment of ligand at the crystal surface. An equilibrium between the rate of nucleation and growth events is achieved at the boundary between phase II and III. During stage III both the monomer concentration and temperature decrease further resulting in very few nucleation events causing a shift to the growth phase. The growth then occurs thermodynamically so that high energy surfaces of small sized crystals are annealed away with the addition of remaining monomer. At later growth times, size focusing or narrowing of the size distribution occurs through an Ostwald ripening process whereby the dissolution of unstable and smaller crystals occurs followed by the growth of larger sized nanocrystals. The resulting QD size and size distribution are dependent on growth conditions including precursor concentrations, reaction temperature, and reaction time.

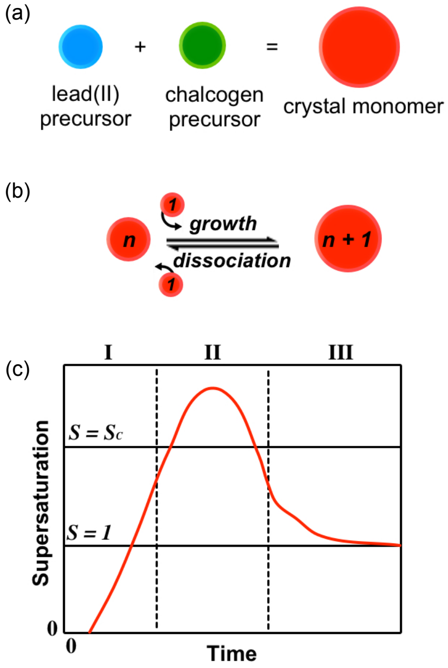

Figure 2.1. Generalized synthesis of semiconductor QDs using a solution-based, hot-injection method. **(a)** Separate solution-based precursors for lead and chalcogen species rapidly combine to produce crystal monomer at the onset of reaction. **(b)** Monomers combine with other monomers to form nanometer-sized colloidal QDs. This reaction is reversible and dynamic, whereby monomers can also detach and re-dissolve in solution. **(c)** Time evolution of crystal monomer supersaturation.

Hines and Scholes synthesized PbS QDs based upon the precipitation of lead and sulfur species (*1*) originating from two separate precursor solutions, the formation of lead oleate from the condensation reaction between oleic acid (OA) and PbO (*2*) and bis(trimethylsilyl) sulfide (TMS) in 1-octadecene.[33] The overall synthesis of PbS using these precursors is displayed in (*3*) and behaves similarly to the scenario described previously with classical nucleation and growth events.

(*1*) $Pb^{2+} + S^{2-} \leftrightarrow PbS_{(s)}$

(*2*) $PbO_{(s)} + 2C_{18}H_{34}O_{2(l)} \longrightarrow Pb(C_{18}H_{33}O_2)_{2(l)} + H_20$

(*3*) $Pb(C_{18}H_{33}O_2)_{2(l)} + ((CH_3)_3Si)_2S_{(l)} \longrightarrow (C_{18}H_{33}O_2)_2\,PbS + (CH_3)_3Si\text{-}Si(CH_3)_3$

Charged oleate ligands coordinate to lead(II) species, which rapidly combine with sulfur to form a PbS crystal monomer stabilized in solution by the organic surfactant. The increased reactivity of TMS relative to elemental sulfur results in generation of highly reactive monomers that can form large sized nanocrystals even in the presence of high concentrations of coordinating ligand (molar ratio 43:2:1 OA:Pb:S). Reducing the molar ratios drastically limits the ability of the coordinating ligand to stabilize the lead precursor, leading to the formation of smaller sized crystals. Furthermore, size control can be achieved by varying the injection temperature; increasing the temperature results in more reactive monomers that react fast and give, on average, larger sized crystals. Additionally, Nair *et al.* have asserted that the interaction between ligands and QD facets, specifically their surface areas and energies along with ligand binding energies to those surfaces, controls the resulting shape of the QD.[36] By adjusting precursor concentration, reactivity of precursor, growth temperature, reaction time, and strength of ligand binding, the size and shape of PbS QDs can be highly tailored using the hot injection method.

Post-synthetic purification and isolation of QDs are accomplished by precipitation with polar solvents, such as ethanol, followed by centrifuging and decanting of the supernatant for removal of unwanted by-products from the synthesis. Re-dispersement of purified QD material in common organic solvents including hexane and octane can provide QD inks for opto-electronic device fabrication.

Casting PbX QDs into thin-films provides a way to incorporate the benefits of the confined energetics of excitons into applied devices. The formation of solid-state QD films from colloidal solutions is commonly performed using layer-by-layer deposition, including spin-coating,[37] Langmuir-Blodgett,[38] and dip-coating.[39] The formation of PbS QD films *via* dip-coating will be discussed here. This technique provides flexibility in terms of control of film thickness (down to the thickness of a single monolayer of QDs), substrate type, solvent system, and ligand exchange treatment. QD thin films are fabricated by alternating between dip-coating a substrate into a solution of dissolved QDs in hexane and a treatment solution containing a short-chain molecule, typically 1,2-ethanedithiol or EDT (Figure 2.2). The motivation to exchange the native oleate ligand with short-chain molecules has been shown to improve film conductivity because the oleate ligands themselves are electrically insulative to the QDs.[39]

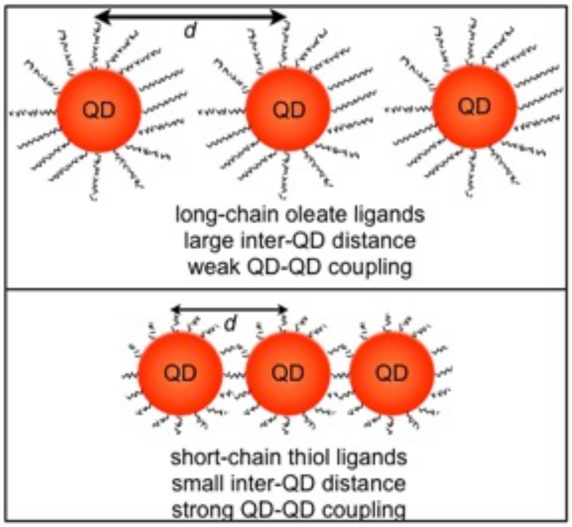

Figure 2.2. Illustration of spherical QDs with long-chain oleate ligands covering the surface. The inter-QD distance (*d*) is too large to enable efficient charge transport from QD to QD. Exchange of the oleate ligand for a short chain thiol molecule, in this case 1,2-ethanedithiol, improves the film conductivity of the QD solid through enhanced coupling of QD wavefunctions and a smaller inter-particle distance.

Film formation involves first immersing a clean substrate of choice into the QD solution which creates a sub-monolayer of PbS QDs that retain their native oleate capping. Dipping this layer into the EDT solution fully removes the oleate capping and replaces it with short-chain EDT molecules. Following treatment, the film is then re-immersed into the QD hexane solution to form a second sub-monolayer of oleate-capped QDs. A second EDT treatment follows and this process is repeated until the desired thickness is achieved. The resulting thickness of the QD film depends on solution concentrations for both QD and treatment and the number of dip-coating cycles (one cycle consists of dip-coating into QD solution followed by treatment). In general, increasing the QD solution concentration allows for the thickness of the film to be built up quickly due to more surface coverage or multi-layer formation per dip cycle.

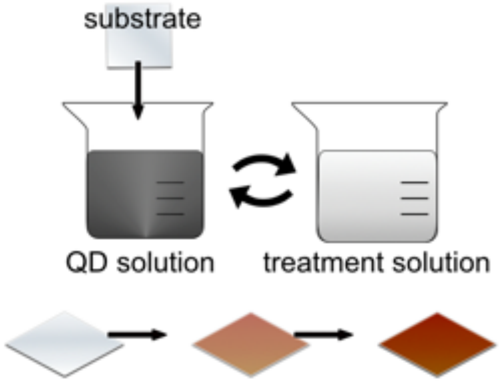

Figure 2.3. Schematic showing dip-coating of a QD film on a glass substrate. A pre-cleaned substrate is immersed first into the QD solution (typically a solution ~2 mg mL-1 of QDs in hexane). After this first dip, the substrate in then immersed in the treatment solution containing a short-chain molecule to remove the native long-chain molecule on the QD surface. This process is repeated a number of times to build up a thick QD layer. The schematic at the bottom illustrates how the substrate changes in color as the QD film gets thicker and thicker with increasing number of dip cycles.

The first sub-monolayer of QDs likely attaches to the substrate via electrostatic interactions between the core of PbS QDs and oriented dipoles on the glass surface. The second layer of QDs may attach via van der Waals interactions between the organic ligands. This statement is supported by observing the preferential coating of the second layer onto the first layer rather than the substrate as shown in Figure 2.4b. In addition, EDT treatment of the first layer may cross-link with the second layer promoting multi-layer formation due to the insolubility of EDT treated PbS QDs in hexane. The ligand exchange process between oleate and EDT is accomplished by mass action due to the relative high concentration of EDT with respect to oleate ligand which causes rapid exchange.[40] The extent of ligand exchange is determined using Fourier transform infrared (FTIR) spectroscopy via monitoring chemical shifts and intensities of functional groups associated with the native and exchanged ligands.[41] Continuous and pin-hole free films with 100 nm thickness or greater can be fabricated using dip-coating.[39] In summary, the formation of uniform and robust QD films can be fulfilled using dip-coating methods with great control of thickness and complete ligand exchange thus rendering it an attractive deposition technique for opto-electronic device fabrication.

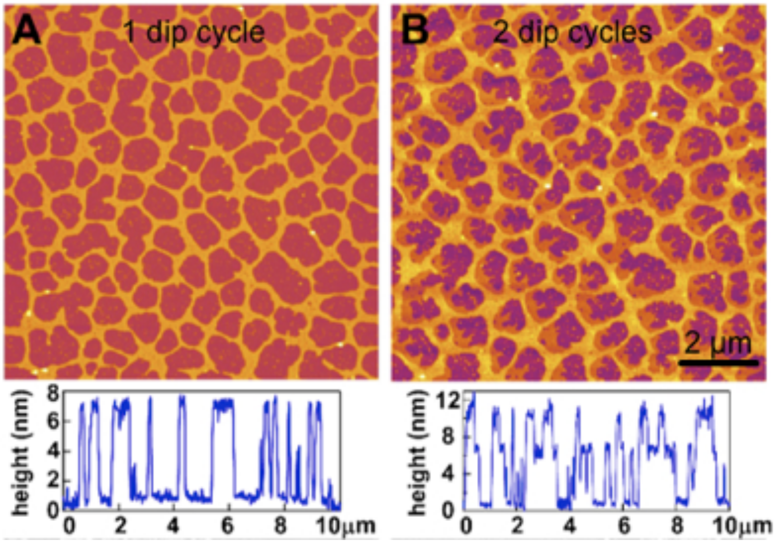

Figure 2.4. Atomic force microscopy (AFM) images of films with ~6 nm diameter PbSe QDs dip-coated onto a silicon substrate using an EDT treatment. It is reasoned that PbS QDs may adopt similar morphologies. **(a)** One cycle of dip-coating results in a sub-monolayer of QDs referenced by the AFM height trace. **(b)** The formation of a QD bi-layer with two full cycles of dip-coating. The dip-coating process is repeated until a continuous 100-nm thick film is acquired. AFM images are 100 μm^2.

To better understand the optical properties of QDs, the wavefunction of the exciton in a quantum dot can be approximated with a particle in a sphere model.[42] The wavefunction of the exciton is confined within the volume of the sphere analogous to the wavefunction of the hydrogen atom. The confinement energy[43] thus becomes discrete and atomic-like according the quantum numbers, n and l, and depends on the inverse square of the sphere radius, a according to Equation 2.1 (m, $\hbar$, and $\beta_{n,l}$ are the mass, reduced Planck constant, and the n,l roots of the Bessel function, respectively).

$$E_{n,l} = \frac{\hbar\beta_{n,l}^2}{2ma^2} \qquad \textit{Equation 2.1}$$

As the particle gets smaller, the energy of the excitonic wavefunction increases due to stronger confinement. Quantum confinement results in discrete energy states for both the electron and hole (refer to Figure 1.4). The first optical absorption peak arises from the transition occurs between the $1S_h$ to the $1S_e$ states and the energy separation between the two gives the optical band gap.[44] For PbX QDs, the optical band gap can be tuned from 0.5−1.5 eV. Generally speaking, the optical properties depend the on the *average* nanocrystal size and shape resulting from the synthesis. The optical band gap has been well correlated with the physical size of the QD by comparing the first exciton energy absorption peak using UV-vis absorption spectroscopy and a statistical analysis of size using transmission electron microscopy (TEM) images of QD sub-monolayers. As the QD size gets smaller and smaller, the first exciton energy will blue-shift accordingly. A Gaussian fit of the first exciton, in units of eV, allows for extraction of the peak position energy and full-width-at-half maximum ($FWHM=2.3548\sigma$) corresponding to the average QD size and size distribution, respectively. The FWHM correlates to the monodispersity of the QD size and provides an overall measure of the sample homogeneity with respect to the spread in both diameter and nanocrystal shape.

The first exciton peak is highly sensitive to the environment of the QDs. Upon creating a solid state film using short-chain thiol molecules causes a red-shift in the first exciton energy relative to the first exciton energy in solution with an oleate capping. Within the literature this has been attributed to enhanced QD-QD coupling resulting in stronger wavefunction overlap between QDs.[45] In contrast, exposure of the QD sample to oxygen environments has been shown to blue-shift the first-exciton energy peak, indicating the average QD size is reduced.[46] The impacts of exposure to air and oxygen to QDs will be discussed next section.

Quantum dot oxidation and its impacts on device performance

Reproduced with permission from *ACS Nano*, **2011**, *5* (10), pp 8175–8186.

DOI 10.1021/nn2033117

QD nanocrystals are inherently metastable materials because they have large surface to volume ratios, whereby interaction of the QD surface with environment and matrix materials (*e.g.* organic long chain ligands, inorganic or organic short chain molecules on the surface of the QD) can alter the optical and electronic properties of the solid.[25,37,47] When QDs are exposed to air, a rapid blue-shift of the first exciton energy is typically observed and indicative of formation of an oxide shell that reduces the average QD diameter.[46,48-50] Primary oxidation shell products for PbS QDs include PbO, $PbSO_3$, and $PbSO_4$.[51] Exposure of solar cell devices that contain QD solids to air results in device failure. Therefore, QD oxidation poses a bottleneck to the practical development of solar cells. In order to develop methods to counter oxidation, fundamental studies that aim to understand spontaneous oxidation of QDs is necessary. Motivated by this, we sought to understand and quantify changes in the optical properties for oxidized and non-oxidized QD solids as a function of QD size.

Most investigations of QD stability have focused on the spontaneous oxidation of PbX QDs in air. These studies show that exposing PbX QD solutions or solids to oxygen results in excitonic blueshifts in absorption and emission spectra. Furthermore, the electronic properties have been shown to be affected by short oxygen exposures resulting in dominant *p*-type doping.[25,31,39,41,52] From these studies, it has been suggested that oxidation consists of two mechanisms (*i*) an initial desorption of EDT and adsorption of oxygen and water that act to increase the hole conductivity followed by (*ii*) the formation of an insulative oxide shell around each QD that gradually decreases film conductivity.[31,53] Photoluminescence quantum yields are also negatively impacted by oxidation due to formation of non-radiative decay states. Furthermore, oxidation of QD solids can modify the engineered electronic[25] and optical properties by creating trap states[46,54] with energies in the optical band-gap and by altering the magnitude of the optical band gap.

Less emphasis has been placed on the effects of heat and light which may exacerbate the oxidation process. QD solutions and solids are expected to ripen and sinter at temperature far below the threshold temperatures for the corresponding bulk materials, driven mainly by reduction of surface energy. The temperature at which a QD solid begins to sinter depends on QD size, packing, surface ligands, and the mobility of both the QD surface atoms and the QDs themselves. Removal of the capping ligands increases the QD surface energy and enables direct QD-QD contact, both of which promote coalescence and grain growth. Recently, van Huis *et al*. demonstrated that hexylamine-capped PbSe QDs rotate, translate, and fuse (sinter) at surprisingly low temperatures (~100°C) during *in situ* TEM heating experiments.[55,56] X-ray scattering studies show that 3D superlattices of 6-8 nm diameter, oleate-capped PbS and PbSe QDs start to sinter at ~230°C and ~150°C, respectively.[52,57,58] Whereas heating QD films in oxygen accelerates oxidation and causes blueshifts in optical spectra (smaller QDs), heating in inert atmosphere results in Ostwald ripening, sintering, and redshifts in optical spectra (larger QDs).[52,59,60] In general, the dense networks of surfaces and grain boundaries within a QD solid promote the diffusion of ligands, QD surface atoms, and even the QDs themselves, particularly during long-term continuous exposures to light, heat, and electric fields (conditions typical for solar cells, for example). Local heating during photothermal (i.e., light and heat) soaking may result in the desorption of ligands and adatoms, inter-diffusion of species across heterojunctions, and chemical reactions within a QD solid. Motion by any of these mechanisms, if unintended, can destroy the functionality of a QD device.

Research objective and strategy

Basic studies are needed to elucidate the most important mechanisms of QD degradation and to develop robust countermeasures if QD solids are to become technologically important materials. Here we use optical absorption spectroscopy and *ex situ* transmission electron microscopy (TEM) imaging to study the effects of heat and UV light on EDT-treated PbS QD solids, focusing on QD size, temperature, and environment (air, 100% oxygen or 100% nitrogen). Long-term stability studies were conducted by exposing QD solids to UV light in air over a period of a month. Additionally, variable temperature studies (in air, 100% oxygen or 100% nitrogen) from 100-360 K were conducted to elucidate the activated nature of the oxidation process. We also employ atomic layer deposition (ALD) of alumina, Al_2O_3, to produce air-stable QD films for environmentally-demanding optoelectronic applications including solar cells. For the purposes of this study, the ALD alumina coating is intended to serve two functions: (*i*) the infilling inhibits diffusion that causes QD ripening and sintering, and (*ii*) the overcoating acts as a gas diffusion barrier to prevent QD oxidation.

Sample preparation, photothermal aging and characterization

QD Synthesis. PbS QDs were synthesized using an air-free method modified from Hines and Scholes.[33] Briefly, PbO (2 mmol) was dissolved and degassed in OA (5 mmol) at 150°C for ~1 hour to form a lead oleate precursor solution. Next, a sulfur precursor solution containing 0.1 M TMS in ODE was rapidly injected into the flask at a specific injection temperature ranging from 120-150°C to yield a dark-brown solution of PbS QDs. Isolation and purification were achieved by precipitating the QDs with ethanol and re-dispersing in hexane a total of four times, typically resulting in ~250 mg of QDs. Size control (2-7 nm diameter) was achieved by varying precursor concentration, injection temperature, and reaction time, yielding QDs with a relatively narrow size distribution of ~10%. Average size and size distribution were determined by analyzing 70-100 QDs in TEM images. PbS QDs with average diameters of 2.9 ± 0.3 nm, 5.0 ± 0.6 nm, and 7.0 ± 0.7 nm were synthesized and used in this study (Figure 2.5a-c).

In Figure 2.5d, the optical absorption spectra show these diameters correspond to a first exciton absorption energy of 1.3 eV, 0.9 eV, and 0.7 eV, respectively, which agree well with published size-bandgap curves for oleate-capped PbS QDs in tetrachloroethylene solution.[16] Absorption FWHMs, which are directly proportional to the size polydispersity of a QD sample, are 134 meV, 88 meV, and 74 meV for the small, medium, and large QDs in solution. Photoluminescence (PL) emission peaks occur at 1.19 eV (FWHM = 210 meV) and 0.87 eV (FWHM = 120 meV) for the small- and medium-sized QDs (emission from the large QDs was too red for our detector).

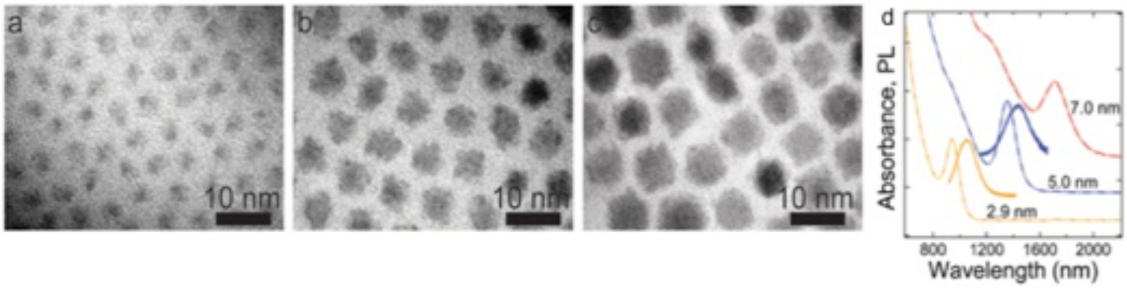

Figure 2.5. TEM images of **(a)** 2.9 ± 0.3 nm, **(b)** 5.0 ± 0.6 nm, and **(c)** 7.0 ± 0.7 nm PbS QDs. Scale bars = 10 nm. **(d)** Optical absorption and photoluminescence (PL) emission spectra of the investigated QD samples in tetrachloroethylene solution. The first exciton absorption energy is 1.31 eV (FWHM = 134 meV), 0.91 eV (FWHM = 88 meV), and 0.72 eV (FWHM = 74 meV), respectively. The PL energy is 1.19 eV (FWHM = 210 meV) and 0.87 eV (FWHM = 120 meV) for the 2.9 nm and 5.0 nm QDs, respectively.

QD Film Deposition. QD films were prepared by dip coating[39] onto glass substrates using a mechanical dip coater (DC Multi-4, Nima Technology) in a glove box with 90 nm thickness.

Briefly, 1.2×1.2 cm^2 glass substrates were cleaned by acetone sonication and an ethanol rinse and dipped alternately into a 2 mg mL^{-1} solution of QDs in hexane and then a 2.5 mM solution of EDT in acetonitrile to make ~100 nm-thick films. Film thickness was measured using tapping-mode atomic force microscopy (MFP-3D, Asylum Research) and SEM (FEI Quanta 3D FEG). Dip coating results in QD films on both sides of the glass. The QD film on the rear surface of each substrate was removed with a razor blade prior to stability testing. The first exciton peak of freshly-made EDT-treated QD films is redshifted relative to QDs in solution because of the increased dielectric constant and substantial electronic coupling in EDT-treated films. Upon film formation, we observed average redshifts of 85 meV, 50 meV, and 15 meV for the 3 nm, 5 nm, and 7 nm QDs, respectively. The peak width varies by 5-10 meV between films, but there is no *average* difference in peak width for QDs in solution and in the solid state.

Characterization. Transmission electron microscopy was performed on a Philips CM 20 operating at 200 kV. Photoluminescence emission spectra of QD samples in TCE were acquired with a Shamrock 500 spectrometer equipped with an iDus InGaAs PDA detector (Andor Technologies) using 514 nm laser excitation. UV-vis absorption spectroscopy utilized a PerkinElmer Lambda 950 spectrophotometer and QD films mounted in airtight optical cells consisting of two mated 1.33-inch UHV ConFlat sapphire viewports. Films mounted in these cells in the glove box show optical spectra that change negligibly after months in air at room temperature in the dark. Integrating sphere measurements and an optical model were used to determine the absorption lengths and absorption profiles of the films at $\lambda = 365$ nm. The measured absorption lengths, $(\alpha_{365})^{-1}$, are 27 nm, 29 nm, and 36 nm for layers of the small, medium, and large QDs, respectively (see Appendix A, Supporting Info). When compared to the thickness of the QD film, these absorption lengths are short. The QDs at the top of the films experience only 2-10% of the UV intensity seen by QDs at the surface of the glass substrate.

Photothermal Aging. For heat and UV soaking studies, QD films on glass substrates were placed directly on a hot plate or a upended handheld UV lamp (1.4 mW cm^{-2} @ 365 nm with illumination through the glass substrate; EL Series lamps from UVP) either in air or a glove box. This UV power density is about one third of that of the full sun AM1.5G spectrum (~4.6 mW cm^{-2} integrated over 280-400 nm). The temperature of samples sitting on the lamp was ~50°C, thus we refer to the combination of light and heat exposure as photothermal soaking. Periodically, each sample was sealed in an airtight ConFlat cell for optical absorption measurements. A curve fitting program implemented in Origin 8.0 was used to extract the first exciton peak position and width.

Variable-temperature UV light soaking (T <300 K) was performed on QD films mounted in an optical cryostat (ST-100 cryostat, Janis Research) inside of a glovebox and then transferred to the benchtop, evacuated, cooled, and backfilled with flowing helium or oxygen (5N purity). A high-flux UV lamp (model B-100AP, UVP) was used to illuminate the films with 3.5 mW cm^{-2} of 365 nm light through a quartz window.

A homemade environmental testing chamber was used to deconvolute the effects of oxygen and moisture on QD films. Films were loaded into the airtight chamber (constructed from a 4.5’’ CF flange, glass viewport, and valved gas lines) inside of a glove box. Humidified gas was made by passing dry oxygen or nitrogen through a water bubbler prior to entering the test chamber. Films were illuminated with a handheld UV lamp in the same geometry as described above. The gas flow rate was controlled with plug valves by monitoring the bubble rate of the exhaust flow.

Atomic Layer Deposition Infilling. To stabilize QD films in air we infilled the QD solid using atomic layer deposition (ALD). Pre-prepared QD films were coated with 15-20 nm of amorphous Al_2O_3 in a homebuilt cold-wall traveling wave ALD system built in a glove box. Deposition was performed at 27°C using alternating pulses of trimethylaluminum and water (40 ms pulse times, 60-120 s purge times, ~0.1 Torr base pressure). Figure 2.6 shows top-down and cross-sectional scanning electron microscopy (SEM) images of a PbS QD film after deposition of 18 nm of ALD alumina at 27°C, compared with a QD film without infilling. These films are similar in thickness and morphology to the films on glass (films on glass proved intractable to image). Elemental depth profiling with X-ray photoelectron spectroscopy (XPS) confirms that the first few nanometers of alumina coat the accessible internal surface of the film to make a three-dimensional PbS/Al_2O_3 inorganic nanocomposite (see Appendix A, Figure S1). Additional ALD deposition eventually seals off the pore network and yields a capping layer of alumina on the external surface of the film.

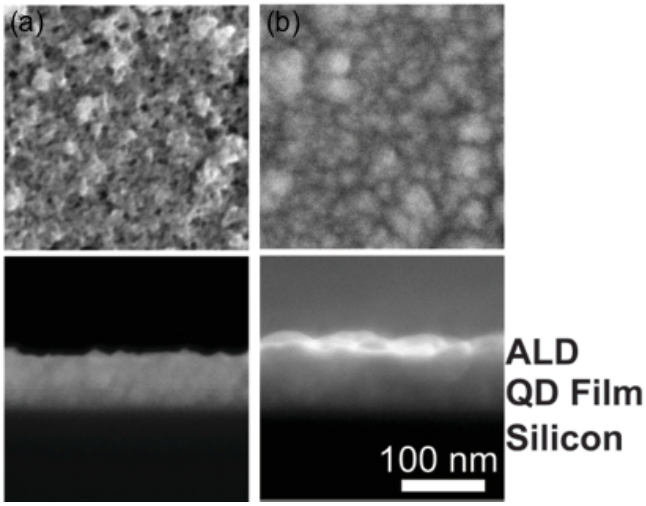

Figure 2.6. Top-down and cross-sectional SEM images of 7 nm QD films before and after ALD. (a) Film without ALD treatment. **(b)** Film with an ALD treatment of Al_2O_3.

ex-situ TEM imaging. For *ex situ* TEM studies, QD sub-monolayers were deposited on SiO_2 membrane window grids (25 nm thick windows, NanoBasic grids, Dune Sciences) using a single dip coating step and EDT treatment. Samples were imaged in the TEM immediately after fabrication, and fiduciary markers were used to relocate and monitor selected regions of each sample over time.

Results and Discussion

Figure 2.7 gives typical absorption spectra for three different films of 5 nm QDs as a function of photothermal soaking time in nitrogen and air (365 nm light @ 50°C). Films soaked in nitrogen exhibit a slow, steady *redshift* and broadening of their first exciton peak, with a total redshift of 46 meV and broadening of 39 meV after one month. Time traces of the peak energy and width (Fig. 2.7d) suggest that the spectral changes have not stopped after one month. In contrast, films in air show a rapid and dramatic *blueshift* (135 meV) and broadening (74 meV) of the excitonic peak within the first week of soaking, followed by only minor changes thereafter. The exciton is nearly washed out by photothermal soaking in air. Control experiments were performed to ascertain the effects of long-term exposure to nitrogen or air (*i*) without UV light or heat and (*ii*) with heat alone (Appendix A, Fig. S3). Films stored in nitrogen in the absence of light and heat showed only a slight redshift (8 meV) and broadening (11 meV), while heat alone caused a slight redshift (8 meV) and significant broadening (28 meV). We therefore conclude that ~85% of the redshift and 25% of the broadening observed in films in nitrogen is caused by the UV flux itself rather than the 50°C thermal bath. Meanwhile, films stored in air in the absence of light and heat exhibited a 95 meV blueshift and 37 meV broadening, consistent with the spontaneous oxidation of PbS QDs at room temperature, while heating in air caused a slow 128 meV blueshift and 41 meV broadening. Based on these results, we believe that none of the blueshift but ~35% of the broadening observed for films in air can be attributed to UV light rather than heating alone. UV illumination certainly intensifies the morphological and chemical changes that occur in the films.

The different aging behavior of films soaked in nitrogen and air implies the action of two distinct aging processes. Films in nitrogen redshift because heating activates diffusion which, in the absence of oxygen, causes the QDs to ripen and fuse (sinter), thereby increasing the average QD size (and size distribution) and relaxing the overall quantum confinement of the system. These films show a steady increase in broadband absorbance as the average bandgap decreases with soaking time (Fig. 2.7a). Soaking a film in air activates diffusion too, but it also enhances the rate of surface oxidation reactions that produce oxidized QDs with smaller PbS cores and greater electronic confinement. The competition between ripening/sintering and oxidation determines whether a QD film exhibits a net redshift or blueshift during photothermal soaking. The 5 nm QD films show a steady and considerable blueshift in air, indicating that oxidation is the dominant process in these films. The considerable decrease in broadband absorbance for films soaked in air (Fig. 2.7b) is a result of the increased average bandgap of the QDs and conversion of a fraction of the film volume to surface oxides.

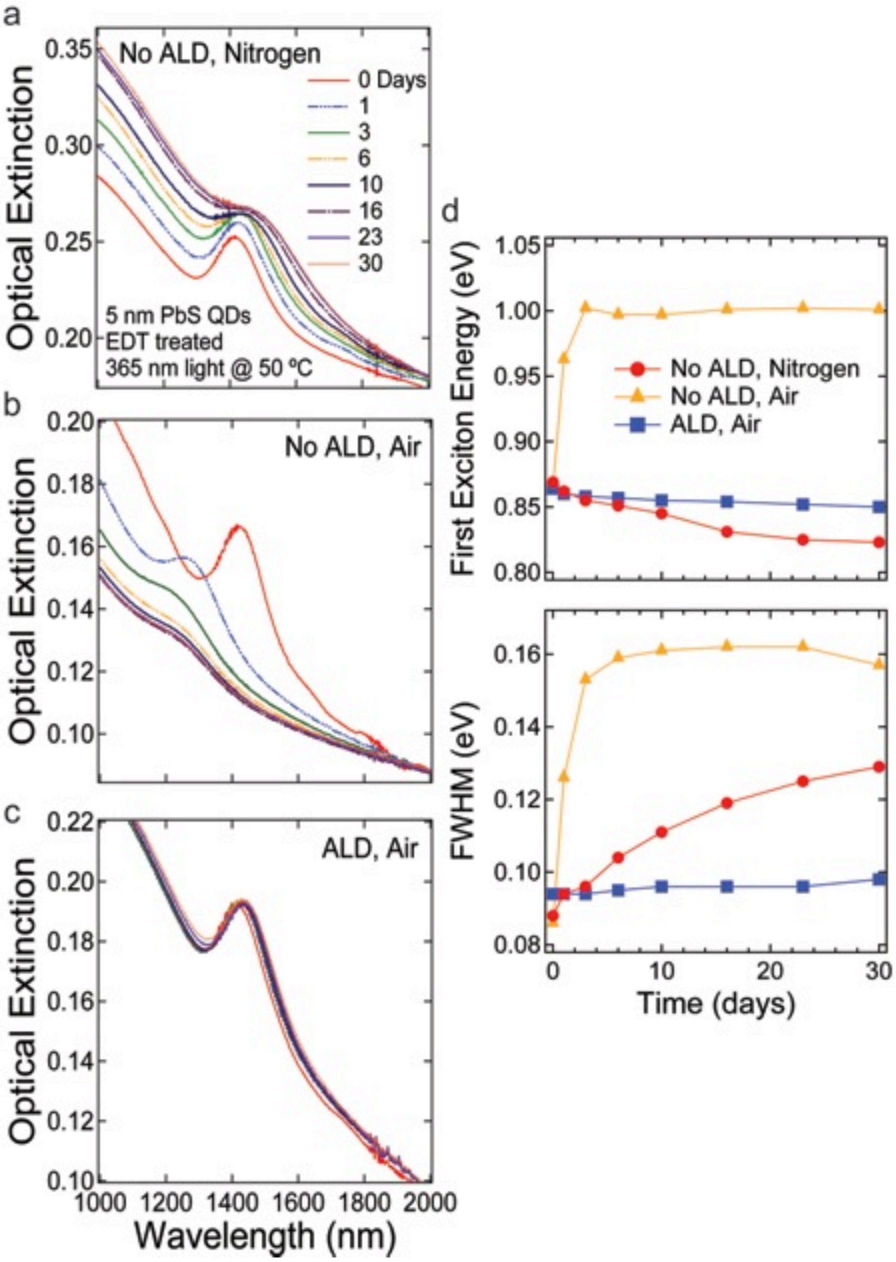

Figure 2.7 UV photothermal soaking of films of 5 nm PbS QDs in air and nitrogen. Typical optical absorption spectra as a function of time exposed to UV light (1.4 mW cm^{-2} @ 365 nm) and heat (50°C) for an untreated QD film in (a) nitrogen and (b) air, as well as (c) an ALD-infilled film in air (18 nm alumina deposited at 27°C). The traces in each graph are offset to overlay at $\lambda = 2000$ nm. (d) Time traces of the first exciton peak energy and peak width for the three films. The first exciton peak of films in air (nitrogen) blueshifts (redshifts) and broadens considerably. The spectra of ALD-infilled films exhibit only a slight redshift (~12 meV) over the first 30 days of photothermal soaking and almost zero peak broadening (~4 meV, compared to ~70 meV for uncoated films in air).

Whereas the excitonic peak shifts one way or the other depending on the ambient gas and other conditions, the peak width – which is proportional to the QD size distribution –consistently increases because (*i*) ripening, sintering and oxidation proceed unevenly within the films, and (*ii*) the UV flux is nonuniform across the thickness of the films (as mentioned above). Both of these effects increase the QD polydispersity.

We can use the known size-bandgap relationship for PbS QDs (Appendix A, Fig. S4) to picture the morphological changes that result from photothermal soaking.[16] This is easy to do in nitrogen because ripening/sintering is the only process that causes large changes in peak energy and width, so redshifts can be related directly to increased QD size. We estimate that the 46 meV redshift observed for 5 nm QD films UV soaked in nitrogen corresponds to a 0.4 nm increase in the average QD size. If this size increase occurs by a combination of Ostwald ripening and sintering, these films should consist of relatively polydisperse, mostly spheroidal QDs mixed with some fraction of sintered ("necked") QDs. This approach is not as useful for films soaked in air because redshifts from ripening/sintering are convolved with blueshifts from oxidation, making it impossible to assign peak shifts to size changes of the PbS QD cores alone; a small peak shift could indicate that a film is either unchanged or sintered and oxidized to equal degrees. If we assume that the 5 nm QD films UV soaked in air experience only oxidation, then the 135 meV blueshift corresponds to a 0.9 nm decrease in the average size of the PbS cores. The neglect of both ripening/sintering and the finite bandgaps of the surface oxides (PbO, $PbSO_4$, etc.) makes this a lower estimate. Despite the limitations, we can successfully use optical spectra to deduce the general morphological changes of films soaked in air. We picture these films as consisting of polydisperse, irregularly-shaped QDs that are heavily contaminated by surface oxides and lightly sintered. This morphology is indeed observed in TEM images of 7 nm QDs soaked in UV in air (see below).

PbS QD films ripen, sinter, and oxidize when exposed to UV light and heat for extended periods of time (*vide infra*). To improve film stability, we use room-temperature atomic layer deposition (ALD) to infill the internal pore network of these films with amorphous alumina and then cap the films with a thin alumina overcoating. ALD is a stepwise chemical vapor deposition method for making thin conformal films on nonplanar substrates with sub-monolayer thickness control, and low-temperature ALD is uniquely suited to growing high-quality films on delicate, topologically complicated substrates.[61-68] ALD has been used to fill the pores of TiO_2 NC films consisting of NCs with diameters as small as 10 nm.[69] More recently, ZnO deposited by ALD at 100°C was shown to penetrate CdSe QD films and increase film conductivity and carrier mobility.[70]

ALD infilling of the 5 nm QD films greatly suppresses photothermal degradation. ALD-infilled films soaked in air showed only a 14 meV redshift and 4 meV broadening after one month, similar to the shifts observed with "no light, no heat" control samples in nitrogen (Appendix A, Fig. S3). The slight redshift suggests that the ALD layer stops oxidation – the film behaves like it is in nitrogen, not air – but does not completely inhibit diffusion within the bulk of the film, either because pockets of the interstitial network are poorly infilled or some diffusion occurs in spite of the ALD coating (for example, at QD-QD necking points that are too narrow for ALD precursor molecules to access). Regardless of this small redshift, it is clear that our ALD infilling method can produce QD solids with greatly enhanced photothermal stability.

We now summarize the behavior of the larger (7 nm) and smaller (3 nm) QD films. The raw data are presented in Appendix A, Figs. S5-S8 and compiled in Table 2.1 along with the results from the 5 nm QDs. Table 2.1 also lists the estimated average size and size distribution of each sample after treatment, as determined from the TEM sizing curve (Appendix A, Fig. S4). Photothermal soaking of 7 nm QD films in nitrogen results in a 16 meV redshift and 32 meV broadening. Control films in nitrogen show a 7 meV redshift and 10 meV broadening in the absence of light and heat, and a 6 meV redshift and 15 meV broadening with heat alone. In air, photothermal soaking causes a very large blueshift (> 156 meV) and broadening (> 105 meV) that completely washes out the excitonic peak after just four days of testing. Control films in air show a 54 meV blueshift and 24 meV broadening without light and heat, while heat alone results in a 77 meV blueshift and 27 meV broadening. ALD-infilled 7 nm QD films are extremely stable in air, showing only a 6 meV redshift and almost zero broadening (~3 meV) after one month of UV exposure.

Photothermal soaking of 3 nm QD films in nitrogen results in a 100 meV redshift and 185 meV broadening. Control films in nitrogen show a 22 meV redshift and 12 meV broadening in the absence of light and heat, and a 42 meV redshift and 50 meV broadening with heat alone. Photothermal soaking in air causes a rapid and pronounced blueshift (124 meV), followed by a slow redshift of 86 meV. The change in peak width is similarly non-monotonic: an initial broadening of 41 meV is followed by noticeable narrowing (8 meV) over the course of the month. Control films in air show a monotonic 146 meV blueshift and 24 meV broadening without light and heat, while heat alone results in a 207 meV blueshift and 47 meV broadening. ALD-infilled 3 nm QD films show a substantial redshift (90 meV) and some broadening (30 meV).

Table 2.1. Effect of Thermal and Photothermal Treatments on Excitonic Peak Energy, Peak Width, Average Diameter, and Diameter Distribution of PbS QD Films.

QD size (nm)	gas	treatment	$\Delta E_{\text{1Sh-1Se}}$ (meV)	ΔFWHM (meV)	$d \pm \Delta d$ (nm)[c]
2.9 ± 0.3	N_2	no UV, -80°C	-2	1	2.9 ± 0.3
	N_2	no UV, no heat	-22	12	2.9 ± 0.4
	N_2	heat only	-42	50	3.0 ± 0.5
	N_2	UV	-100	185	3.3 ± 1.2
	Air	no UV, no heat	146	24	2.5 ± 0.3
	Air	heat only	207	47	2.4 ± 0.3
	Air	UV	124, -86[a]	41, -8[a]	2.7 ± 0.3
	Air	***ALD, UV***	**-90**	**30**	**3.3 ± 0.5**
5.0 ± 0.6	N_2	no UV, no heat	-8	11	5.0 ± 0.7
	N_2	heat only	-8	28	5.0 ± 0.9
	N_2	UV	-46	39	5.4 ± 1.2
	Air	no UV, no heat	95	37	4.3 ± 0.7
	Air	heat only	128	41	4.2 ± 0.7
	Air	UV	135	74	4.1 ± 1.0
	Air	***ALD, UV***	**-14**	**4**	**5.1 ± 0.6**
7.0 ± 0.7	N_2	no UV, no heat	-7	10	7.1 ± 0.8
	N_2	heat only	-6	15	7.1 ± 0.9
	N_2	UV	-16	32	7.3 ± 1.2
	Air	no UV, no heat	54	24	6.3 ± 0.8
	Air	heat only	77	27	5.9 ± 0.8
	Air	UV	> 156[b]	> 105[b]	< 5.2 ± > 1.6
	Air	***ALD, UV***	**-6**	**3**	**7.1 ± 0.7**

All data after one month of soaking. "UV" = 1.4 mW cm^{-2} of 365 nm light (this warms the films to ~50°C). "Heat" = 50°C. "ALD" = 18 nm of alumina deposited at 27°C.

[a] Spectral changes not monotonic. [b] Peak indistinct after four days.

[c] Effective size changes from PbS QD TEM sizing curve (Appendix A, Fig. S4).[55] These estimates attribute all optical shifts to size changes, ignoring changes in dielectric constant, coupling energy, and other factors, as well as the bandgap of any oxide surface layer. See text for details.

It is clear that ALD infilling is least effective at preventing redshifting and broadening of the smallest QDs. Figure 2.8 shows this explicitly by comparing the photothermal aging behavior of bare and ALD-infilled films of the three QD sizes. Whereas infilled 7 nm and 5 nm QD films show minimal changes in peak energy and peak width, the 3 nm QD films redshift and broaden considerably. This is caused by incomplete infilling of the exceedingly narrow interstitial spaces in the 3 nm QD films. We can estimate the size of these interstitial voids by modeling the films as a close-packed array of spheres with a center-to-center distance of 3.5 nm (2.9 nm + 0.6 nm to accommodate the EDT ligands). The largest interstitial sites in such a film are approximately 1.5 nm in diameter, not much larger than the trimethylaluminum molecules used in the ALD process (approximate TMA dimensions: 7.4 Å × 7.4 Å × 4.2 Å). The molecular geometry of the molecule was optimized with Turbomole at TPSS/def2-TZVP quality. The size is determined by adding vdW radii to the internuclear distances. Although our QD films are not close-packed and the largest interstitial spaces are certainly bigger than estimated here, it is reasonable to expect the diffusion of ALD precursors to be inhibited by the particularly tortuous pathways within films of the smallest QDs.

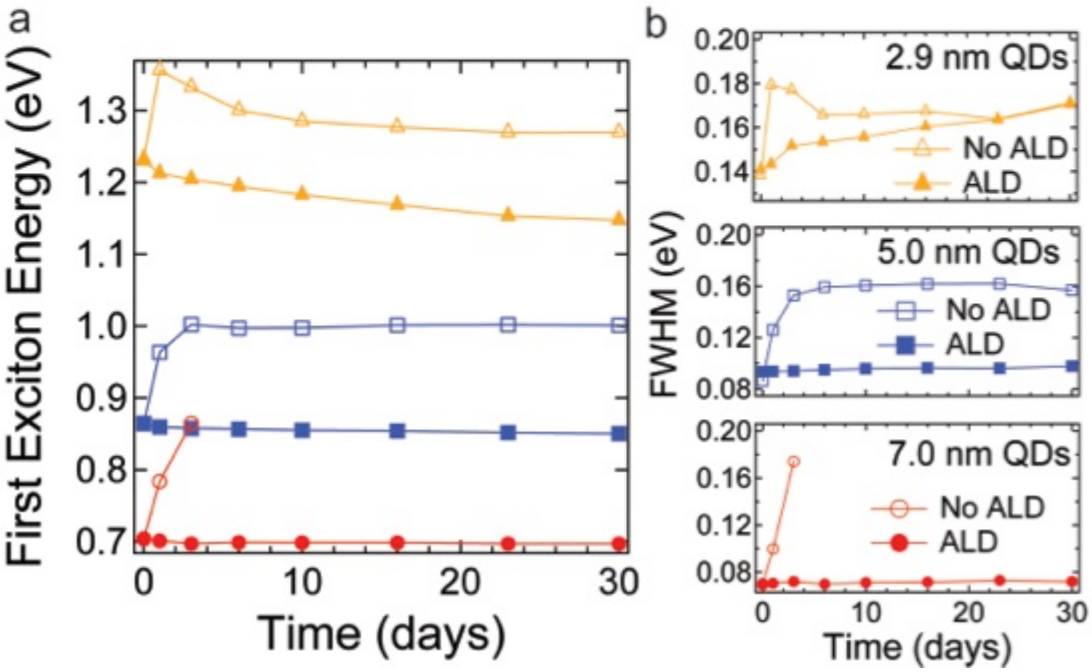

Figure 2.8. Comparative photothermal aging in air for the three QD sizes. (a) First exciton energy versus time in air. Open symbols are bare films and closed symbols are ALD-infilled films (18 nm alumina @ 27°C). All samples were exposed to 365 nm UV light at 50°C in air. The exciton peak of unprotected films of the largest QDs (open circles) was completely washed out after four days of photothermal soaking. (b) Peak width versus time in air. The legends in (b) apply to (a).

Figure 2.8 also shows that the aging behavior of the bare films in air depends strongly on QD size. The large QDs show the largest blueshift and broadening, resulting in complete washout of the excitonic peak, while the medium-sized QDs exhibit a moderate blueshift and broadening and the small QDs first blueshift and then redshift. To separate the effects of UV exposure and heat exposure, Figure 2.9 compares the photothermal and thermal aging behavior at nominally the same average temperature (50°C) for all three QD sizes. We observed that, relative to heat alone, UV illumination caused an increased blueshift for the large QDs, little change for the medium QDs, and a reversal of the initial blueshift for the small QDs.

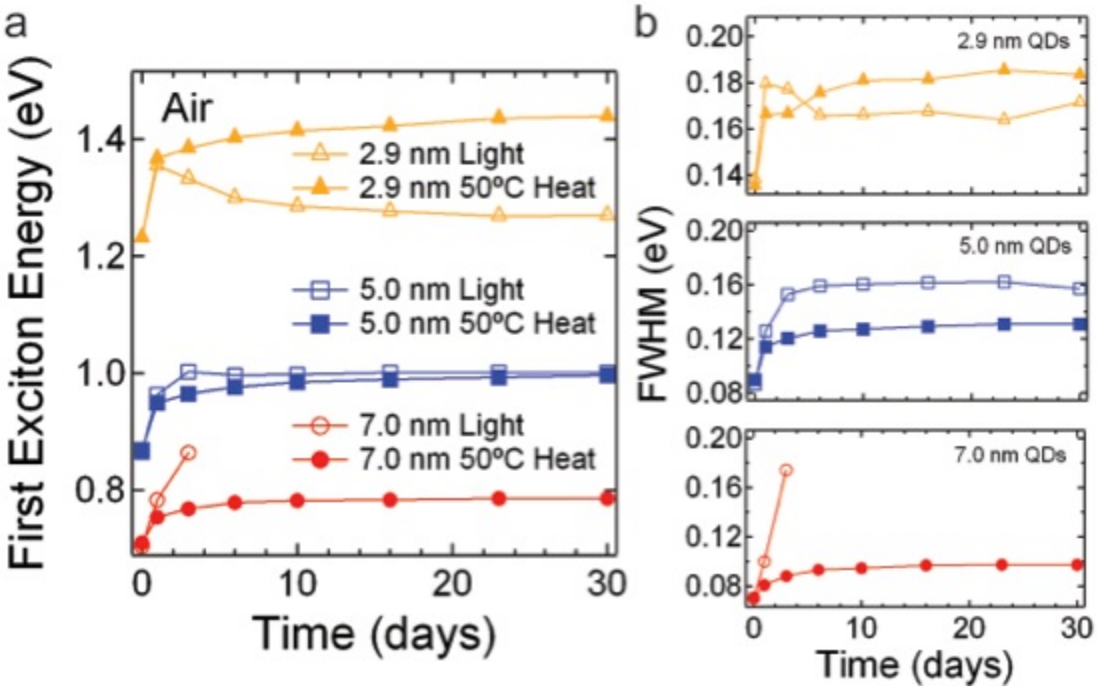

Figure 2.9. Comparison of thermal and photothermal aging behavior for the three QD sizes (no ALD). (a) First exciton energy versus time in air. Open symbols are films exposed to UV light and heat; closed symbols are films exposed to heat alone. (b) Peak width versus time in air. The legends in (a) apply to (b).

To explain these results, it is useful to reemphasize that shifts in peak energy reflect the net, ensemble-averaged outcome of processes that cause blueshifts and redshifts in the QD films. In air, blueshifts result mainly from oxidation (leading to decreased QD core diameters, lower dielectric constants, and less electronic coupling), while redshifts arise from ripening and sintering (resulting in increased QD diameters, higher local dielectric constants, and greater coupling). QD films in air undergo ripening/sintering and oxidation simultaneously, so the overall peak shift depends on the competition between these two relatively complicated processes.

UV illumination can promote thermally-activated processes such as oxidation and ripening/sintering by at least three distinct mechanisms: (*i*) generating electrons and holes capable of participating in chemical reactions at the surface of the QDs, (*ii*) creating localized, transient temperature spikes ("hotspots") from the cooling and recombination of hot carriers, and (*iii*) raising the average steady-state film temperature above 50°C via photon absorption. The first effect should promote surface redox reactions such as oxidation, while the latter two should increase the rate of both oxidation and ripening/sintering within the films.

To test the third mechanism (higher steady-state film temperature), we soaked films at elevated temperatures (65°C and 80°C) in the absence of UV light (Figure 2.10). These higher-temperature thermal soaks resulted only in larger blueshifts (greater oxidation) for bare QD films. Because increasing the soak temperature does not reproduce the qualitative or quantitative effects of UV illumination seen in Figure 2.9, we conclude that UV exposure must be doing more than just uniformly heating the films. The likelihood that the UV flux increases film temperature substantially above 80°C seems low. Therefore, we rule out steady-state film heating as an important effect of UV illumination.

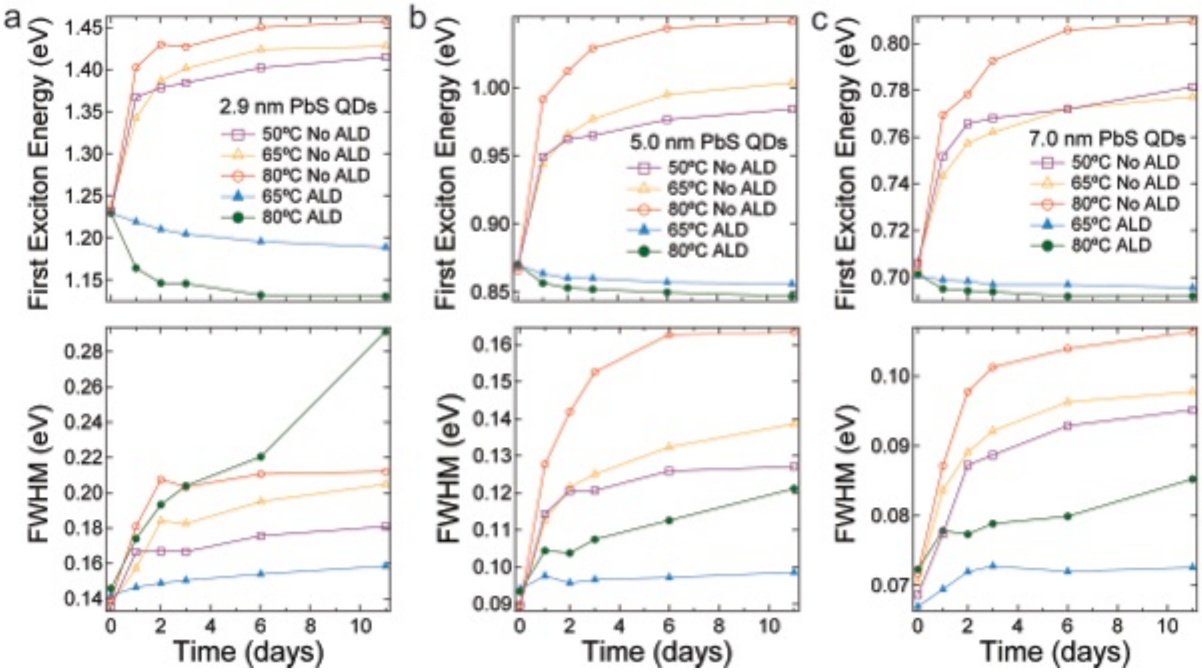

Figure 2.10. Thermal aging behavior in air at different temperatures. Time traces for (a) 3 nm, (b) 5 nm, and (c) 7 nm QD films. Both uncoated and ALD-infilled films are shown.

The data in Figure 2.9 are best explained if UV illumination triggers photo-oxidation (mechanism 1) and hotspot-induced ripening/sintering (mechanism 2) in a ratio that varies systematically with QD size. Our results show that long-term UV exposure causes net oxidation of large QDs but net sintering of small QDs. This size dependence probably results from the larger thermodynamic driving force for the ripening/sintering of smaller, higher surface area spheres. If ripening/sintering is favored for smaller QDs but oxidation is independent of size (such that smaller QDs undergo more ripening/sintering as they oxidize), then net peak shifts should be redder for smaller QDs, as observed (Fig. 4). In other words, we believe that photo-oxidation occurs about equally for all QD sizes but UV-generated temperature spikes preferentially cause surface diffusion and ripening/sintering of small QDs because of the larger driving force for surface area reduction in small QD films. Thus, UV exposure of 3 nm QDs yields an initial blueshift (oxidation) followed by a marked redshift (ripening/sintering). UV exposure of 5 nm QDs enhances oxidation and ripening/sintering about equally, so these effects cancel and there is little net change compared to thermal soaking alone. Finally, UV exposure of 7 nm QDs enhances oxidation more than ripening/sintering, causing the excitonic peak to blueshift strongly with soaking time.

In contrast to recent reports of remarkable air stability of small PbS QDs in solar cells,[24,29] we observed considerable shifts in peak energy and width of small (3 nm) QD films for all aging conditions explored in this study (no light or heat, heat only, and UV soaking). Moreover, ALD infilling stops the oxidation but not the ripening/sintering of these films during UV soaking in air. Since the ALD overcoat acts as a gas diffusion barrier in a manner similar to the top metal electrode of a solar cell, it is remarkable that Luther *et al*. observed none of the peak shifts seen here even after 1000 hours of light soaking in air.[29] However, their stability tests were performed at 20°C using a low-flux sulfur plasma lamp that emits very little UV light, while our ALD-infilled films were tested at 50°C in strong UV light. Moving forward, it will be interesting to test the stability of PbS QD solar cells at higher temperatures and under standard AM1.5G illumination.

Ex Situ TEM Imaging. We used TEM to directly image QD monolayers before and after photothermal soaking. Although monolayers cannot be expected to age in precisely the same fashion as multilayer QD films, they should provide a qualitatively accurate picture of the morphological changes induced by the various treatments. Samples were prepared on SiO_2 window TEM grids by drying a drop of QD solution followed by ligand exchange with EDT. We studied only the largest of the three QD sizes (7 nm) because of the difficulty in obtaining useful time series images of the smaller QDs. Figure 2.11 compares representative images of QD monolayers before and after a month of UV soaking in nitrogen or air without ALD versus in air with ALD. The QDs aged in nitrogen lose their faceting (becoming more “diffuse” in shape and size), but do not show obvious ripening or sintering, which is consistent with the small redshift and minor broadening observed in absorption spectra of the corresponding multilayer films (Appendix A, Fig.

S5). In contrast, the QDs aged in air show marked changes in size and shape and some changes in connectivity (Figs. 2.11 and Appendix A, Fig. S9). The average QD diameter appears to shrink by ~0.7 nm, the shapes become more irregular, and the size distribution considerably broadens after photothermal treatment, but the positions of the QDs are nearly unchanged (to within 1-2 nm). It is clear from these images that the QDs both oxidize and ripen in air and, furthermore, that ripening occurs mostly by atomic diffusion between immobile QDs rather than by QD diffusion and aggregation. These morphological changes are qualitatively consistent with the large blueshift and broadening observed in film spectra (Appendix A, Fig. S5).

We also imaged QD monolayers immediately before and after the deposition of 11 nm of ALD alumina and again after one month of photothermal soaking in air. The presence of the ALD coating leads to a considerable loss of image sharpness (Fig. 2.11). Despite the blurriness of the post-ALD images, we can confidently state that the QDs retain their positions and sizes after photothermal soaking, as anticipated from the nearly unchanged absorption spectra of the multilayer films. The ALD coating effectively stops both oxidation and ripening of the QDs (at least at this temperature).

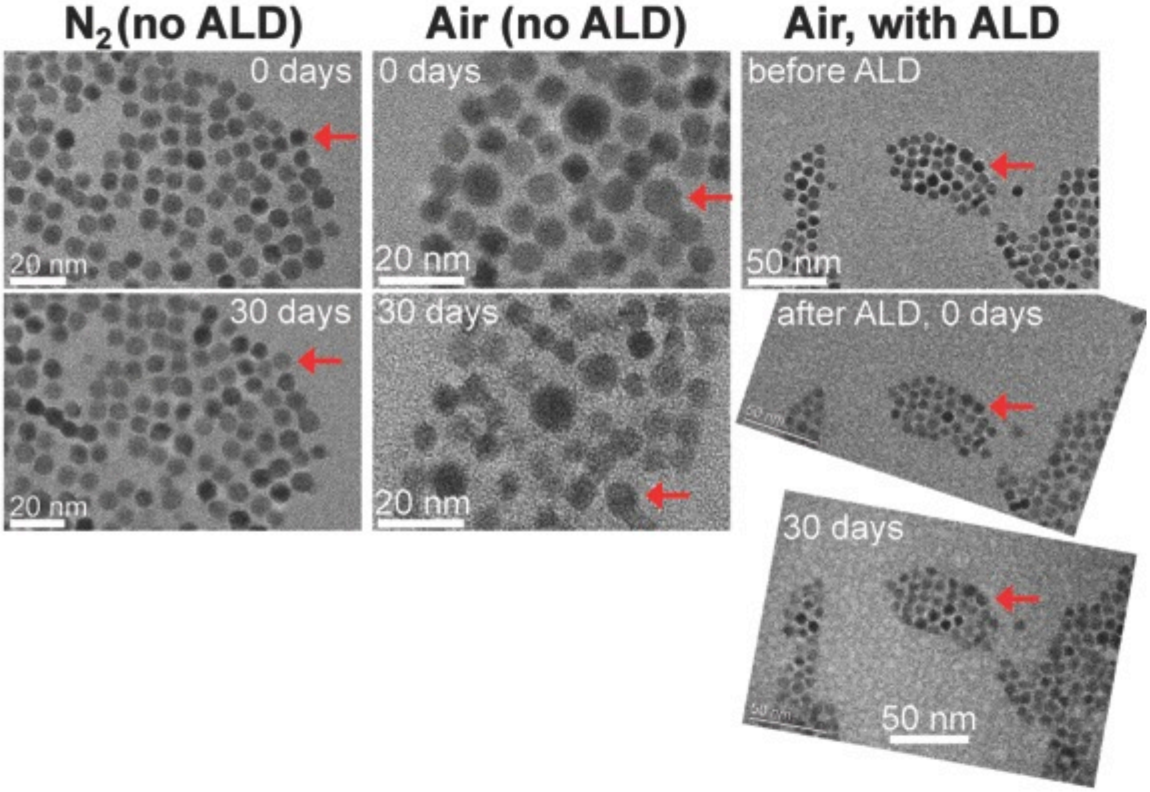

Figure 2.11. ***Ex situ*** **TEM imaging of UV-soaked QD monolayers.** Sample conditions are as follows: (*left*) nitrogen without ALD; (*middle*) air without ALD; (*right*) air with ALD. The red arrows are reference markers for each pair of images. Electron beam damage was negligible in these experiments. However, we observed substantial beam damage of ALD-infilled monolayers at higher magnification. Controls for samples aged in the dark in nitrogen at 193 K and 298 K and in air at 298 K can be found in the supporting information (Appendix A, Fig. S10).

High-Temperature Aging. Commercial photovoltaic modules must pass demanding environmental stability tests, including 1000-hour soaks at 85°C and 85% relative humidity (so-called 85/85 damp heat tests). As a prelude to true device testing, we soaked 5 nm QD films at 65°C, 80°C, and 90°C in air in the dark to determine how they react to elevated temperatures. Figure 2.12a presents stacked spectra of bare and ALD-infilled films soaked at 80°C for 11 days, while Fig. 2.12b compiles the time trends in peak energy and width for all samples studied. It is evident from these data that higher temperatures generally cause larger peak shifts and greater broadening, as expected. The small, temperature-dependent redshift and broadening observed with ALD-infilled films indicates that the ALD coating remains an effective oxidation barrier but allows progressively greater ripening and sintering of the QDs at higher temperatures. It is not yet clear how this internal diffusion will affect the electrical properties of the films (conductivity, carrier type and mobility, etc.). ALD-infilled films tested at 100°C showed rapid redshifting and complete loss of the exciton peak within one day, which we interpret as complete structural failure of the ALD matrix caused by chemical reactions between it and the QDs. Better thermal stability may be achievable by using denser ALD alumina coatings deposited at higher temperatures (50-75°C) or by switching to another ALD material (MgO or SiO_2, for example). The thermal stability of QD field-effect transistors and solar cells built from ALD-infilled films is under evaluation in our laboratory.

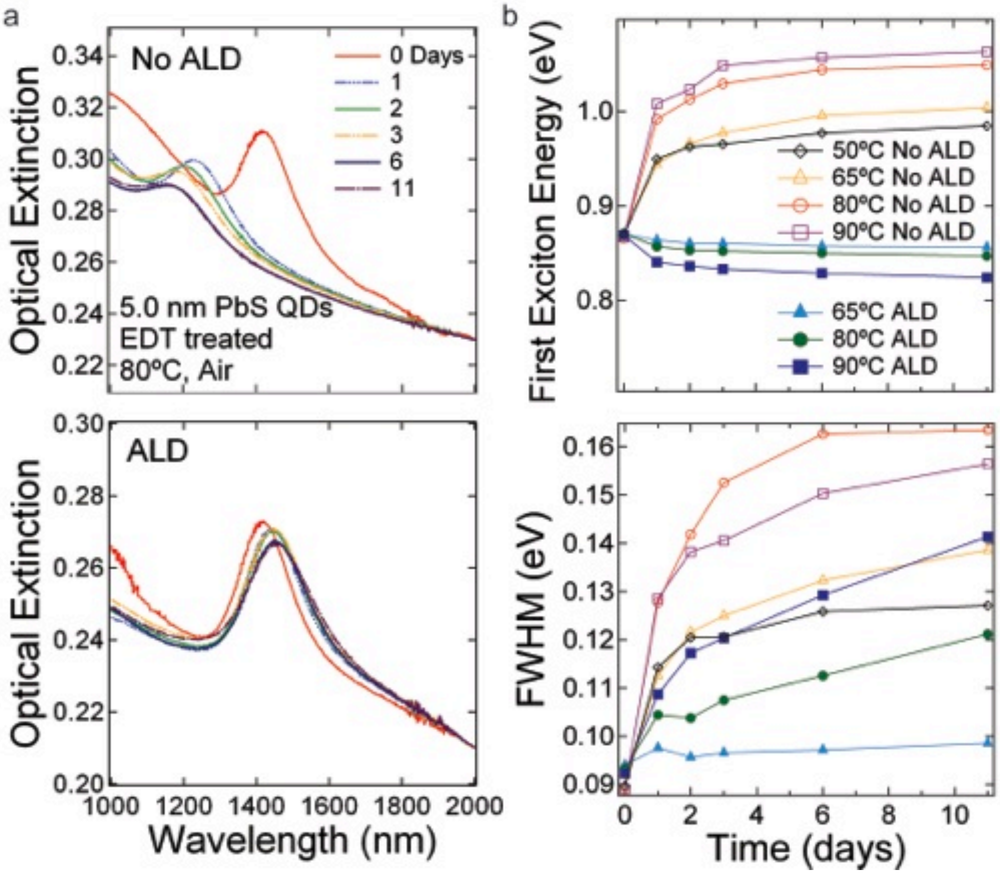

Figure 2.12. Thermal soaking of films of 5 nm PbS QDs in air. (a) Raw data for EDT-treated QD films soaked at 80°C in the dark, without and with ALD treatment. (b) Peak energy and width versus time for films soaked at 50°C, 65°C, 80°C, or 90°C for 11 days.

Low-Temperature Aging. We also studied the effect of low temperatures on the aging behavior of our QD films in order to better understand the nature of the aging process in different gases. Films soaked in inert gas (nitrogen or helium) at low temperature show no changes in absorption spectra, presumably because the diffusive motion required for ripening and sintering is frozen out. For example, films of 3 nm QDs stored in the dark in nitrogen at 193 K (-80°C freezer) showed no changes in absorption spectra after one month (Table 2.1). Likewise, UV-induced redshifting and broadening was completely absent after UV soaking in flowing helium at 80 K (56 hour soak @ 3.5 mW cm^{-2}), whereas identical films soaked at 323 K showed typical redshifts (23 meV; Appendix A, Figure S11). The complete freeze out of optical changes at these relatively mild temperatures suggests that QD ripening and sintering are strongly activated processes (i.e., large activation energies).

We also soaked films in dry oxygen to test whether QD oxidation could be suppressed at low temperature. Figure 2.13 shows a plot of peak energy and peak width for films of 7 nm QDs soaked for 50 hours in UV light (3.5 mW cm^{-2}) and flowing oxygen at various temperatures (110-321 K). There are three salient features of the data. First, we cannot completely stop oxidation even at the lowest temperature (films soaked at 110 K still blueshift by ~25 meV). Second, the temperature dependence does not follow simple Arrhenius behavior. Instead, we observe a temperature-independent ~25 meV blueshift of the peak position at "low" temperatures (110-250 K) and a rapidly-increasing blueshift at temperatures above 250 K. Time series show that the low-temperature blueshift occurs gradually during the UV soak. This behavior suggests the existence of two distinct stages of oxidation, with one stage dominant at low temperature and the second activated only at high temperature. We speculate that, at low temperature, oxidation is limited to the outermost monolayer of QD surface atoms. Once these atoms are oxidized (probably by chemisorption of oxygen), oxidation self-terminates and the blueshifting stops. At higher temperatures, however, there is sufficient thermal energy to activate solid-state diffusion and enable the oxidation of atoms deeper inside the QDs, resulting in a strong enhancement of the blueshift with temperature.

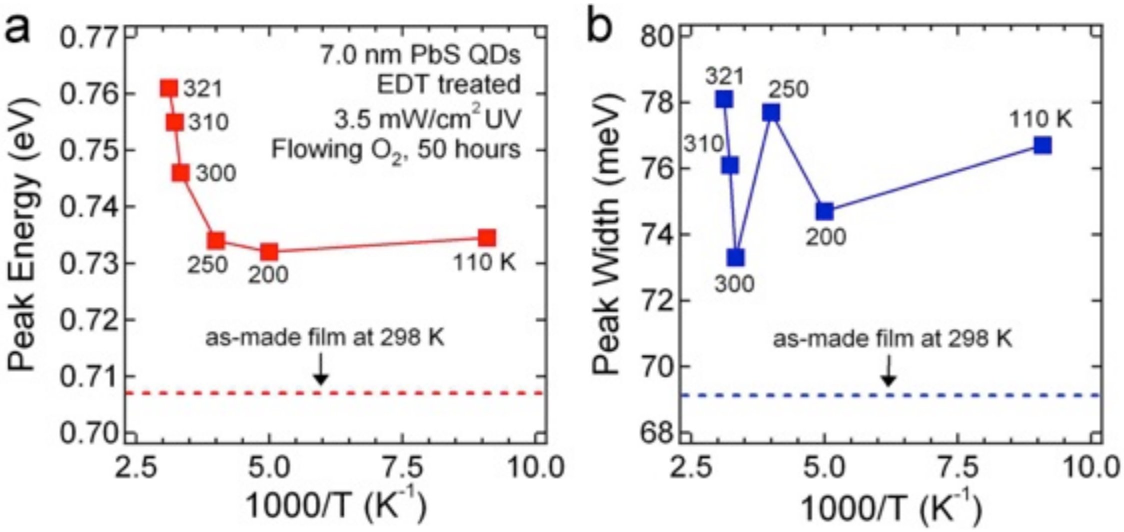

Figure 2.13. First exciton peak energy and width for films soaked in UV and oxygen for 50 hours at various temperatures. (a) Peak energy. (b) Peak width. The values for a film before UV soaking are indicated by the dotted lines.

The third remarkable feature of the data in Figure 2.13 is the anomalously small and temperature-independent peak broadening, which averages only 7 meV across the temperature range (Fig. 2.13b). In comparison, films that were UV soaked at 323 K in air exhibited ~70 meV of broadening over the same period. We attribute the difference in peak broadening to the presence of moisture in air. This conclusion is based on the comparison of films UV soaked at room temperature in dry oxygen versus humidified oxygen in a purpose-built environmental chamber. We observed five times more peak broadening in wet oxygen than in dry oxygen (22 meV versus 4 meV after 10 hours of soaking), yet the blueshifts were very similar in the two environments (Appendix A, Figure S12). Enhanced peak broadening in the presence of moisture implies that water increases the QD size distribution without affecting the average QD size relative to UV soaking in dry oxygen. The explanation for this behavior is not clear, but it is possible that adsorbed water speeds oxidation of select QD surface facets, resulting in greater size polydispersity for wet oxidized QD films.

To summarize, our low-temperature studies show that (*i*) UV-induced ripening and sintering of PbS QD films can be frozen out at low temperature but oxidation is only partially suppressed even at 110 K, (*ii*) oxidation follows a non-Arrhenius temperature dependence, with weakly-activated, self-terminating surface oxidation at low temperature and strongly-activated subsurface ("bulk") oxidation at high temperature, and (*iii*) moisture somehow increases the QD size distribution in photo-oxidized films without affecting the average QD diameter.

In conclusion, we have described the aging behavior of PbS QD films as a function of ambient atmosphere, temperature, UV illumination, and QD size. Aging in air causes oxidation and blueshifts of the first exciton peak in optical spectra, while aging in nitrogen results in ripening/sintering and redshifts in optical spectra. Both oxidation and ripening/sintering coarsen the QD size distribution and broaden the first exciton peak. Infilling and overcoating QD films with ALD alumina at room-temperature produces inorganic nanocomposites in which internal and external diffusion are inhibited. The ALD coating serves both as a gas diffusion barrier that prevents oxidation and a 3D inorganic matrix that inhibits internal atomic and molecular motion. A 18 nm alumina overcoat completely prevents oxidation regardless of QD size, whereas the alumina matrix is most effective at stopping ripening/sintering of the larger QDs, which are easier to infill. TEM imaging of 7 nm QD monolayers revealed morphological changes consistent with the shifts observed in optical spectra. The ALD layers remain effective up to temperatures of ~100°C, at which point they fail, apparently by reacting with the QDs.

We find that UV illumination causes preferential oxidation of large QDs but preferential ripening/sintering of small QDs. This difference is due to the greater driving force for ripening/sintering of smaller QDs. The main mechanism of UV action is not simple film heating;

instead, UV-generated electron-hole pairs (*i*) cause photo-oxidation and (*ii*) create hotspots that trigger diffusion and ripening/sintering (particularly in small QDs). We can completely freeze out UV-induced ripening/sintering in inert gas by cooling films to 80 K, which suggests that ripening/sintering are strongly-activated processes. However, UV-induced oxidation could not be eliminated even at temperatures as low as 110 K. From the temperature dependence we identify two stages of oxidation, with self-terminating oxidation of the outermost monolayer of surface atoms occurring at low temperature and strongly-activated subsurface oxidation important at higher temperature. We also find that moisture is somehow responsible for most of the increase in size distribution of PbS QD films aged in air. Our results will be useful in ongoing efforts to fabricate truly stable QD films for next-generation solar cells.

CHAPTER 3

Atomic force microscopy

Atomic force microscopy (AFM) is a surface analytical technique that can characterize physical and chemical properties of a substrate surface or thin-film.[71-73] In its basic form, examples of measurable properties include relative surface heights, surface roughness, sample hardness and stiffness.[74,75] However, recently developed advanced AFM techniques can also measure surface electrical characteristics such as charge,[76] polarization[77] and potential.[78]

In AFM, a probe tip is brought into close proximity of a surface and the tip is rastered across the surface using specific tip-sample interactions as a mechanism for feedback. The probe tip is attached to a force-sensing, flexible cantilever and typically has a radius of curvature ranging from 20-30 nm such that very small nanoscale features can be resolved. A feedback laser is focused on the back of the cantilever directly above the probe, which is then reflected onto a position sensitive photodiode (see Figure 3.1). As the probe tip interacts with the sample surface, the deflection of the cantilever causes the position of the reflected laser spot on the photodiode to move, thus providing a means to monitor the nanoscale interaction between the probe tip and sample surface.

AFM provides a three dimensional map of surface structure and topology. Relative to other microscopy techniques such as scanning electron microscopy (SEM), AFM can be utilized under ambient conditions without the use of a vacuum and will not result in destruction of the sample. Different types of imaging modes in AFM have been developed, including contact and tapping modes which are used quite frequently. In contact mode AFM, the probe tip is in direct contact with the sample surface, and the deflection is used to generate the 3D surface map as the probe traces the contours of the surface. In tapping mode (AC mode) the cantilever is driven near its resonance frequency by a piezoelectric component in contact with the cantilever chip. The cantilever is driven at a specified AC oscillation amplitude given in units of volts, which equates to a physical range of motion (in nanometers). As the probe tip interacts with the sample surface, the amplitude of oscillation is changed by damping forces. The 3D map is generated by maintaining a constant amplitude of oscillation by adjusting the height of the probe tip in the z-direction. For most samples, this method of imaging is preferred because it creates less damage to the probe tip and the sample surface relative to contact mode.[79]

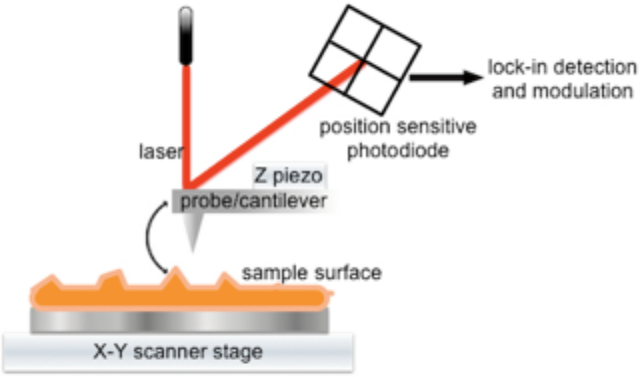

Figure 3.1 Schematic of an atomic force microscope interacting with a sample surface. The probe is attached to the cantilever, which is mechanically driven at a specified target amplitude of oscillation. As the probe interacts with nanoscale features of the sample surface, the amplitude of oscillation changes. Using a laser focused onto the back of the cantilever above the probe tip and a position sensitive photodiode, the motion of the tip can be recorded. Maintaining a constant amplitude of oscillation can be achieved using lock-in detection and modulation, whereby the Z-piezo adjusts the height of the probe according to the topology of the surface.

Imaging QD thin-films with AFM

AFM has the capability to resolve nanoscale objects and features. Here, achieving nanometer resolution of individual quantum dots (QDs) as a test-bed is discussed. A sub-monolayer film of ~6.3 nm PbSe QDs with an oleate-capping was deposited onto a silicon substrate (RMS roughness <1 nm) and imaged with tapping-mode AFM using an Asylum MFP-3D housed in a Herzan isolation chamber and Olympus AC160TS probes. Achieving the appropriate conditions for nanoscale resolution depends on the radius of the probe, sample surface roughness (RMS roughness), sample topology, mechanical and thermal drift, piezo drift (cantilever Z-piezo, or X-Y scanner piezos), and scanning parameters including target amplitude, setpoint and controller gain.[80] With the objective of imaging individual QDs, it is important that the substrate roughness not exceed the diameter of the QDs to avoid the substrate morphology dominating the topology. Indeed, the RMS roughness (<1 nm) of the silicon wafer[81] substrates is less than the diameter of the 6.3 nm QDs used in this study. Figure 3.2 illustrates the effects of drift and optimization of scanning parameters on the resulting AFM topography image of the QD film.

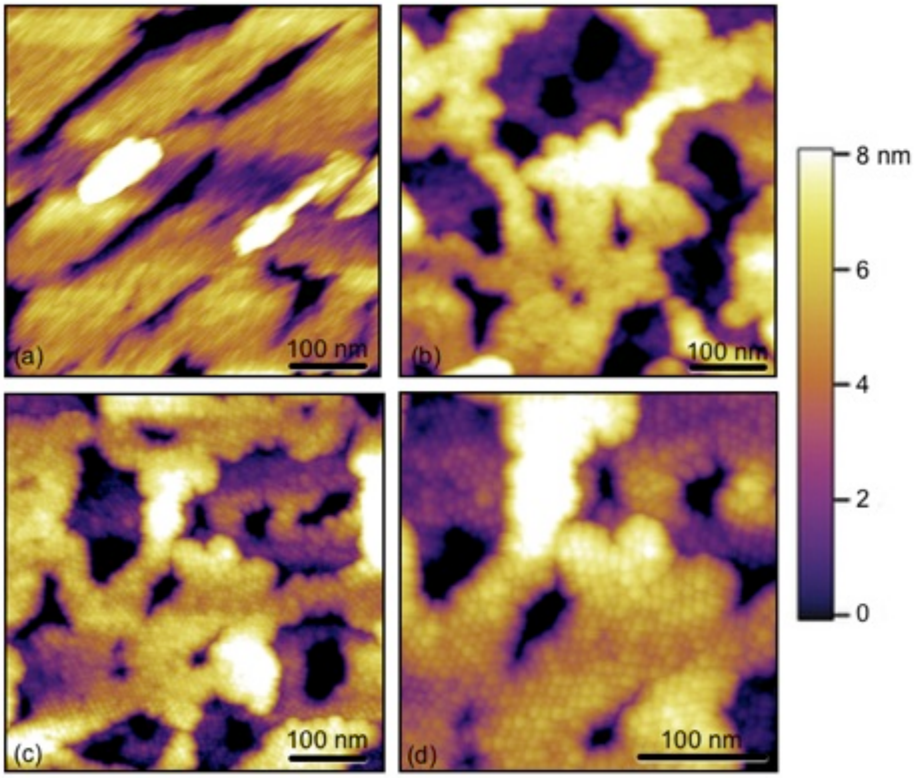

Figure 3.2 AFM imaging of individual 6.3 nm PbSe QDs. Achieving QD resolution can be impeded by **(a)** mechanical and thermal drift **(b)** non-optimized scanning parameters. **(c)** Ideal scanning conditions allowed for individual QD resolution to be achieved. **(d)** Zoom-in of (c).

In Figure 3.2a, the image was obtained by immediately scanning the topology after the substrate and cantilever were loaded into the AFM system. The image appears slanted in one direction due to mechanical drift of the AFM components including the sample mount and scanner stage. Allowing the sample to sit in the isolation chamber undisturbed overnight removed effects from mechanical and thermal drift; Figure 3.2b shows that the image is no longer slanted. Nevertheless, the scanning parameters chosen in Figure 3.2b are not ideal for individual QD resolution. The target amplitude in Figure 3.2b was adjusted to 1.00 V, corresponding to a 100-nm range of motion of the probe tip. This range of motion is too high for the probe to accurately image soft samples with low surface roughness. The physical convolution between the probe and nanoscale features of the sample needs to be small for enhanced resolution, especially for small objects such as QDs. This was achieved by adjusting the target amplitude to 0.5 V; accordingly, individual QD resolution was achieved and is shown in Figure 3.2c,d.

Understanding the film morphology of QD thin films on technologically-relevant surfaces was accomplished with AC mode imaging as a function of dip-coating cycles. This study has broad implications in understanding the conductivity of charges transported in electrical devices such as solar cells and transistors. Briefly, PbSe QDs having average diameters ~6.3 ± 0.3 nm were used motivated by the enhanced carrier mobility displayed for this particular QD size[82] along with an 1,2 ethanedithiol (EDT) treatment.[25,39] Pre-cleaned substrates were dipped into a solution of 2 mg mL^{-1} of QDs in hexane and a 1 mM solution of EDT in acetonitrile in a nitrogen filled glove-box. Three different substrates were chosen including silicon, silicon oxide and a 140 nm-thick indium-tin oxide (ITO) thin film on glass. Electrical properties of QD thin films are often ascertained using a thin-film transistor[23] whereby the QD film is in direct contact with Si and SiO_2 surfaces, thereby motivating our choice. Furthermore, ITO is nearly a ubiquitous transparent conducting oxide layer in solar cells constructed with QDs.[29,83,84] The film morphology was evaluated with AFM at varying degrees of dip cycles including 1, 2, 3, 4, 5 and 10 cycles (1 dip cycle = 1 dip in QDs + 1 dip in EDT treatment + 1 dip in an acetonitrile rinse); films were mechanically dip-coated using a Nima Multi-vessel System. AFM images were acquired using an Asylum Research MFP-3D SA system operating in tapping mode and Olympus AC160TS tapping-mode probes. Scanning electron microscopy images were acquired using a Zeiss Ultra 55 system.

As-synthesized PbSe QDs have long-chain oleate ligands on their surfaces which impede charge transport and conductivity in a QD thin-film.[39] Exchanging the oleate ligands for short-chain organic or inorganic molecules has shown to improve the film conductivity. This process affects the resulting film morphology due to contraction of the inter-QD distance.[85] Figure 3.3 displays AFM images of a QD film on a silicon substrate with and without an EDT treatment. Comparing the film morphology before and after the EDT treatment reveals that the QD layer contracts in volume as would be expected with the exchange of the native long chain ligand for a shorter chains. This is observation is consistent with a prior report on PbSe QDs treated with hydrazine.[45]

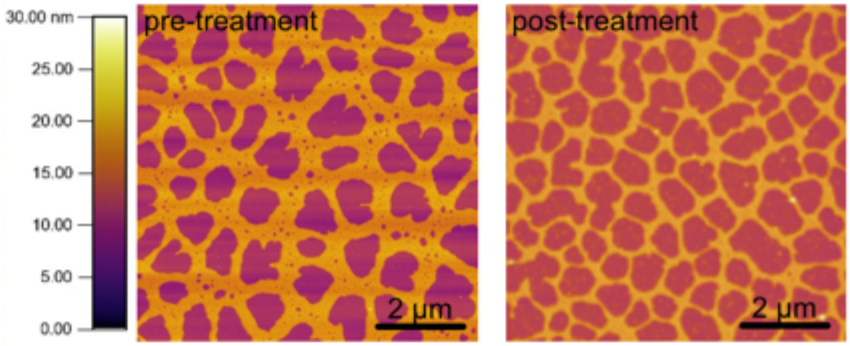

Figure 3.3 Film morphology of one PbSe QD sub-monolayer, pre- and post-treatment with EDT on a silicon substrate. Based on the false color-scale of the image, the orange colored region represents regions of the QD film, while the dark purple and red areas (pre- and post-treatment, respectively) are the underlying silicon substrate. The film contracts upon treating the QDs with EDT.

The film morphologies with increasing number of dip cycles for EDT treated PbSe QDs are displayed in Figure 3.4. Observing the AFM images at 3 dip cycles shows less exposed substrate area relative to the morphology at 1 dip cycle. The morphology can be loosely equated as web-like and subsequent monolayers deposited tend to prefer the underlying QD layer rather than the substrate. Some of the physical interactions that can dictate resulting film morphology include QD-QD and substrate-QD interactions (Coulomb, van der Waal and capillary forces, etc.), and substrate surface roughness.[86] Since QDs attach primarily to the underlying QD layer, this could indicate the QDs interact with each other through fixed dipoles. It is known that surface dipoles[87] from the faceting on each QDs can result in charged QDs. The dipoles on the QDs may aid in bi-layer formation and Volmer-Weber-like growth,[88] whereby deposition of the second monolayer preferentially interacts with other QDs rather than the substrate. The web-like, discontinuous film morphology may augment the complexity of the charge transport process *via* a perturbation in hopping conduction mechanism.[82]

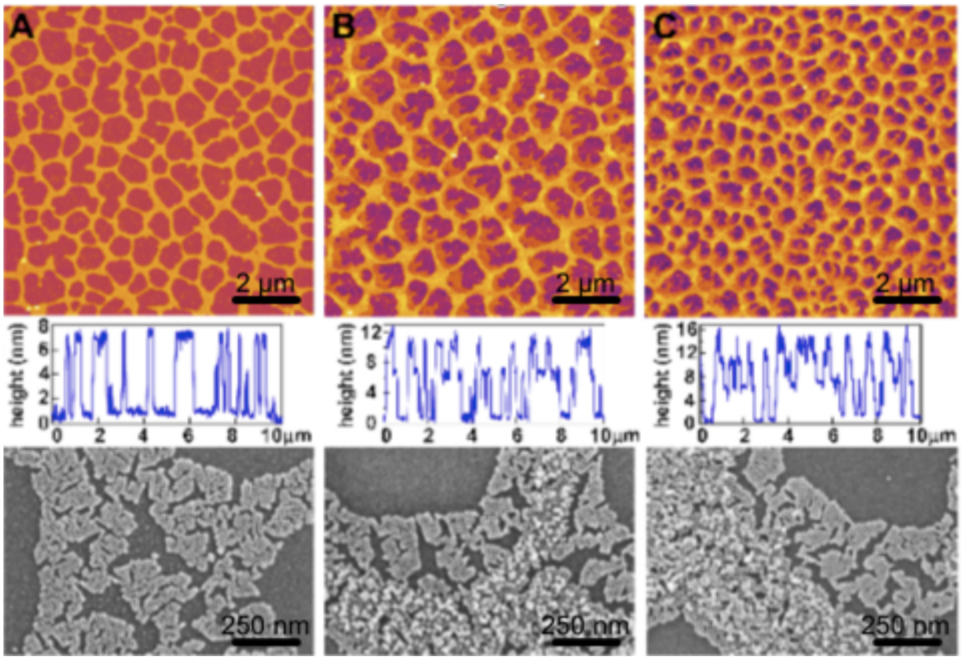

Figure 3.4 AFM/SEM images of EDT treated QD films on silicon with **(a)** 1 **(b)** 2 and **(c)** 3 dip cycle(s). Line-scans across each image were taken for each area scanned with AFM to display

height profiles (shown below AFM image). Formation of 1-2 sub-monolayers is achieved in this low dip cycle regime.

Analyzing each AFM image in Figure 3.4 with Gwyddion, a free-source AFM analytical software program, at each stage of dip-coating was performed and is shown in Table 3.1. The % coverage metric analyzes the percentage of bare spots with exposed substrate in the 10 x 10 μm^2 image. Between 1 and 4 dip cycles, very little multi-layers are created thus the film thickness does not reach theoretical thickness of ~24-28 nm, corresponding to 4 multi-layers of 6 nm QDs. At 5 dip-cycles, the QD film retains almost 100% coverage and results in a film thickness of around 15 nm. From 5 to 10 dip cycles, the film thickness roughly doubles. In this regime, the buildup of the film becomes linear with increasing number of dip-cycles.

Table 3.1 An analysis of film morphology for 6.3 nm PbSe QD films on silicon substrates with increasing dip cycles.

dip cycles	% coverage[a]	film thickness (nm)[b]	number of layers[c]
1	30	7	1
2	60	13	2
3	75	14	2
4	93	13	2
5	97	15	2-3
10	99	27-30	5

[a] The % coverage metric was determined by analyzing AFM images with Gwyiddion.

[b] Film thickness was determined by taking height profiles from each AFM image.

[c] The number of monolayers corresponds to the film thickness divided by the average size of the QD, ~6.3 plus the size of the oleate ligand ~1 nm.

Figure 3.5 shows the film morphology of same-sized PbSe QDs on SiO_2 and ITO with an EDT treatment. Observing the film morphology on SiO_2 substrates (Fig. 3.5a) reveals a similar web-like film morphology indicating both Si and SiO_2 substrates act to promote Volmer-Weber-like film growth. Obtaining images of the film morphology on ITO proved difficult because the natural surface roughness of the ITO[89] is much greater than the silicon substrates making it hard to distinguish between the morphology of the QDs and ITO. For this reason, SEM was used to image the film morphology (Fig. 2.5b). The QDs on ITO tend to position themselves according to the natural topology of the ITO. Here, the surface roughness dominates the film morphology, superseding the tendency for QDs to deposit onto other QDs. The web-like morphology is no longer observed, illustrating that film morphology can depend entirely on the substrate choice. With increasing dip cycles however, thick films of QDs on ITO (100nm or greater) that are free of pin-holes can be achieved in this fashion.[39]

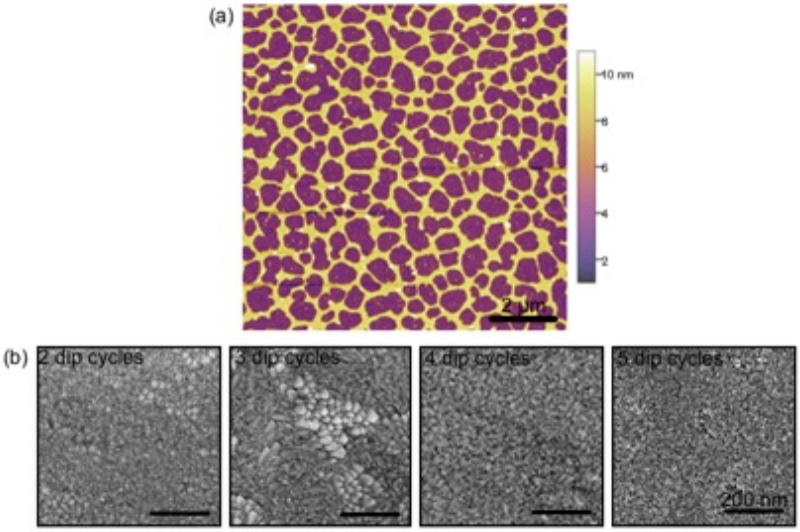

Figure 3.5. (a) Film morphology of an EDT treated QD film at 1 dip cycle on a SiO_2 substrate. The resulting film morphology is markedly similar to the morphology observed on silicon substrates. **(b)** Film morphology of EDT treated QD films on ITO substrates as a function of dip cycle. The film morphology no longer displays web-like growth. The white area in the 3 dip cycle image reflects the natural morphology of the ITO substrate. A continuous film of disordered QDs at 5 dip cycles is observed allowing for the fabrication of pin-hole free QD films for solar cells.

Electrical modes of AFM

The AFM probe can also be used to study electrical properties of a sample or opto-electronic device. When a conductive coating is added to the probe tip, typically Pt/Ir (because it demonstrates good adhesion), the probe can become a nano-sized multimeter to measure current,[90] potential[91] and capacitance (scanning capacitance microscopy)[92]. In conductive-AFM (c-AFM), the probe tip is in direct contact with sample forming a nanojunction which can be employed to map the conductivity of a sample and collect point-by-point current-voltage curves for resistance measurements.[93] Scanning Kelvin probe microscopy (SKPM) measures the electrical potential of a surface (surface potential). In SKPM, in addition to the conducting AFM tip being driven at its resonance frequency, an additional *AC* bias modulation (~18−350 kHz, depending on the technique) is added to modulate the electrostatic forces between the tip and the surface.[78] This enables lock-in detection of the electrostatic forces and the amplitude of the vibrating probe is monitored to generate a surface potential map of the surface. Subsequently, by taking the mathematical derivative of the surface potential profile, electric field distributions can be mapped (Figure 3.6).

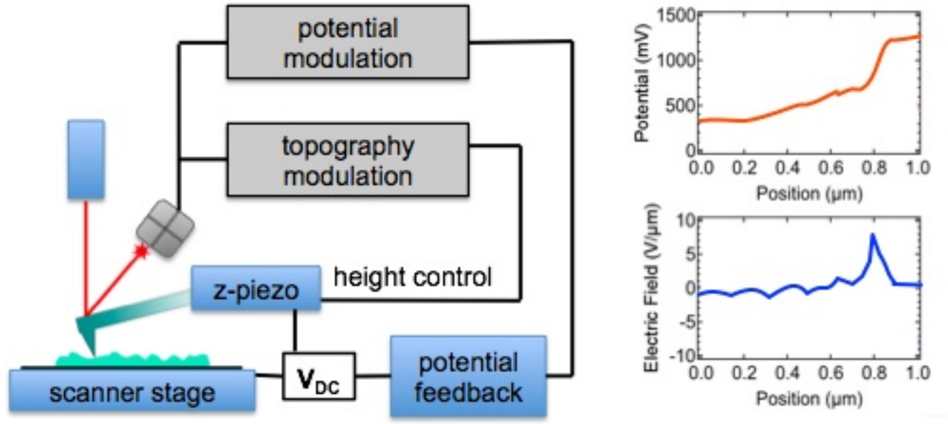

Figure 3.6. Schematic of an AFM equipped with SKPM modulation. Here, the probe is collecting two signals, topography and surface potential. These signals can be modulated using the same frequency or separate frequencies. The output of the measurement creates a map of surface potential. By taking a line-scan in the surface potential map a potential profile (potential *vs.* position) can be created. Taking the first mathematical derivative of the potential derivative can generate an electric field profile (V/μm).

As the probe comes close into contact with a sample surface, the amplitude and frequency of the probe will change due to electrostatic interactions between the probe and sample. The electrostatic interaction is based on the contact potential difference (CPD) between the probe and sample generating a flow of charges as the Fermi energy levels equilibrate between the probe and sample surface. The SKPM feedback mechanism works to nullify the CPD between the tip and the surface by applying a voltage to the tip directly equal to the CPD to cancel out the forces acting on the probe (see Figure 3.7).[94] Thus a 3D map of surface potential is generated. The probe can be used to measure relative work function differences of the sample under study. Absolute measurements of work function can be achieved if the work function of the tip is measured and calibrated.[94] Electrostatic forces arising from dynamic or fixed charge at the surface or an applied bias to the sample can also cause the motion of the probe to be altered.

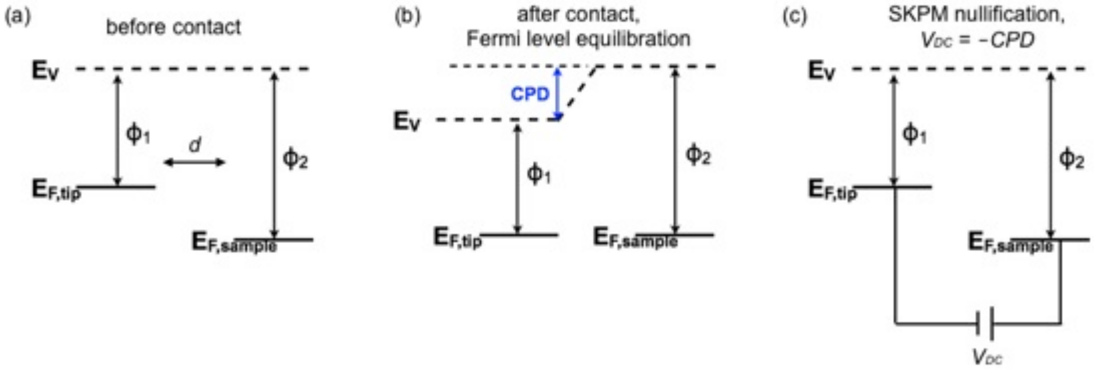

Figure 3.7. Relative work function measurement between tip and sample. (a) The tip and sample are separated by a distance, *d*, and have dissimilar work functions. **(b)** When the probe tip and sample come into contact, charges will flow to equilibrate the tip and sample Fermi energy levels creating a contact potential difference (*CPD*) in the vacuum level. **(c)** SKPM nullifies the contact potential difference by applying a DC voltage equal in magnitude to the contact potential difference between tip and sample.

The sample and probe tip can be modeled as a parallel plate capacitor according to Equation 3.1. Here, $\frac{\partial C}{\partial z}$ is the capacitive gradient, and $V_{app} = V_{DC} + V_{AC} \sin \omega t$, and V_{SP} is the surface potential.[95]

$$F_{\omega} = \frac{1}{2}\frac{\partial C}{\partial z}\left(V_{app} - V_{SP}\right)^2 \qquad \textit{Equation 3.1}$$

Minimization of the force at ω is achieved by applying a voltage equal in magnitude to V_{SP} ($V_{DC} = V_{SP}$).

The accuracy of the surface potential measurement can be complicated by many factors including the magnitude of the probe radius, sample roughness, detection method, the geometry and dimension of the probe/cantilever and sample.[95-99] In general, long-range electrostatic forces between the probe/cantilever and sample surface can average the surface potential between the probe tip and the immediate, underlying sample surface. To circumvent stray electric fields averaging surface potential, it is best to use probe tips with long probe lengths and narrow cantilever widths to minimize averaging effects.[96] Furthermore, it is best to detect the surface potential at a separate frequency from that of topography, to avoid convolution between the two signals. The single-pass method has shown great accuracy because it minimizes long-range electrostatic forces.[76,100]

At best, SKPM can measure surface potentials with an accuracy of <50 nm of lateral resolution and a ~10 mV energy resolution in ambient conditions.[76] For this reason, SKPM has been extensively used in studying bulk-semiconductor surfaces[94,101] to understand work-function variation,[101] semiconductor–semiconductor and –metal junctions,[76,102-106] and solar cell cross-sections.[103,107-114] SKPM provides nanoscale potentials to aid in understanding band-alignments, charge separation and transport, and hetero-interfaces. In the next section, the use of SKPM in understanding the nanoscale electrical potential in a transistor will be discussed.

Understanding the nanoscale electronic properties of devices with SKPM

PbX QD Thin-film Transistors. Opto-electronics comprise a vast array of devices that rely on phonon-electron interactions (through light or electricity) to form the basis of their function and purpose. Some of these basic principles include photoconductivity, the photoelectric effect and radiative recombination as shown in Figure 3.8.[115]

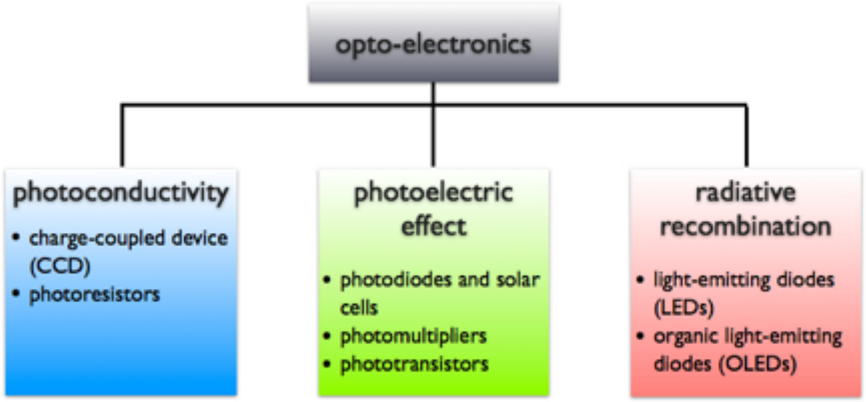

Figure 3.8 Some operational principles highlighted for the basis of opto-electronics. Device applications are listed in each colored box for each respective operational principle.

A brief background on thin-film transistors will be given here. Many different types of transistors have been developed and used for electronics and integrated circuits.[116] The thin-film transistor (TFT) will be discussed here since it provides the opportunity to study the electronic properties of thin-films of electronically coupled QDs. TFTs operate by controlling the microscopic flow of current between two electrode terminals and form the basis of electrical communication in logic circuits. A conductive channel that is formed can be controlled by the electrodes in the transistor such that the current flow is either in the on or off state thus forming the basis for logic circuits. From a fundamental perspective, TFTs offer the opportunity to study the charge transport properties occurring in PbX QD thin-films particularly charge carrier mobility of electrons or holes.[58] A TFT consists of three terminals, the source, drain and gate electrodes along with a dielectric oxide. By depositing a semiconducting thin film (*e.g.* QD solid) on top of the dielectric oxide, the gate dielectric can be utilized to accumulate electronic charges at the oxide-thin-film interface *via* an applied bias to the gate electrode. Generating a potential difference between and source and drain contacts will sweep the accumulated carriers in the channel thus generating a current. Depending on the channel potential, a TFT can behave as an *n*-type, *p*-type or ambipolar (conducting of both electrons and holes) transistor. Current-voltage (IV) curves are used to assess the rectifying behavior of the current in TFT.[116] Output and transfer IV curves are used to determine the type of TFT (*e.g.* *p*- or *n*-type or ambipolar), carrier mobility of the semiconducting thin-film (in units of cm^2 V^{-1} s^{-1}) and on/off ratio (I_{on}/I_{off}). The output curve is a plot of the drain current *vs.* source-drain voltage (I_{SD} *vs.* V_{SD}) as a function of gate bias (V_G). The transfer curve is a plot of drain current *vs.* the gate voltage (I_{SD} *vs.* V_G) as a function of gate bias (V_{SD}). The output curves at varying gate biases determines whether the TFT conducts current as an *n*- or *p*-type transistor, and if the TFT conducts both channels, then the TFT is designated as an ambipolar TFT. By analyzing the linear portion of the current in the transfer plots, the carrier mobility, μ_{lin}, can be calculated according to Equation 3.2 where $\frac{\partial I_{SD}}{\partial V_G}$ is the slope of the line in the transfer plot at a specified V_{SD}. The capacitance of the gate oxide, C_i, and the dimensions of the channel including the length, L, and width, W, are pre-determined constants depending on the actual configuration of the transistor.

$$\mu_{lin} = \frac{\partial I_{SD}}{\partial V_G}\frac{L}{WC_iV_{SD}} \qquad \textit{Equation 3.2}$$

The output and transfer characteristics can provide much information on the electronic quality of the semiconductor thin-film. Crystalline silicon has typical electron mobilities at room temperature >1000 cm^2 V^{-1} s^{-1}.[117] An analysis of PbX QD thin-films typically yield mobilities ~ 10^{-3} to 10^1 cm^2 V^{-1} s^{-1}depending on QD size[82] and surface treatment[41,52,58,59,118,119] and matrix material.[23,53] TFTs provide the opportunity to understand the electronic properties of PbX QD solids. However, analyzing the IV output and transfer curves is an indirect method to understand the channel potential. Employing SKPM to image the channel potential allows for a deeper understanding of the electronic properties of the QD solid in the TFT which will be discussed next.

SKPM of an empty-channel FET. Before evaluating the channel potential of a QD thin film, SKPM measurements were performed on a field-effect transistor (FET) without a conductive channel present. Briefly, a FET substrate was cleaned and mounted into a specially designed holder equipped with electrical contacts to apply a bias to the gate electrode and generate a potential difference between the source and drain electrodes. SKPM images were obtained with an Asylum MFP-3D in SKPM mode with varying tip-sample distances using Pt/Ir coated AFM probes (Asylum Research, Electrilevers). To better understand the influence of the cantilever on the measured surface potentials, the FET was scanned with the cantilever oriented orthogonal and parallel to the source and drain electrodes. The accuracy of the SKPM was evaluated by assessing the magnitude of the surface potential relative to the known potential to the source and drain electrodes applied from an external power source and compared for orthogonal and parallel orientations. It is expected that the orientation of the cantilever with respect to the sample will alter the capacitive coupling. Figure 3.9a shows the schematic of SKPM imaging the channel potential of an empty-channel FET with the cantilever in both the orthogonal and parallel orientations. The schematic illustrates scanning in the orthogonal direction; rotating the substrate 90° was performed to scan in the parallel direction. A voltage series was collected with the potential difference between source and drain electrodes equal to ±6.0, ±3.0, and 0 V with the gate electrode grounded and as a function of distance between the tip and sample (lift height, nm). Figure 3.9b displays the schematic of the conductive probe interrogating the topography and potential of the FET in the parallel orientation. Figure 3.9c show resulting AFM topography and surface images for orthogonal scanning.

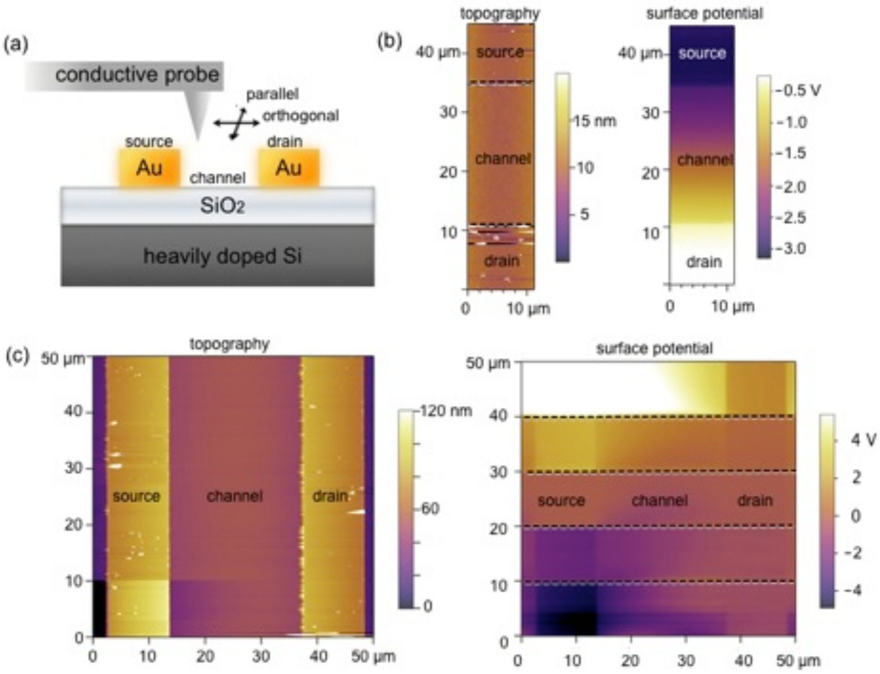

Figure 3.9. SKPM imaging of an empty-channel FET with the cantilever oriented parallel and orthogonal to the source-drain electrodes. (a) Cross-section of a FET showing source and drain electrodes. The heavily doped Si acts as the gate electrode to induce and accumulate charges in the channel. The schematic depicts the cantilever in the orthogonal orientation; the FET was rotated 90° to scan in the parallel direction. **(b)** AFM topography and surface potential images acquired in the parallel orientation. The surface potential image was acquired with a −3.0 V bias voltage applied to the source; the gate was grounded. **(c)** AFM topography and surface potential images acquired in the orthogonal orientation. Varying potential differences between source and drain were collected during the surface potential scan including ±6.0, ±3.0, and 0 V; changes in the applied potentials are marked by dashed lines in the image.

Comparing the known applied potential difference between the source and drain electrodes and the actual surface potential measured allowed for the accuracy to be determined. Line-profiles were extracted for each applied voltage and displayed in Table 3.2.

Table 3.2. Accuracy of measured surface potentials with applied bias to source-drain electrodes in a field-effect transistor: orthogonal vs. parallel scanning

lift height (nm)[a]	applied bias (V)[b]	surface potential (V)[c] orthogonal	surface potential (V)[c] parallel
90	6.00	5.07	5.16
	3.00	2.11	2.33
	0.00	-0.12	-0.37
	-3.00	-2.23	-2.95
	-6.00	-4.61	-5.34
50	6.00	5.27	5.72
	3.00	2.13	2.43
	0.00	-0.15	-0.27
	-3.00	-2.34	-2.86
	-6.00	-4.50	-5.13
10	6.00	5.25	5.35
	3.00	2.16	2.47
	0.00	-0.3	-0.21
	-3.00	-2.64	-2.80
	-6.00	-4.51	-5.07

[a] Denotes the distance between tip and sample.
[b] The applied bias was generated via an external source measure unit.
[c] Measured surface potential was determined by the potential difference between the respective source and drain potentials.

From the results in Table 3.2, two major observations can be elucidated. First, the accuracy of the measurement is much better in the parallel orientation. This is supported by comparing the accuracy of the applied potentials with parallel *vs.* orthogonal scanning at lift heights of 90 nm. The accuracy of the potential in the parallel is 12% higher than the orthogonal direction. This is likely because the cantilever is positioned continually over the gold source drain electrodes in the parallel orientation as it rasters the surface. In the orthogonal configuration, the cantilever is influenced by the both the gold electrodes and the SiO_2 substrate surface, thus the cantilever "feels" the inhomogeneous nature of the surface below it.[97] These observations are consistent with a previous report by Charrier and co-workers. Here, the authors observe changes in the capacitive coupling between both the cantilever and tip and the entire sample depending on their respective orientations.[96] Minimizing this unwanted averaging effect can be achieved by increasing the interaction between the probe tip and the surface immediately below by adjusting the height between tip and sample. For this reason, long probe tips and thinner cantilevers aid in diminishing the averaging effects. Second, the accuracy of the measurement improves with decreasing lift height.[96] This is supported by comparing parallel scanning at lift heights of 90 *vs.* 10 nm. In this case, the accuracy of the applied potential for parallel scanning at a shorter lift height is 8% higher.

SKPM of an ambipolar channel in a TFT. A conductive thin-film of 6.3 nm PbSe QDs was deposited on a FET substrate with an EDT treatment resulting in ambipolar behavior; electron and hole mobilities in the linear regime of the fresh film were $5.4\text{x}10^{-3}$ and $2.6\text{x}10^{-3}$ $\text{cm}^2\ \text{V}^{-1}\ \text{s}^{-1}$, respectively and are consistent with values reported by Liu *et al.*[82] To retain the ambipolar nature of the QD TFT during SKPM measurements, an enclosure was built to achieve air-free measurements using Asylum's Closed Fluid Cell (CFC) modified with inlet and outlet gas purge lines and electrical ports (Figure 3.10a). A fabricated PbSe QD TFT with 10 dips of PbSe QDs (2 mg mL^{-1}) and a 1 mM EDT treatment was loaded into the CFC inside a nitrogen filled glove box and carefully sealed. The CFC containing the TFT was quickly removed from the glovebox and connected to a nitrogen gas purge system using an up-stream 3-way valve for the inlet source and 2-way valve for the downstream outlet. IV curves of the PbSe QD TFT were taken to ensure ambipolar behavior was retained inside the enclosure. Figure 3.10b-e show IV output and transfer plots of the TFT after 45 minutes enclosed in the CFC (typical AFM images take ~45 minutes to acquire). The ambipolar nature of the TFT is retained allowing for investigation of the channel potential with PbSe QDs present. It is noted that the electron mobility decreased by roughly a factor of two while the hole mobility increased by 33%, likely due to slight oxygen exposure after 45 minutes in the CFC.

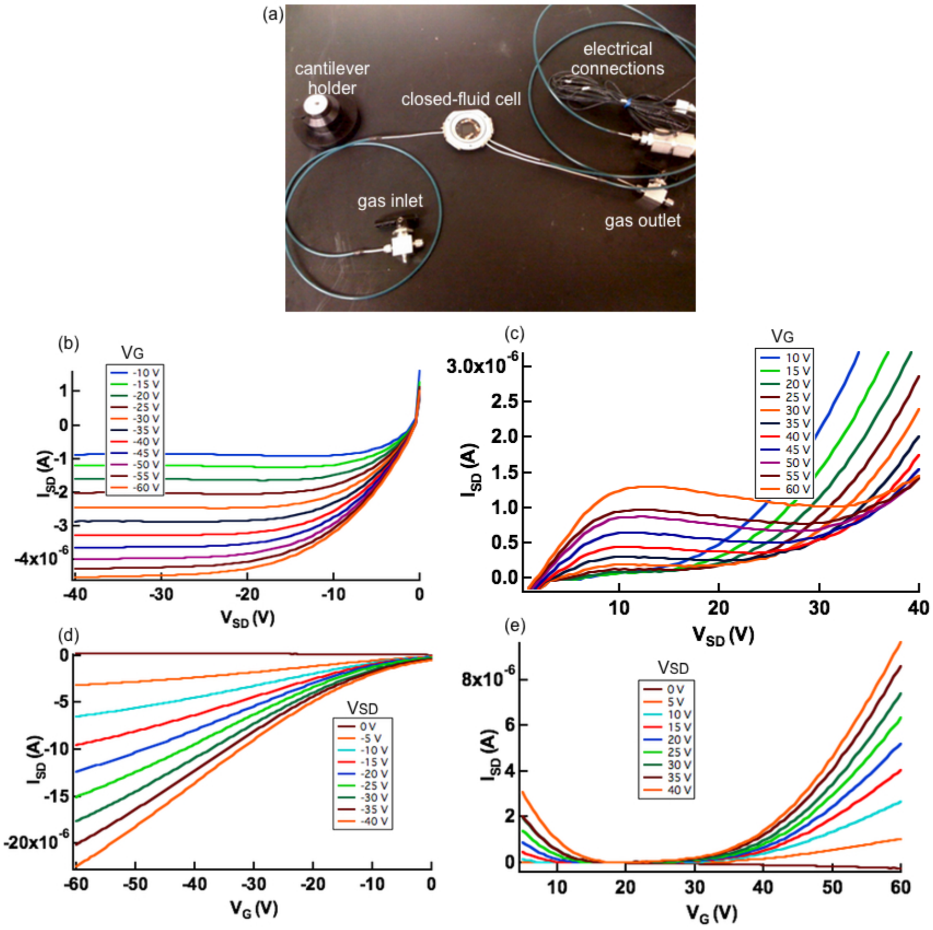

Figure 3.10. (a) Photograph of the modified Asylum Closed Fluid Cell containing gas and electrical ports. IV curves of the 6.3 nm PbSe TFT with an EDT treatment were collected after 45 minutes in the Closed Fluid Cell with continuous purging of nitrogen gas. The plots consist of the following: **(b)** *p*-channel output, **(c)** *n*-channel output**, (d)** *p*-channel transfer, and **(e)** *n*-channel transfer plots.

A series of voltages were applied between the source-drain and gate electrodes with the QD film in the channel; topography and potential images were collected accordingly. Figure 3.10a shows the topography image of the PbSe QD TFT with a 10 μm channel length. The TFT was scanned in the orthogonal orientation because the x-y positioning is constrained by the presence of the CFC, not allowing for enough lateral movement to properly position the TFT in the parallel orientation. The web-like morphology of the PbSe QD film can be observed across the entire channel and areas outside the channel region in the topography image displayed in Figure 3.11a. The source-drain electrodes were inadvertently positioned at a slight angle with respect to the cantilever, unlike the topography image in Figure 3.9. Because of this, line-scans were taken at slight angles to ensure the geometry was perfectly orthogonal. Each line-scan profile was aligned in the x-direction using distinct topographic features to account for drift in the x-direction. Line-scans are displayed for a variety of V_{SD} and V_G in Figure 3.11b. The source and drain electrodes have been drawn for illustration and surface potentials >0 V represent the *n*-channel potential profiles, while surface potentials <0 V are the *p*-channel potential profiles.

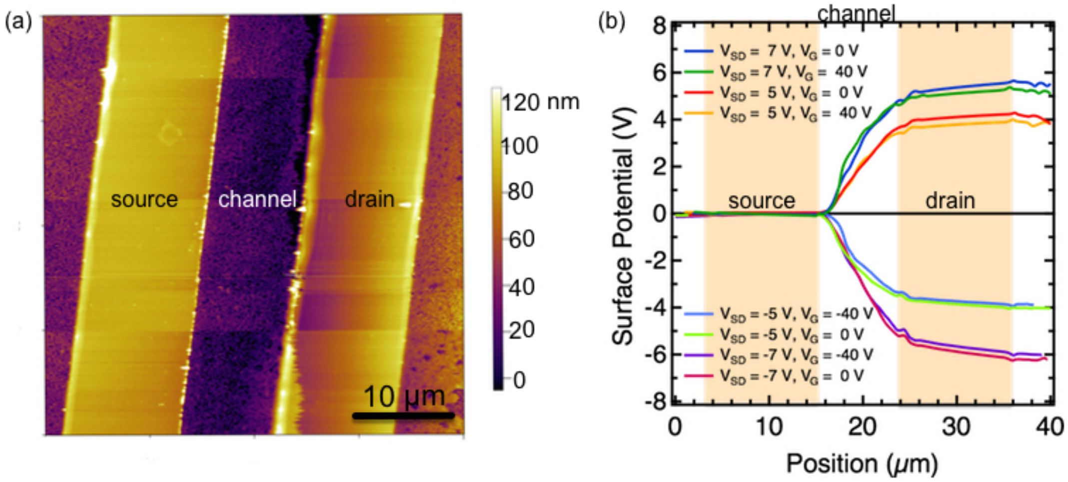

Figure 3.11. SKPM of an ambipolar PbSe QD TFT. (a) AFM topography image showing the source and drain electrodes and the channel containing a thin-film (~40 nm) of EDT treated PbSe QDs with an average diameter of ~6 nm. **(b)** Surface potential line-scans of the TFT in the *n*- and *p*-channel regimes; surface potentials greater than 0 V are the *n*-channel profiles, and vice-versa for the *p*-channel.

The electronics of the Asylum controller have a limitation of the modulation potential, up to ± 10 V, thus $|V_{SD}|$ applied were <10 V. The applied potentials for both the source-drain and gate result in linear behavior of the TFT ($|V_{SD}| << |V_G|$) such that the charge density in the channel is uniform. In both *n*- and *p*-channel operation, the potentials at the source drain electrodes are uniform and relatively flat while the potentials in the channel are sloped. The *p*-channel displays a negative slope from source to drain while the slope becomes positive in the *n*-channel, thus showing a polarity switch corresponding to injection of either holes or electrons at the source drain electrodes. Secondly, the potential profiles are linear from source to drain, indicative of a uniform distribution of charge in both operating regimes. When $|V_{SD}|>>|V_G|$, the charge distribution becomes non-uniform; however, the limitations of the SKPM controller do not allow for us to investigate the channel in this regime due to the restricted modulation of potential (± 10 V) in the electronics of the controller. Nonetheless, SKPM was able to demonstrate direct potential mapping of the conductive channel in a TFT. Furthermore, the operating regime of the TFT coincides well with the resulting potential profiles, showing uniform charge densities for both electrons and holes.

SKPM and other electrical variants of AFM are valuable techniques that can provide a deeper understanding to the working mechanism of devices. Within the literature, many fundamental properties of devices have been investigated with SKPM that can enhance understanding of transport models,[120] locations of potential drops,[121] and contact resistances.[122]

CHAPTER 4

Advancements in CQDSC device architecture and PCEs

Colloidal quantum dot solar cells (CQDSCs) are an emerging PV technology for third generation solar cells that employ quantum confined nanoparticles, specifically PbS and PbSe QDs.[123] Major advancements in power conversion efficiency (PCE) have been achieved over this past decade with record efficiencies currently at 8.6% (independently verified).[30] Historically, PbS and PbSe QDs were of interest as absorber layers in PV devices since these materials demonstrated the capability to produce two or more electron hole pairs per absorbed photon through multiple exciton generation (MEG).[19,22,124] Most signatures of MEG are measured through time-resolved spectroscopy [124] using exclusively solutions and films of QDs and the resulting quantum yields of MEG been heavily debated in the literature.[22] For this reason, unequivocal measurement of MEG can be elucidated through construction of a solar cell that shows an external-quantum efficiency (EQE) greater than 100%. The EQE measures the amount of current generated per photon as a function of wavelength; if MEG were producing two or more electrons per photon, EQEs >100% would be observed.

Before discussing the evolution of device architectures, special attention will be paid in understanding the basic operational principles of solar cells.[9,125] As mentioned in Chapter 1, asymmetry of the device through energetics or kinetics achieves charge separation and diode-like behavior. Upon illumination, an excess of excitons (electron-hole pairs) are created relative to equilibrium conditions in the dark. For efficient photo-harvesting, these excitons need to be *(i)* separated into free electrons and holes *(ii)* transported and collected at the electrodes with minimal radiative and non-radiative recombination events. Depending on the solar cell design, the mechanism by which charge transport and collection occurs through drift or diffusion currents, with or without an electric field present in the absorber layer. The fundamental driving force for generation of an electric field requires an electrical potential gradient at the homo- or heterojunction. In field-free regions, the chemical potential gradient describes the basis for diffusion of carriers.

First, a simple *p-n* homojunction, a common design for crystalline silicon solar cells will be discussed.[9,126] An asymmetry in carrier concentration is created through a junction between a *p*-type and *n*-type material, both in this case are heavily doped crystalline silicon. An excess of holes are present in the *p*-type Si while the *n*-type Si possesses an excess of electrons. A union between *p*-type and *n*-type layers causes the electrons to diffuse to the *p*-type side to equilibrate Fermi energy levels, generating a space-charge region and an electric field. This flow of carriers eventually reaches an equilibrium such that the space charge region is of a finite distance. Within the space-charge region, all the carriers are ionized and travel *via* drift. If the semiconductor is made sufficiently thick, beyond the space charge region carriers travel *via* field-free diffusion, known as the quasi-neutral region. Because crystalline silicon is ultra-pure and virtually defect-free, carrier diffusion lengths are quite long allowing for carriers far away from the junction to diffuse to the space charge region for efficient charge separation and collection. Thus, crystalline solar cells have micron-thick active layers to maximize the amount of light absorption.

In general, to maximize solar harvesting of PbX QD solids it is important the absorber layer accomplish the following:

(1) Absorb as much of the incoming sunlight as possible.[127] Absorption within a solid is governed by the Beer-Lambert law, $I = I_0 e^{-\alpha h v l}$, where I, I_0, and α, are the transmitted light intensity, incident light intensity, absorption coefficient, and film thickness, respectively. QD films need to be sufficiently thick to absorb all the light in the UV and near-infrared region; absorption lengths in the near-infrared region for PbSe QDs are ~500 nm.

(2) Demonstrate excellent carrier transport for enhanced charge extraction at the electrodes. Photo-generated charge carriers need to be effectively transported to the electrode *via* drift and diffusion currents. In the depletion region, carrier drift lengths need to be maximized. In the quasi-neutral region, carrier diffusion length is the important metric to characterize the efficiency of charge transport.[123] Both carrier diffusion and drift lengths are of current interest in maximizing for efficient charge extraction. In one dimension, electronic charge transport can be described by the drift-diffusion equation written for electrons in Equation 4.1.[127,128]

$$J_n = qn(x)\mu_n E(x) + qD_n \frac{dn}{dx} \qquad \textit{Equation 4.1}$$

Here, the first term represents drift-based transport governed by the charge of the electron, q, the electron density, $n(x)$, the electron mobility, μ_n, and the electric field, $E(x)$. The second term describes diffusion-based transport of the electron without the presence of an internal electric field. The average length a carrier travels before recombining can be characterized by the drift length, L_D. Carriers that travel *via* drift and diffusion are described by Equations 4.2 and 4.3,[127] respectively, and τ describes the carrier lifetime.

$$L_D = \mu_n E(x)\tau \qquad \textit{Equation 4.2}$$

$$L_D = \sqrt{\frac{\mu_n k_B T}{q}\tau} \qquad \textit{Equation 4.3}$$

In general, drift lengths are much longer relative to diffusion lengths (1-10 *vs.* 0.1 μm) reported for PbS QDs, thus it is advantageous to create thick depletion regions in devices for enhanced charge extraction.[127] Major efforts are underway in using inorganic or organic small molecules to passivate QD surfaces to remove surface dangling bonds and carrier trap sites.[18,23,30,83,119,129-

[131] These treatments have been shown to improve carrier mobility and lifetimes which likely increases the drift and diffusion lengths in the QD solid, akin to Equations 4.2 and 4.3.

QDs are a versatile material for construction of solar PV devices because they can be synthesized as a function of diameter allowing for engineered light absorption within the device stack. Furthermore, different QD sizes with varying optical band gaps can be used to match other layers in the solar cell for graded junctions or multi-junction solar cells.[132] QDs can be cast from solution using simple manufacturing techniques such as spray- or spin-coating, which are amenable to fabrication of solar cells on flexible substrates.[133] The first architecture that used PbS and PbSe QDs was implemented with a Schottky configuration.[25,37,134] Here, the PbS or PbSe QD layer was inserted between a transparent conducting oxide (indium tin oxide, ITO) and an evaporated metal contact (Figure 4.1a). A Schottky barrier is formed by the junction between a metal and semiconductor, specifically a low work function metal and a *p*-type semiconductor (or a high work function metal and an *n*-type semiconductor). The metal can be considered as heavily doped ($N > 10^{21}$ cm^{-3}), thus most of the band-bending occurs in the semiconducting QD layer. A depletion region is formed in the QD solid as the Fermi energy level of the QD layer aligns with the Fermi energy level of the metal. Photo-generated charge carriers in the QD layer are separated and transported through an electric field formed by the Schottky junction. Initial devices constructed with PbS and PbSe QDs favored the use of low work function metals (Ca, Al or Mg) because QD films tended to be *p*-type.[39]

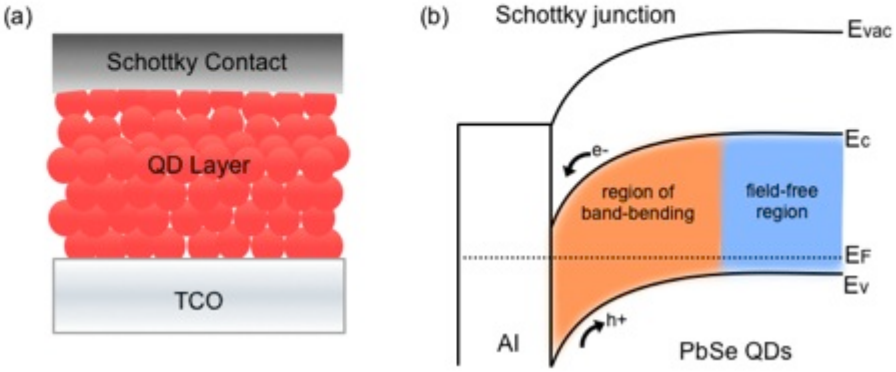

Figure 4.1. Schottky solar cell with PbS or PbSe QDs. (a) Schematic of a Schottky architecture. The QD layer is deposited onto a transparent conducting oxide (TCO) which is an Ohmic contact to the QD layer. Low work function metal contacts such as Al or Ca can be evaporated on top of the QD layer forming a Schottky junction. **(b)** Band diagram illustrating the formation of a Schottky junction between a low work function metal and a *p*-type PbSe QD film. Fermi-level equilibration through band bending of the QD layer creates an internal electric field by which carriers are separated and extracted. The depletion and quasi-neutral regions are illustrated in orange and blue, respectively.

Respectable device efficiencies of Schottky solar cells were reported as high as 5.2% (not independently verified) using 1,4-benzendithiol treated PbS QDs.[135] To observe MEG, the external quantum efficiency (EQE) of the solar cell was characterized. In 2008 report by Luther *et al.* on EDT-treated PbSe QD Schottky devices measured an EQE of 55-65% for wavelengths <700 nm, the region where MEG would be active ($2-3E_G$ for 0.95 eV PbSe QDs).[25] Consequently, the authors conclude that MEG was quenched in the solar cell device. In a separate report by Beard *et al.*, it was determined the EDT treatment to the QD surface substantially reduces the efficiency of MEG.[136] As observed in Figure 4.1b, the electric field is positioned at the back of the device. Absorption of high energy photons at the front of the device produce carriers that need to travel to the back electrode to be efficiently extracted. Furthermore, the barrier heights for Schottky contacts are limited to $\sim 0.5E_G$ which puts a constraint on the maximum voltage of the cell.[137]

For these reasons, architectures evolved to reposition the junction towards the front side of the cell to enhance harvesting of blue-photons. This was accomplished through an *n-p* heterojunction (HJ) architecture, where a *n*-type metal oxide film (TiO_2, ZnO, and CdS) and a *p*-type PbS or PbSe QD film are used to construct the solar cell.[26,28,29] The first certified efficiency for the HJ architecture was placed on the NREL device efficiency chart in 2010 (see Figure 4.2).[29] This structure used an ITO transparent conducting oxide, ZnO nanocrystal (NC) layer, followed by a layer of 1.3 eV PbS QDs that were EDT treated. A gold back contact was thermally evaporated onto the QD layer, and the resulting PCE of the device was 3% (independently verified). The solar cell showed an inverted polarity where electrons were collected at the front electrode and holes at the back contact. In a report by Gao *et al*., an unwanted Schottky barrier between the QD film and the gold electrode was eliminated through insertion of a thin layer of MoOx, an *n*-type transition metal oxide. The MoOx layer serves two functions: *(i)* eliminates Schottky junction formation by Fermi-energy level pinning of the back metal contact and *(ii)* increase the efficiency of hole extraction by injecting electrons into the valence band of the QD layer.[84,138] Device performance was substantially enhanced with the advent of the MoOx layer, which improved V_{OC}, J_{SC} and FF resulting in a certified efficiency of 4.4%.[84]

The next major advance focused on modification of the treatment used during QD film formation. In the previous reports, organic treatments to the QDs including short-chain thiols (ethanedithiol, EDT, and 1,3−benzenedithiol, BDT)[25,53] and small organic acids (mercaptopropionic acid, MPA)[139] were used to improve the film conductivity of the solid by increasing QD-QD coupling in the solar cell. The report in 2011, focused on the use of inorganic treatments to the QD surface motivated by the high mobilities achieved with metal chalcogenide complexes. Tang *et al.* used bulky salts of Cl^-, I^-, and SCN^-species to treat the QDs during solid-state film formation.[130] The authors were able to produce devices with PCEs >5% and reason that inorganic treatments effectively passivate cation rich surface traps enabling high carrier mobility to be achieved. Expanding on the inorganic passivation, in 2012 a hybrid approach[131] was developed to passivate the QD surface with both inorganic and organic ligands, with the exception that the inorganic treatment was accomplished during the synthesis using a $CdCl_2$ treatment. Inorganic metal halide species bind to the surface of the QD in solution and subsequent solid state film formation was accomplished with organic MPA ligands. It is reasoned the hybrid approach allows for the heterogeneous nature of the QD surface to be effectively passivated, resulting in a certified efficiency of 7%.[131] Lastly in 2014, elucidation of the treatments on the energetics of the CQD solid was determined using ultraviolet photoelectron spectroscopy for tertbutylammonium iodide (TBAI) and EDT-capped PbS QDs with an optical gap of 1.3 eV.[30] It was observed that TBAI treated QDs exhibited a deeper work function relative to EDT capped QDs. Thus, the authors capitalized on the difference in energetics for the two treatments to block electron flow from the TBAI treated film to the EDT layer. Thus, a layer of EDT treated PbS QDs were used to replace the MoOx layer to serve as a hole extraction layer along with a Au back contact. Through this band alignment engineering, the authors were able to produce stable solar cells with record breaking efficiencies >8%.[30]

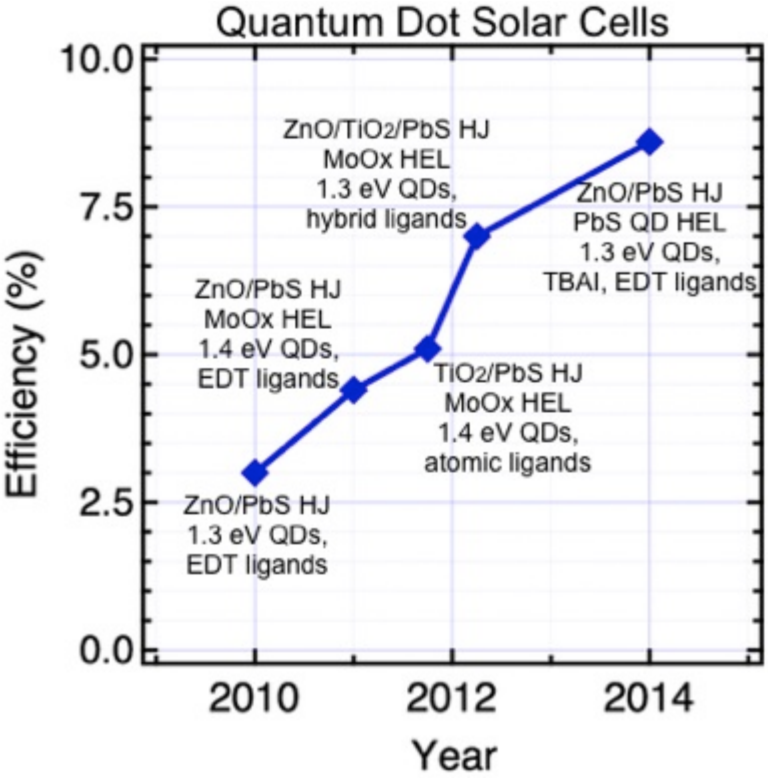

Figure 4.2. Certified efficiency *vs.* year for QD solar cells from the NREL device efficiency chart. Annotations to each of the records have been added to briefly describe the architecture. HJ and HEL stand for heterojunction and hole-extraction layer, respectively. EDT, TBAI, atomic and hybrid ligands detail the surface treatment to the QDs (EDT = ethanedithiol, TBAI = tertbutylammonium iodide, ligands = monovalent Cl^-, I^- and SCN^-, hybrid = synthetic $CdCl_2$ treatment, film formation with mercaptopropionic acid, MPA).

While a rigorous comparison cannot be made for each of the architectures in Figure 4.2, it is interesting to note the correlation of increased fill-factor and short-circuit current density with improved efficiencies. This has often been attributed to improved passivation of the QD surface, paying particular attention to passivation of surface cation or anion species the hybrid approach satisfies.[129-131] The passivation strategies[127,140,141] are still heavily debated within the literature, which could be acting to reduce the amount of recombination within the film or at interfaces. Secondly, improved PCE could be attributed to architecture modifications that allow for enhanced and selective charge extraction at the electrodes.[142] In consideration for future device architectures, integrating the solar flux (AM1.5G solar spectrum) shows that half of the power lies within the infrared region, thus a major challenge exists to efficiently convert this portion of the spectrum into photocurrents. Current record breaking devices typically use small-size PbS QDs (1.3−1.4 eV), thus a major challenge exists to switch to the use of large-size QDs with gaps closer to the near-infrared region. Equating the overall power of the solar cell with the product between voltage and current of the cell under illumination, there exists a trade-off in using a small- or large-sized QDs. Large-sized QDs have small optical gaps (0.7−0.8 eV), and the open-circuit voltage of the solar cells are roughly equal to half of the band-gap, thus typical voltages remain low. Accordingly, use of small-sized QDs dominate the record breaking devices (typically 1.3 eV PbS QDs) due to the higher voltage achieved with larger optical gaps.[30] However, there is an additional advantage in using large-sized QDs because they display better MEG quantum yields[19,22,124] and higher carrier mobility[82] relative to small-sized QDs. Thus, their use in future architectures is further necessitated for enhanced near-infrared capture and potential improvement in photocurrents through generation of two or more electrons per photon. In 2011, a HJ was fabricated using 0.72 eV PbSe QDs with a double treatment of EDT and hydrazine. EQE measurements on the solar cell were 108% in the UV region, demonstrating for the first time unequivocal measurements of MEG.[21] Ongoing efforts are being carried out to realize the full potential of MEG for break through records in device efficiency.

To date, the model used to describe the operation of HJ devices uses a one-side *n-p* junction formalism where the cell operates best when the QD layer is fully depleted (due to small minority carrier diffusion length).[26] By employing solution phase and solid-state passivation treatments to the QDs and modifications to the device architecture for enhanced coupling, PCEs have increased dramatically due to reduction of trap state density and recombination in films. The QD layer is composed of strongly quantum-confined nanoparticles each with discrete energy levels that are electronically-coupled to promote conduction through the array.[143] The collective properties of the array are somewhat akin to a traditional thin film-semiconductor but with tunable band gap determined by the average QD size. It is not known how coupled energy levels translate into band-like energy levels in comparison to traditional bulk semiconductors. In the next section, the discussion will focus on understanding the suggested models for CQDSC operation.

Models for CQDSC operation

The depleted HJ model is the most common explanation for how CQDSCs operate to date.[26,139] Here, physical quantities of the QD solid including free carrier density, quasi-Fermi energy levels, and dielectric constant are averaged over the entire length scale of the solid. Establishment of the depletion region in a QD solid requires that the energy levels of the QDs (discrete, yet coupled states) form band-structure. From here, the energetics and carrier density of the QD solid can be used in the formation of a *p-n* junction with the QD solid as the *p*-type layer, and the ZnO or TiO_2 as the *n*-type layer; band-bending at the heterojunction generates a space-charge region and electric field in the presumably *p*-type film with a low carrier concentration. For full depletion of the QD layer to occur, the carrier concentration in the *n*-type metal oxide layer needs to appreciably exceed the carrier concentration of the PbS QD solid ($N_D >> N_A$).

In contrast, another suggested mechanism of device operation is the excitonic model.[28,144,145] Rather, a Type II HJ is formed between the window layer and QD film with no band bending at the HJ interface. A discontinuity at the conduction and valence band between the window and QD layers allows for photogenerated electrons to efficiently transfer to the ZnO or TiO_2 layer. Within the excitonic model, carriers diffuse *via* photoinduced chemical potential gradient and electron and hole selective layers are used to extract out charge carriers without the aid of an electric field. The major difference between the depleted HJ and excitonic-like model lies in the capability for band-bending to occur at the junction and whether photogenerated carriers in the QD layer travel through either drift or diffusion currents.

Fabrication of CQDSCs

The fabrication of HJ solar cells can be broken down into 4 distinct processes including the *(i)* transparent conducting oxide (TCO), *(ii)* *n*-type metal oxide layer, *(iii)* CQD layer, and finally evaporation of the *(iv)* back contacts. For a more detailed overview of the synthetic conditions for QDs and *n*-type metal oxide layer see Chapter 5.

TCO layer. TCO substrates include tin-doped indium oxide (ITO) and fluorine doped tin oxide (FTO) are available commercially. The substrates are cleaned and sonicated in the following solutions, *(i)* detergent mixed with deionized water, *(ii)* deionized water, and *(iii)* isopropanol for 5 minutes per solution. The substrates are blown dry with nitrogen and placed into an oven at 120 °C overnight to dry.

n-type metal oxide layer. Pre-synthesized ZnO nanocrystals were prepared and dissolved in a solution of chloroform. The layer was deposited using spin-coating methods at typical speeds ~3000 RPM for 30 seconds. The layer was annealed in air at 260 °C for 30 minutes. Film thickness was roughly ~60 nm.

CQD layer. PbS QDs were deposited directly onto the *n*-type metal oxide layer using either dip-coating or spin-coating. Briefly, the substrate is sequentially immersed into a solution of QDs in hexane (2−4 mg mL^{-1}) and a treatment solution of EDT (1 mM) in acetonitrile. This process is repeated until the film reaches the desired thickness (150-350 nm, see Chapter 2 on dip-coating methods). In some cases, mild annealing the QD film in air is performed for short durations (*e.g.* 90 °C for 20 minutes).

Thermal evaporation of back contacts. Pre-prepared TCO/*n*-type metal oxide/CQD film stacks were loaded into a thermal evaporator and back metal contacts including MoOx and Al, Au, or Ag were deposited using shadow masks with final film thicknesses of 10-15 nm and 100-150 nm, respectively; the shadow masks produce solar cells with a 0.11 cm^2 active area.

Characterization of CQDSCs

Figure 4.3a shows a scanning electron microscopy (SEM) image of a CQDSC cross-section highlighting the layers in the stack. Here, the ITO is functioning as a transparent conducting oxide, the ZnO NCs as the *n*-type window layer, PbS QDs as the active layer (E_G = 1.3 eV) and a MoOx/Ag top contact. The morphology of the QD and NC layers are disordered and do not exhibit any long-range order. Figure 4.4b shows current-voltage scans of the device with and without illuminated measurements. A brief introduction to the analysis of illuminated JV curves is discussed in Chapter 1. The dark curve in Figure 4.4b shows rectification near the open-circuit voltage of the cell. Upon illumination, this curve shifts downward with respect to the current-density axis due to formation of photogenerated charge carriers in the PbS QD layer. The short circuit current density, J_{SC}, describes the current density under short-circuit conditions (V = 0 V). The open-circuit voltage (V_{OC}) under illumination can be attributed to the quasi-Fermi energy level difference between the *n*-type and *p*-type materials for a textbook *p-n* junction.[9,125] Conversely, the V_{OC} in a *p-i-n* structure (an intrinsic absorber layer is sandwich between two heavily doped *p*-type and *n*-type layers) can be attributed to the quasi-Fermi energy level difference between electrons and holes in the intrinsic absorber layer.[146] An understanding of the mechanism of device operation is thus required in fully understanding the origins of the V_{OC} in CQDSCs. The fill-factor, *FF*, provides a measure of the power loss occurring in the solar cell through recombination events and resistances in the device.

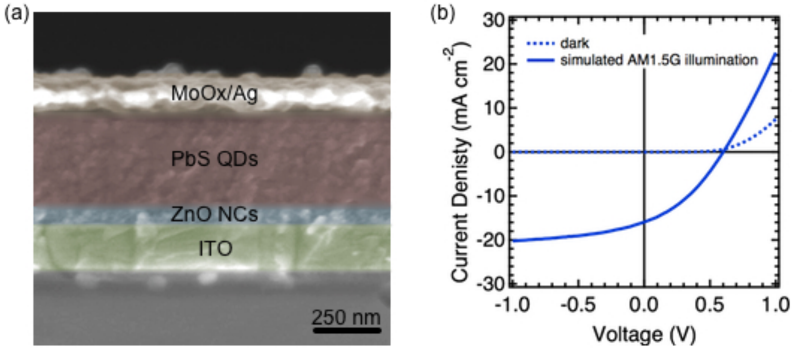

Figure 4.3. (a) A SEM image of a cross-section consisting of a ZnO/PbS heterojunction. The thickness of the individual layers comprise of the following: ITO = 150 nm, ZnO NCs layer = 65 nm, PbS QD layer = 330 nm, and MoOx/Ag = 15 and ~100 nm. **(b)** Current voltage scans of the solar cell with and without simulated illumination at 100 mW/cm^2, which mimics 1-sun illumination. The performance characteristics are as follows: V_{OC} = 600 mV, J_{SC} = 16 mA cm^{-2}, FF = 35%, and η = 3.4%.

CQDSC solar cell operation is often studied with the aid of capacitance voltage (CV) measurements[26] whereby the cell is modeled as a parallel plate capacitor. CV measurements were acquired using an Agilent B2912 source-measurement and an Agilent 4294A impedance analyzer. To perform a proper CV analysis, an equivalent circuit model is used to represent the solar cell which consists of a parallel capacitance (C_P), parallel resistance (R_P), and series resistance (R_S). Verification of the ideality of the circuit can be elucidated through impedance spectroscopy.[147] Figure 4.5a shows an impedance spectrum (imaginary impedance *vs.* real impedance) resembling a semi-circle. The real and imaginary impedance, Z, of the solar cell can be written by Equation 4.4.

$$Z = \left(R_S + \frac{R_P}{1+j\omega R_P C_P}\right) \qquad \textit{Equation 4.4}$$

By fitting the semicircle at each point along the curve to Equation 4.4, the capacitance of the solar cell can be extracted as a function of frequency and applied bias. The extracted capacitance as a function of frequency shows a fairly flat region occurring at frequencies <10^4 Hz, and remains flat for two decades of frequency range (Figure 4.5b). Thus, a 1 kHz frequency was chosen to perform the CV analysis with a voltage range from −1.0 to +0.5 V. The extracted capacitance at 1 kHz is measured between the ITO and back metal contact as a function of applied bias shown in Figure 4.5c.

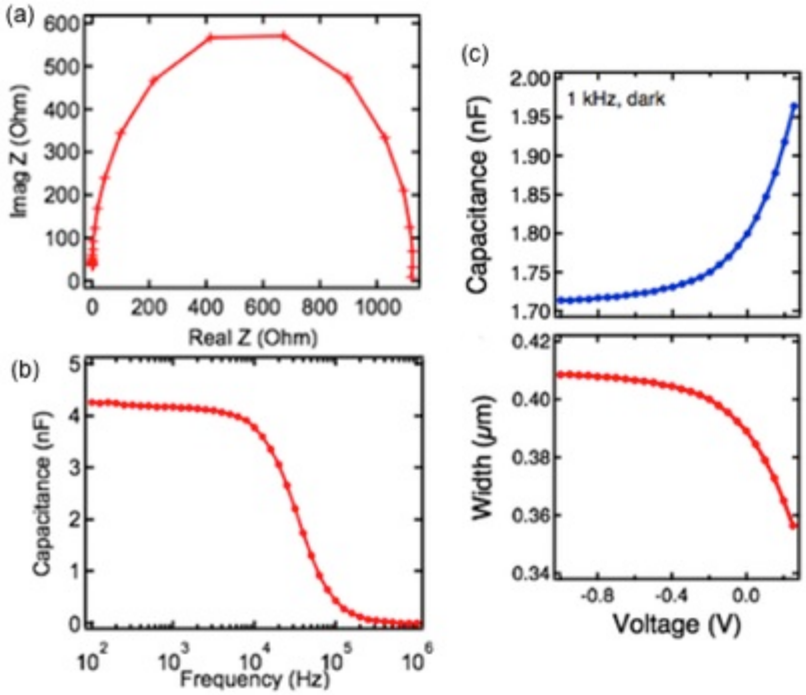

Figure 4.4. Impedance and capacitance voltage measurements on CQDSCs. (a) An impedance plot of the real and imaginary impedance of the solar cell as a function of frequency at 0 V. The impedance spectrum represents a semi-circle which can be used to generate the capacitance. **(b)** The extracted capacitance as a function of frequency. **(c)** The capacitance at 1 kHz as a function of applied voltage. The capacitance can be used to calculate the depletion width of the solar cell.

Using the known area of the cross-section (A), the electric permittivity (ε_0) the dielectric constant for the PbS QD layer (ε) which has been rationalized and previously used within the literature,[54,127] and the layer thickness, the junction capacitance of an *n-p* junction can be described by Equation 4.5, where W represents the depletion region width.[148]

$$C = \frac{\varepsilon\varepsilon_0 A}{W}$$

Equation 4.5

If one further assumes a strongly asymmetrical *n-p* junction (i.e. *N-p* or *n-P* junction), where the carrier concentration (N_D or N_A, the *n*-type or *p*-type layer, respectively) in one layer appreciably exceeds the carrier concentration in the other such that all depletion occurs in the lower doped layer, the capacitance can be re-written as Equation 4.6 with $N_D >> N_A$. Here, V_{BI} and V_a represent the built-in potential of the junction and the applied bias, respectively.

$$C = \frac{A}{2}\sqrt{\frac{2q\varepsilon\varepsilon_0}{V_{BI}-V_a}N_A} \qquad \textit{Equation 4.6}$$

The depletion width in the *p*-type layer is then determined by Equation 4.7.

$$W = \sqrt{\frac{2\varepsilon\varepsilon_0}{qN_A}(V_{BI}-V_a)} \qquad \textit{Equation 4.7}$$

Using Equation 4.7, bias-dependent information such as built-in potential, depletion widths and carrier concentrations of the active layer can be extracted.

From Figure 4.5c, at forward bias >0.5 V, the conductance of the cell increases causing a breakdown in the capacitance of the parallel plate model, therefore, the analysis is restricted to voltages <0.5 V. The behavior in Figure 4.5c shows a fall-off in capacitance with increasing reverse bias ($V_a < 0$ V) can be credited to the increase in the denominator in Equation 4.6, thus reducing the overall capacitance. Additionally, Equation 4.7 states that the depletion width increases with increasing reverse bias to the cell. Accordingly, the depletion width shows an increase in width at bias voltages <0 V. Consistent with previous report of CV measurements on CQDSCs, we observe a depletion width similar in magnitude to the physical thickness of the QD layer.[26] For example, a solar cell constructed with a 330 nm thick PbS QD film shows a measured depletion width of ~350 nm at 0 V, providing convincing evidence for a fully depleted active layer.

The CV analysis is quite complex considering all the layers and interfaces in the solar cell. Furthermore, deep trap states within the semiconductor absorber layer have shown to complicate the CV analysis by creating hysteresis effects in the scanned capacitance.[149] The time scales for trap state filling and de-trapping must be less than the RC time constant utilized in the CV scan. Additionally, use of a static dielectric constant for QDs may not apply such that the dielectric relaxation time must be less than your AC time constant.[150] Furthermore, the MoOx layer possesses many defect states arising from oxygen vacancies which can create trap states that interact with AC field.[30] A rigorous analysis to de-convolute the other layers within the device structure is thus required. Better tools to directly investigate the layers within the stack are needed to provide a deeper understanding of how the devices operate. One such tool discussed in the next chapter is scanning Kelvin probe microscopy, which is used to study device operation of CQDSCs to directly probe the nanoscale electrical potential of the layers in the stack.

CHAPTER 5

Literature highlights of SKPM

Scanning Kelvin probe microscopy (SKPM) offers the capability to directly map work function differences (contact potential difference, CPD) with tens of nanometers resolution as a function of bias, illumination, and environment.[91,151] The relative work function (CPD) difference aids in understanding band offsets between material interfaces in addition to providing a spatial map of potential and electrical field. SKPM has been widely used to study electrical properties of solar cells,[109-113,152-155] field-effect transistors,[122,156,157] light-emitting diodes,[158,159] and heterostructures.[76] A conductive AFM probe is used to directly map surface potentials; for a in-depth discussion of SKPM, refer to Chapter 3. Briefly, as the tip scans over the surface, a feedback system nullifies the contact potential difference between tip and sample by applying a DC voltage directly to the tip, thus providing a direct work function measurement with <50 nm spatial resolution of potential and a 10 mV energy resolution. A background on the use of SKPM in studying solar cells will be covered here.

Exposing and scanning a cross-sectional solar cell with SKPM provides the opportunity to electrically map each individual layer in the device to gain a better understanding of how potentials are distributed throughout the stack. SKPM has been extensively used to characterize fundamental properties of solar cell cross-sections, specifically built-in potentials,[76,110,152,160] locations of *p-n* junctions,[108,112,161] depletion regions, [109,112] photovoltage with white-light illumination,[114,155] and band-structure alignments between hetero-material interfaces.[91,162] Glatzel, *et al.*,[109] used SKPM to study solar cell cross-sections based on CIGSSe absorber and located the *p-n* junction with different buffer layer materials including i-ZnO and an alloy, (Zn,Mg)O inserted between the absorber and *n*-type window layer. Each cross-section containing the intrinsic or alloyed buffer layer was scanned with SKPM, and it was determined the *p-n* junction depletion region was shifted in position towards the absorber layer in the case of the alloyed buffer, thus partly explaining its two-fold increase in photoconversion efficiency (6.3% for i-ZnO buffer *vs.* 12.5% for alloyed buffer). In a related study, CIGSe cross-sections were illuminated with white-light and measured with SKPM.[114] A 50 mV potential at CIGSe grain boundaries was observed with white-light illumination, relative to 150 mV in the dark indicating the grain boundaries may not be as detrimental to solar cell device performance under illuminated conditions. Additionally, Moutinho, *et al.* used SKPM to investigate CdTe/CdS heterojunction solar cells and located depletion and quasi-neutral regions occurring in the device as a function of applied bias.[112] SKPM has gained strong use in the study of electrical properties of surfaces and cross-sectional devices because of it provides direct potential information at the nanoscale and demonstrates flexibility in experimental design.

Research objective and strategy

The best colloidal quantum dot solar cells (CQDSCs) use a *n-p* heterojunction between a *n*-type transparent window layer (TiO_2, ZnO nanocrystals, and others) and a *p*-type film of an array of electronically coupled ~1.3 eV PbS quantum dots (QDs).[30] The power conversion efficiency CQDSCs is increasing from improved passivation strategies to the QD surface and device architecture modifications that allow for efficient charge extraction at interfaces within the device stack. To date, the depleted heterojunction model is often used to describe the operation of CQDSCs. It has been reasoned that band bending in the PbS QD layer at the heterojunction interface creates a space charge region in the presumably *p*-type film, such that all photogenerated charge carries are transported and collected through drift currents.[26,139] It is not known how band bending that occurs in traditional bulk semiconductors will develop within the QD layer that possess quantized yet coupled energy levels. Advancements in device efficiency can likely follow with better understanding how photogenerated carriers are collected at the electrodes, either through drift or diffusion currents.[144] Employing SKPM, the potential difference between a conductive AFM tip and the layers within an operating CQDSC cross-section were mapped to visualize space-charge and quasi-neutral regions. This allows a better understanding of how the device operates as a function of applied bias, illumination and device and how photogenerated charge carriers are collected either through drift or diffusion. In this study, SKPM profiling of CQDSC cross-sections was accomplished as a function of applied bias, illumination, and changes to the device architecture.

Fabrication of heterojunction solar cells with different n-type window layers

ZnO NCs. ZnO NCs were synthesized in a procedure similar to Gao, *et al.*[84] by dissolving 4.4 g of zinc acetate in 200 mL of methanol and heated to 60 °C. A 0.4 M solution of potassium hydroxide in methanol was added drop-wise to the solution of zinc acetate and stirred for 2 hours. The NCs were purified three times, by cycles consisting of centrifugation and re-suspension in methanol. The final product was dissolved in 40 mL of chloroform. A portion of the resulting ZnO NC solution was spin-coated onto patterned ITO glass slides (Thin Film Devices, Anaheim, CA) at 3000 RPM for 30 seconds and then heated on a hotplate in air at 260 °C for 30 minutes.

Sputtered ZnO layer. Preparation of sputtered ZnO layer was accomplished with an AJA International ATC Series 7 target RF-magnetron sputtering system housed in a glove box. Ceramic targets with a copper back plate were used to deposit ZnO onto pre-cleaned ITO substrates. A 7.5% mixture of oxygen in argon was used as the sputtering gas by adjusting the flow of O_2 to 1-20 sccm relative to Ar at 1-50 sccm using separate mass flow controllers. Deposition of a 60 nm ZnO sputtered layer was accomplished at 100 °C, 80 W, and 9 mTorr for the deposition temperature, power, and working pressure, respectively.

TiO_2 layer. The TiO_2 film is prepared according to a report in the literature.[163] Briefly, 125 µL of deionized water is mixed with 5 mL of anhydrous ethanol. The pH of the solution is adjusted to 1

by adding hydrochloric acid, then 375 μL of titanium ethoxide is added. The titanium ethoxide precursor solution is spun directly onto ITO substrates at 1350 RPM and heated to 115 °C for 30 minutes. Final annealing is accomplished by heating in a oven at 350 °C for 30 minutes.

PbS QD layer. PbS QDs were synthesized according to procedure detailed elsewhere[164] with a ~930 nm first exciton and solution phase Cd^{2+} surface treatment. The PbS QD layer (3.5 nm diameter QDs) was deposited using dip-coating in air. Briefly, QD layers were deposited onto the annealed *n*-type window layer of choice in air *via* sequentially immersing the substrate into a suspension of PbS QDs in hexane (10 mg/mL solution) followed by treatment in a 1 mM 1,2-ethanedithiol solution in acetonitrile. This process was repeated until the thickness of the QD film reached the desired thickness, ~200-400 nm. PbS QD films were annealed on a hotplate set at 100 ° C for 30 minutes inside a nitrogen-filled glove box.[83] Top contacts including a 10-15 nm MoO_X followed by a 100 nm thick Al, were thermally evaporated using 0.5-3.0 Å/s rates and 10^{-7}-10^{-6} Torr pressures making an active area of 0.11 cm^2.

Preparation of solar cell cross-sections and SKPM characterization

Solar cell cross-sections were created by scoring a portion of the top metal contact with a diamond scribe followed by mechanical cleaving using glass pliers. The cross-section was lightly blown dry with a nitrogen stream and mounted into a specially designed holder equipped with electrical contacts to apply a bias during measurement (see Figure 5.1a). Magnet wire and colloidal silver paste were used to electrically contact the ITO and metal. To study device operational physics using SKPM, the device must retain its power conversion efficiency in the cross-sectional state. Current-voltage (J-V) characteristics at 1-sun illumination before and after breaking the device were acquired to verify the functionality of the cross-section (Figure 5.1b). Indeed, the device performance was retained upon exposing the cross-section. This particular solar cell had an open-circuit voltage of 602 mV, a short-circuit current of 15.9 mA cm^{-2}, a fill-factor of 35%, and an overall efficiency of 3.4% before mechanical cleaving.

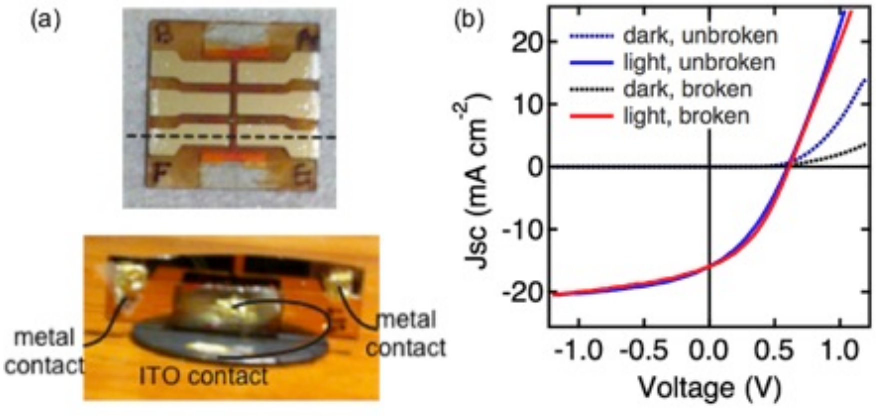

Figure 5.1. Preparation of active solar cell cross-sections. (a) Photographs of an unbroken solar cell chip (top) and a cross-section (bottom). The chip contains six individual solar cells with active areas of 0.11 cm^2; the chip dimension is one square inch. A diamond scribe is used to make a small score mark, ~1/8" in length on the top metal contact away from the active area and in the direction of the dotted line. Glass pliers are used to mechanically cleave along the score mark. The cross-section is mounted into a specially designed holder for SKPM. Small magnet wire (black lines drawn for display) and colloidal silver paste are used to electrically contact the electrodes. **(b)** Current voltage curves at 1-sun illumination (100 mW cm^{-2}) before and after breaking the device. Unbroken and broken annotations denote the state of the device before and after exposing the cross-section, respectively.

Scanning Kelvin probe measurements were performed using an external low-frequency lock-in amplifier (Stanford Research Systems, SR830) and a Park Instrument XE-70 controller system using conductive Pt/Ir coated AFM tips (Budget Sensors, Multi-75EG). Topography was measured at the first resonance frequency (70 kHz) and potential was modulated with a 1.00 V AC bias at 18 kHz. Surface topography and potential were mapped simultaneously in a single pass method with scan rates of 0.2 Hz and image size of 512 x 512 lines and points in ambient conditions. For each device, the ITO was grounded and full images were obtained with the metal biased at ±1.0, ±0.5, and +0 V; open circuit conditions were scanned with the metal wire disconnected. Figure 5.2a shows a schematic illustrating the setup for cross-sectional profiling with SKPM. Here, the cantilever is positioned away from the glass substrate to reduce surface potential averaging effects caused by capacitive coupling between cantilever and sample surface. From the scanning electron microscopy (SEM) and atomic force microscopy (AFM) topography image (Fig. 5.2b,c), the active layers are well-defined upon exposing the cross-section. Additionally, AFM topography images show great correspondence of morphology imaged with SEM. A surface potential image acquired at V_B = +1.0 V has been overlaid onto the topography image in Figure 5.2d to display changes in potential correlated with the morphology of the stack.

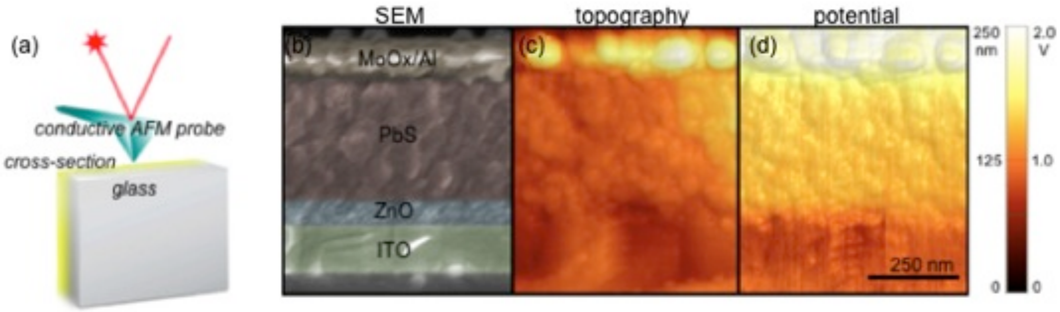

Figure 5.2. (a) Schematic illustrating scanning of a ZnO/PbS heterojunction solar cell cross-section with Kelvin probe microscopy. **(b)** Scanning electron microscopy image of the cross-sectioned solar cell; the individual layers in device stack have been colored for display purposes. Here, the PbS QD layer thickness is ~350 nm. **(c)** Atomic force microscopy topography image of the cross-section scanned in a new location relative to (b). **(d)** Surface potential image acquired at V_B = +1.0 V has been overlaid onto the topography image in (d). Colored scale bar applies to images in (c) and (d); 250-nm scale bar applies to (b), (c), and (d).

Surface potential profiles were extracted by averaging line-scans within a 0.25 μm region in images at each applied bias to generate plots of potential *vs.* position where position represents a vertical cut through all layers in the stack. Electric field profiles were generated by simply taking the first derivative of each potential profile. Figure 5.3a displays the raw surface potential profiles at each applied bias. Each profile represents the convolution of *(i)* contact potential difference between the tip and each layer in the stack, *(ii)* surface charge, and *(iii)* applied bias. The +0-V line profile can be used to account for the effects of contact potential differences between tip and sample and surface charge. Figure 5.3b shows potential profiles with subtraction of the 0-V line profile to determine the effects of applied bias only. In Figure 5.3c, the ITO region was normalized to 0 V since this electrode is grounded during scans. The results and discussion section display potential profiles that have been corrected and normalized in this manner. Finally, Figure 5.3d displays the electric field profiles generated by taking the numerical derivate of each potential profile in Figure 5.3c.

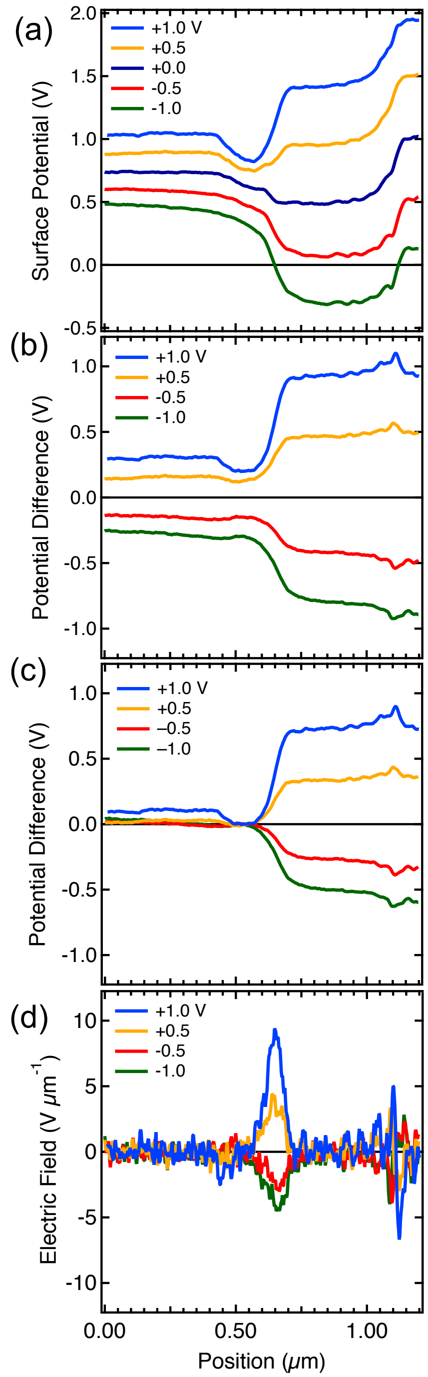

Figure 5.3. Normalization Procedures for SKPM Profiles. (a) Raw surface potential line-scans with applied bias for a solar cell cross-section with a ~350 nm thick PbS layer. **(b)** Surface potential line-profiles with subtraction of the 0-V line-profile. **(c)** Normalization of ITO potentials to 0 V at a position of x = 0.5 μm. **(d)** Electric field profiles generated by taking the first derivative of individual line-scans in (c).

Results and discussion

Figure 5.4 shows potential and electric field profiles for a solar cell cross-section containing 140-nm thick ITO, 65-nm thick ZnO NC layer, 350-nm thick PbS QD layer, and a 15-nm MoOx/100-nm Al top contact. A false-colored SEM image has been rotated and overlaid on the potential profile to identify locations of potential drops within the device stack. With an applied bias $V > 0$ V, the potential profiles show a steep rise in potential and a change in slope in the PbS QD region. For applied biases $V < 0$ V, the potential profiles show a steep drop in the ZnO region and another change in slope in the PbS region. At a specified bias, $V_B = 1$ V for example, the potential difference between the ITO and metal contacts is roughly ~830 mV indicating minimal surface potential averaging effects, a well-known phenomenon within the SKPM technique.

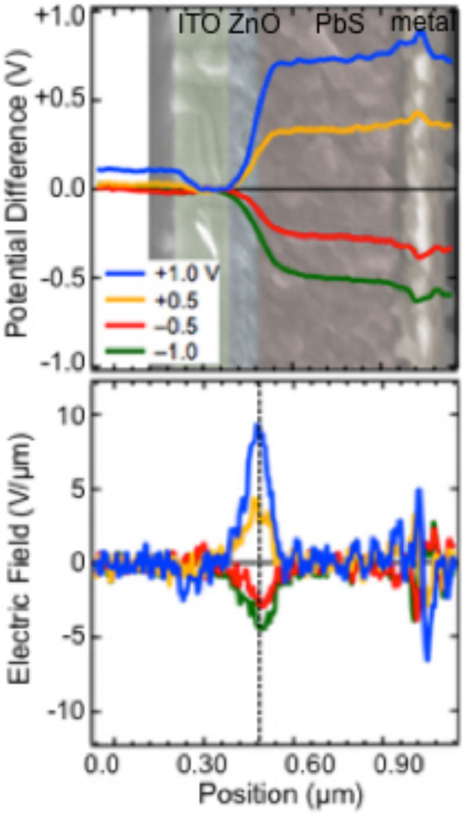

Figure 5.4. Potential and electric field profiles at each applied bias (V_B = ±1.0 and ±0.5 V). A false-colored SEM image of the cross-section has been rotated and inlayed within the potential profile to identify regions of potential drops. Taking the derivative of each respective potential profile created the electric field profiles; a dashed line has been drawn to locate the junction between PbS and ZnO.

The +1.0 V line-profile shows that most of the potential drop (~80%) occurs in the ZnO layer rather than the PbS layer. For all applied voltages, the majority of the potential drop is located in the ZnO NC region, indicating it is the most resistive layer in the stack. Furthermore, comparison of electric field profiles at all biases shows the electric field resides in the ZnO layer, not in the PbS layer. The potential and electric field profiles coupled together suggest the PbS QD layer is not fully depleted, as is typically observed with capacitance voltage (CV) measurements on similar QD solar cells. Many reports have effectively used SKPM to map cross-sectional *p-n* heterojunctions. Moutinho *et al.* observed space-charge and quasi-neutral regions as a function of bias occurring in a CdTe/CdS heterojunction solar cell cross-section thus providing validity for the measuring technique.[112]

To verify the accuracy of the SKPM system, various other solar cell types including a CdTe/ZnO heterojunction and an amorphous silicon *p-i-n* solar cell were scanned with SKPM to show that our AFM system is capable of observing depletion regions, consistent with *p-n* and *p-i-n* operation (see Appendix B, Fig. S1, S2).[153] For an amorphous silicon solar cell cross-section scanned with SKPM, we observe substantial sloping of the potential as a function of applied bias throughout the entire absorber layer, indicating the field region is evenly distributed across the intrinsic amorphous silicon layer. In addition, we prepared and scanned a CdTe/ZnO heterojunction solar cell cross-section with SKPM. We observe a sloped potential in the CdTe layer which indicates band bending, thus providing validity for the measuring technique. More specifically, we are able to locate the *p-n* heterojunction between CdTe and ZnO, and we observe depletion occurring in the CdTe layer. From this, we conclude that our AFM system is capable of showing the existence of depletion regions in active layers in solar cell cross-sections.

To ensure the solar cells studied here displayed typical behavior reported in the literature, we performed CV measurements on solar cell cross-sections at varying QD layer thickness, 200−350 nm. CV measurements were acquired using an Agilent B2912 source-measurement and an Agilent 4294A impedance analyzer using a 1 kHz frequency and a voltage range from -1.0 to +0.5 V; this AC frequency was chosen through a frequency sweep of the capacitance. Figure 5.5a shows a plot of capacitance *vs.* voltage for cross-sections of variable PbS thickness under dark conditions at 1 kHz (the choice of this frequency is discussed in Chapter 4). The thickness of the active layers were verified with cross-sectional SEM. At forward bias >0.5 V, the conductance of the cell increases causing a breakdown in the capacitance of the parallel plate model, therefore, we restrict our analysis to voltages <0.5 V. The capacitance in Figure 5.5a shows a fall-off in capacitance as the cell is scanned with increasing reverse bias. This is consistent with previous reports that show a decreased capacitance with increasing reverse bias.[139] Using known area of the cross-section and the dielectric constant of 12 for PbS, the voltage-dependent depletion width (Figure 5.5b) and carrier concentration estimation, $N_{PbS} = {\sim}4.0 \times 10^{16}$ cm^{-3} were extracted from the CV data. Consistent with previous report of CV measurements on CQDSCs, we observe a depletion width similar in magnitude to the physical thickness of the QD layer. For example, a solar cell constructed with a 200 nm thick PbS QD film shows a measured depletion width of ~200 nm at 0 V, providing convincing evidence for a fully depleted active layer. Thus, the solar cell cross-sections studied here show behavior consistent with the literature.

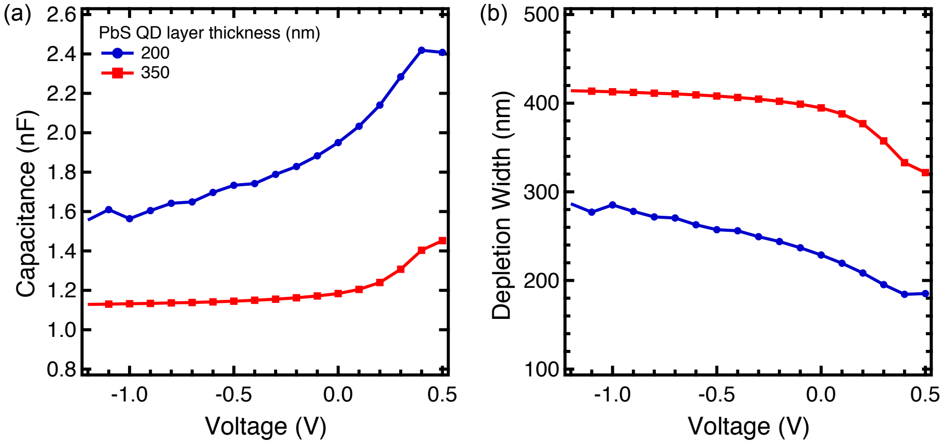

Figure 5.5. Capacitance-voltage measurements on CQDSCs with variable PbS layer thickness (a) Capacitance vs. voltage for 200 and 350 nm thick PbS layers. **(b)** Calculated depletion width for CQDSCs in (a).

To observe the possible existence of space charge and quasi-neutral regions in the PbS QD layer, we prepared and scanned cross-sections with PbS QD layer thicknesses 200, 330, and 850 nm. Figure 5.6 shows cross-sectional potential and electric field profiles on solar cells with variable PbS QD layer thickness, while maintaining the same thickness for ITO, ZnO NCs and top metal contacts. The shape of the potential in the QD region does not change shape appreciably with decreasing or increasing thickness. These profiles show the lack of formation of both a space-charge region and subsequent quasi-neutral region upon extending or shortening the PbS QD layer.

The potential drop for all three cells is localized primarily in the ZnO NC region and the potential remains fairly flat, yet slightly sloped in the PbS QD region. Importantly, most of the potential drop resides in the ZnO NC layer for each profile in Figure 5.6. The potential drop at the PbS/metal interface in Figure 5.6 for the 800-nm thick PbS QD layer cannot be fully explained, but could be due to an increased dipole effects of the MoOx layer.

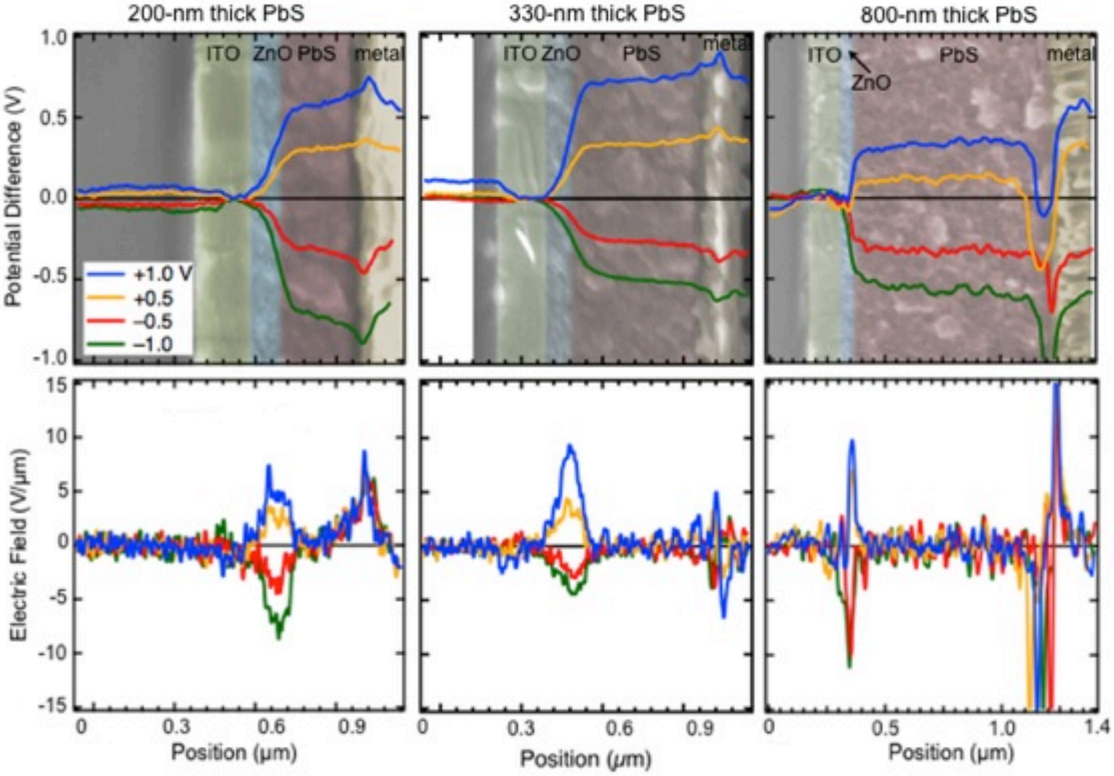

Figure 5.6. PbS QD layer thickness dependence: SKPM potential and electric field profiles as the PbS QD layer is increased in thickness from 200 nm (left), 500 nm (middle) and 850 nm (right). All devices studied utilize the same thickness for ITO, ZnO, and MoOx/Al contacts.

Utilizing Poisson's equations and the electric field profile in Figure 5.4, we can estimate the carrier concentration of ZnO NC layer using Equation 5.1.

$$\frac{dE}{dx} = \frac{\rho}{\varepsilon\,\varepsilon_0} \qquad \textit{Equation 5.1}$$

Here, E is the electric field, ρ is the charge density, ε is the dielectric constant of ZnO (4.4), and ε_0 is the electric permittivity. By integrating Equation 5.2, we can calculate the carrier concentration of ZnO using Equation 5.3, where N_D is the carrier concentration of ZnO, E_{max} represents the maximum electric field in the ZnO from the SKPM profile in Figure 1c, x_n is the depletion region inside the ZnO.

$$N_D = \frac{\varepsilon\, \varepsilon_0 E_{max}}{q x_n} \qquad \textit{Equation 5.2}$$

From this, we calculate the carrier concentration for ZnO to be 2.0x10^{16} cm^{-3}, which is similar in magnitude to the reported carrier concentration for PbS and PbSe QD thin films obtained from CV measurements on heterojunction solar cells. This estimation technique has been utilized previously to estimate the carrier concentration of CdTe using SKPM and has demonstrated good accuracy.[112] These results indicate that the junction cannot be approximated using a one-sided junction formalism whereby the carrier concentration in the *n*-type layer appreciably exceeds the carrier concentration in the PbS layer, resulting in most of the depletion occurring in the lower doped layer. Therefore, the approach to the CV analysis using the one-sided junction approximation cannot be appropriately used.

CQDSC cross-sections were constructed and characterized with SKPM using *n*-type TiO_2 sol-gel and sputtered ZnO layers to verify the nature of the potential drop is not unique to the ZnO NC layer (Figure 5.7). Here, most of the potential drop still occurs in the *n*-type window layer consistent with our previous observations using ZnO NCs.

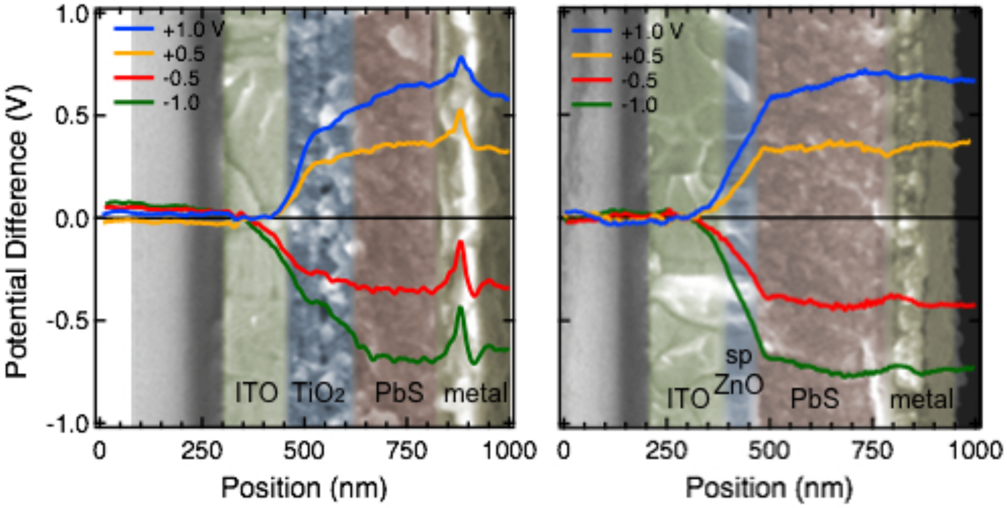

Figure 5.7. SKPM profiles for solar cell cross-section fabricated separately with TiO_2 and sputtered ZnO. The ZnO NC film has been substituted for a ~140 nm thick TiO_2 sol gel film and ~60 nm sputtered ZnO film ("sp ZnO" in the image). The majority of the potential drop resides in the sputtered window oxide layer.

We now distinguish between SKPM measurements with applied bias and illumination. Figure 5.8 shows SKPM profiling of a TiO_2/PbS heterojunction cross-section with illumination from a focused laser (λ = 632 nm) which produces 500 mV (V_{OC} = 510 mV). Four different scans were acquired with the cathode floating or grounded and with the laser turned on or off. From these data, SKPM is capable of discerning the photo-potential of the cell (potential difference between the metal contact under short circuit, dark and open-circuit, illuminated conditions). Accordingly, the photo-potential of the cell under illumination is ~400 mV, which is similar in magnitude to the open-circuit voltage of the cell at 1-sun illumination. Furthermore, applying a bias equal to the voltage the laser produces (500 mV) results in a similar potential profiles (SKPM potential profiles: applied voltage = 0.5 V and open circuit, laser in Figure 5.8). Thus, we can conclude that applying a bias to the solar cell during SKPM measurement allows us to understand device operation with illumination.

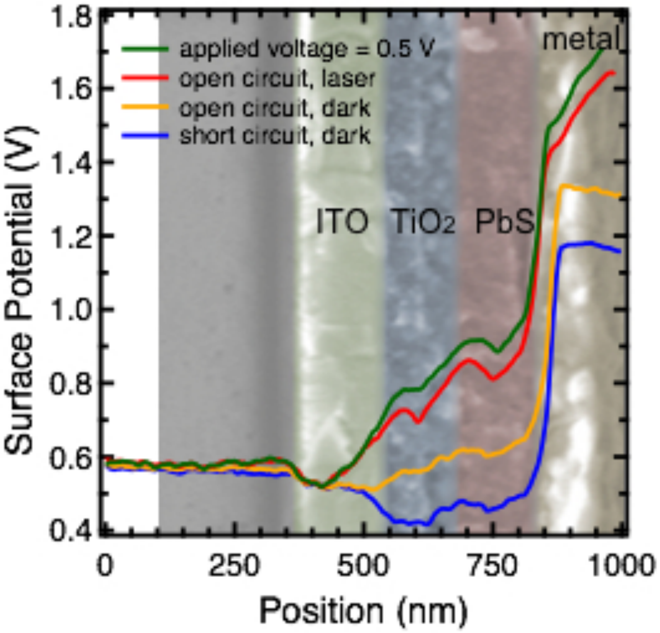

Figure 5.8. SKPM profiling with illumination using a 632-nm focused laser on the cross-section. Four different scans were obtained with the metal cathode floating or grounded and with the laser turned on or off. The photo-potential of the cell as measured with SKPM can be described by the potential difference of the metal in short circuit, dark and open circuit, illuminated conditions.

Here, our SKPM profiling of QD solar cells indicate that the *n*-type window layers used within this work are incapable of generating a strong field in our light-absorbing layer. The carrier concentrations of the *n*-type window layers are too low to create a one-sided *p*-*n* junction. In amorphous silicon solar cells, amorphous heavily doped *p*- and *n*-type contacts are utilized to generate an electric field in the intrinsic amorphous silicon layer, typically 200-300 nm thick such that all photogenerated charges are collected via drift.[146] By depositing an intrinsic amorphous silicon layer on top of our pre-prepared ZnO NC layer and using MoOx/Al contacts, we sought to determine if our contacts were capable of generating a field in a 200 nm thick intrinsic layer (see Appendix B, Figure S3). SKPM profiles of the cross-section containing intrinsic amorphous silicon substituted for the PbS layer show most of the potential drops are located in the contacts rather than in the *a*-Si layer. This indicates our contacts do not have sufficient conductivity to extend a space charge region across the amorphous silicon intrinsic layer.

SKPM was successfully used to study CQDSC cross-sections as a function of applied bias, illumination and device architecture. Understanding of how applied potentials were distributed throughout the stack showed the *n*-type layers are highly resistive, thus limiting the performance of the solar cell. Our results provide the means to better understand how CQDSCs operate which will hopefully enable rational design of forthcoming architectures. By comparing SKPM profiles of many solar cell architectures, we conclude that photogenerated charge carriers are collected primarily *via* diffusion currents. The window layer and MoOx interface allow for selective charge extraction for electrons and holes, respectively. Further optimization of future architectures will require improved selectivity of carrier type and better energetic conduction and valence band alignments. Additionally, the more efficient charge extraction may benefit from enhanced carrier diffusion lengths.

CHAPTER 6

Thesis findings and contributions to the field of CQDSCs

The focus of this thesis was to provide a better understanding of colloidal quantum dots, particularly PbS QDs for solar PV applications. In Chapter 2, the photothermal oxidation of PbS QDs was evaluated as a function of QD diameter, ambient gas (air, 100% nitrogen, or 100% oxygen) and temperature. It was determined the optical blueshifts showed a unique size dependence determined by the competition between oxidation and sintering processes. Development of methods to counter degradation through atomic layer deposition infilling of alumina in the solid allowed for air-stable, and robust PbS QD solids to be fabricated.

In Chapter 3, atomic force microscopy was used to understand the physical and electrical properties of QD arrays including sub-monolayers and thin films. Achieving individual QD resolution in a sub-monolayer film was discussed and explained. Additionally, the film morphology was characterized on technologically-relevant surfaces and was characterized to better understand its influence on charge transport. Scanning Kelvin probe microscopy (SKPM) was used to study devices including an empty-channel field effect transistor. Here, capacitive coupling between the cantilever and device was studied by scanning the channel potential in varying orientations. It was determined the substrate geometry can have a large influence on the measured surface potentials due to changes in capacitive coupling. Finally, scanning of an ambipolar thin-film transistor containing a thin film of conductive PbSe QDs with SKPM under inert atmosphere was discussed and accomplished. Directly imaging the channel potential of the thin-film transistor (TFT) showed conduction of both holes and electrons. Furthermore, a uniform charge distribution was observed consistent with the IV output and transfer characteristics of the TFT in the linear regime. This chapter demonstrated the uniqueness and practicality of AFM and SKPM in studying thin-films and opto-electronic devices with a particular emphasis on coupled PbSe QD arrays.

Chapter 4 covered a brief summary of the progress in power conversion efficiency of colloidal quantum dot solar cells. An discussion of the models of device operation was covered, distinguishing between depleted *vs.* excitonic-like operation. A short section explained how CQDSCs are fabricated and characterized. An in-depth discussion of impedance spectroscopy and capacitance-voltage measurements was summarized. Finally, Chapter 5 demonstrated for the first time mapping of a CQDSC cross-section with SKPM to map local potentials of each layer in the stack as a function of applied bias, illumination and architecture. This technique allows for a direct investigation of how the device operates. SKPM profiles consistently showed the presence of a substantial potential drop in the *n*-type window layer, suggesting field-free regions in the PbS QD layer. These results aid in the fabrication of future device architectures which will require *n*-type window layers with higher carrier concentrations to create a depletion region in the QD layer for enhanced charge extraction.

Outlook and future work

Using SKPM, a full understanding of the channel potential in a TFT as a function of QD surface treatment will allow for a better understanding of passivating treatments and doping of the QD solid. Furthermore, charge transport models developed for QD solids can be better understood with SKPM since this technique directly probes the channel potential, especially correlating the current voltage characteristics and the potential profiles in unipolar or ambipolar TFTs. Finally, a rigorous understanding of CQDSC operation with cross-sectional scanning as a function of QD size will allow for rationalized band engineering the device to enable development of improved architectures.

BIBLIOGRAPHY

1. Executive Office of the President. *The President's Climate Action Plan* (The White House, 2013).
2. International Panel on Climate Change. *Summary for Policy Makers* (Cambridge University Press, Cambridge, New York, 2013).
3. Karl, T. R., Melillo, J. M., Peterson, T. C. *Global climate change impacts in the United States* (Cambridge University Press, 2009).
4. Davis, S. J., Caldeira, K., Matthews, H. D. *Science* **2010**, *329*, 1330–1333.
5. Lewis, N. S., Nocera, D. G. *Proc. Natl. Acad. Sci.* **2006**, *103*, 15729–15735.
6. Crabtree, G. W., Lewis, N. S. *Physics Today* **2007**, *60 (3)*, 37–42.
7. Walter, M. G., Warren, E. L., McKone, J. R., Boettcher, S. W., Mi, Q., Santori, E. A., Lewis, N. S. *Chem Rev* **2010**, *110*, 6446–6473.
8. Green, M. A. *J Mater Sci: Mater Electron* **2007**, *18*, 15–19.
9. Wurfel, P. in *Physics of Solar Cells: From Basic Principles to Advanced Concepts* (Wiley, 2009).
10. Bhubaneswari, P., Iniyan, S., Goic, R. *Renewable and Sustainable Energy Reviews* **2011**, *15*, 1625–1636.
11. Green, M. A., Emery, K., Hishikawa, Y., Warta, W. *Prog. Photovolt: Res. Appl.* **2010**, *18*, 346–352.
12. Ginley, D., Green, M. A., Collins, R. *MRS Bull.* **2008**, *33*, 355–364.
13. Wadia, C., Alivisatos, A. P., Kammen, D. M. *Environ. Sci. Technol.* **2009**, *43*, 2072–2077.
14. Timilsina, G. R., Kurdgelashvili, L., Narbel, P. A. *Renewable and Sustainable Energy Reviews* **2012**, *16*, 449–465.
15. Shockley, W., Queisser, H. J. *J. Appl. Phys.* **1961**, *32*, 510.
16. Moreels, I., Lambert, K., Smeets, D., De Muynck, D., Nollet, T., Martins, J., C., Vanhaecke, F., Vantomme, A., Delerue, C., Allan, G., Hens, Z. *ACS NANO* **2009**, *3*, 3023–3030.
17. Wise, F. W. *Acc. Chem. Res.* **2000**, *33*, 773–780.
18. Smith, A. M., Nie, S. *Acc Chem Res* **2010**, *43*, 190–200.
19. Ellingson, R. J., Beard, M. C., Johnson, J. C., Yu, P., Micic, O. I., Nozik, A. J., Shabaev, A., Efros, A. L. *Nano Lett* **2005**, *5*, 865–871.
20. Beard, M. C., Midgett, A. G., Hanna, M. C., Luther, J. M., Hughes, B. K., Nozik, A. J. *Nano Lett* **2010**, *10*, 3019–3027.
21. Semonin, O. E., Luther, J. M., Choi, S., Chen, H. Y., Gao, J., Nozik, A. J., Beard, M. C. *Science* **2011**, *334*, 1530–1533.
22. Nozik, A. J., Beard, M. C., Luther, J. M., Law, M., Ellingson, R. J., Johnson, J. C. *Chem. Rev.* **2010**, *110*, 6873–6890.
23. Liu, Y., Tolentino, J., Gibbs, M., Ihly, R., Perkins, C. L., Liu, Y., Crawford, N., Hemminger, J. C., Law, M. *Nano Lett.* **2013**, *13*, 1578–1587.
24. Tang, J., Wang, X., Brzozowski, L., Barkhouse, D. A. R., Debnath, R., Levina, L., Sargent, E., H. *Adv. Mater.* **2010**, *22*, 1398.
25. Luther, J. M., Law, M., Beard, M. C., Song, Q., Reese, M. O., Ellingson, R. J., Nozik, A. J. *Nano Lett.* **2008**, *8*, 3488–3492.
26. Pattantyus-Abraham, A. G., Kramer, I. J., Barkhouse, A. R., Wang, X., Konstantatos, G., Debnath, R., Levina, L., Raabe, I., Nazeeruddin, M. K., Gratzel, M., Sargent, E. H. *ACS Nano* **2010**, *4*, 3374–3380.
27. Gao, J., Luther, J. M., Semonin, O. E., Ellingson, R. J., Nozik, A. J., Beard, M. C. *Nano Lett.*

2011, *11*, 1002–1008.
28. Leschkies, K., S., Beatty, T., J., Kang, M. S., Norris, D., J., Aydil, E., S. *ACS Nano* **2009**, *3*, 3638–3648.
29. Luther, J. M., Gao, J., Lloyd, M. T., Semonin, O. E., Beard, M. C., Nozik, A. J. *Adv. Mater.* **2010**, *22*, 3704–3707.
30. Chuang, C. H., Brown, P. R., Bulovic, V., Bawendi, M. G. *Nat. Mater.* **2014**,
31. Leschkies, K., S., Kang, M. S., Aydil, E., S., Norris, D., J. *J. Phys. Chem. C* **2010**, *114*, 9988–9996.
32. Ding, B., Shi, M., Chen, F., Zhou, R., Deng, M., Wang, M., Chen, H. *J. of Crys. Growth* **2009**, *311*, 1533–1538.
33. Hines, M. A., Scholes, G. D. *Adv. Mater.* **2003**, *15*, 1844–1849.
34. Reiss, P. in *Semiconductor Nanocrystal Quantum Dots* 35-72 (Springer, 2008).
35. Rempel, J. Y., Bawendi, M. G., Jensen, K. F. *J. Am. Chem. Soc.* **2009**, *131*, 4479–4489.
36. Nair, P. S., Fritz, K. P., Scholes, G. D. *Small* **2007**, *3*, 481–487.
37. Koleilat, G., I., Levina, L., Shukla, H., Myrskog, S., H., Hinds, S., Pattantyus-Abraham, A., G., Sargent, E., H. *ACS Nano* **2008**, *2*, 833–840.
38. Justo, Y., Moreels, I., Lambert, K., Hens, Z. *Nanotech.* **2010**, *21*, 295606.
39. Luther, J. M., Law, M., Song, Q., Perkins, C. L., Beard, M. C., Nozik, A. J. *ACS Nano* **2008**, *2*, 271–280.
40. Baumgardner, W. J., Choi, J. J., Lim, Y. F., Hanrath, T. *J. Am. Chem. Soc.* **2010**, *132*, 9519–9521.
41. Zarghami, M., H., Liu, Y., Gibbs, M., Gebremichael, E., Webster, C., Law, M. *ACS Nano* **2010**, *4*, 2475–2485.
42. Marin, J. L., Riera, R., Cruz, S. A. *J. Phys. Condens. Matter* **1998**, *10*, 1349–1361.
43. Norris, D., J. in *Nanocrystal Quantum Dots* (ed Klimov, V. I.) (CRC Press, 2010).
44. Kim, J., Wong, C. Y., Scholes, G. D. *Acc. Chem. Res.* **2009**, *42*, 1037–1046.
45. Williams, K. J., Tisdale, W. A., Leschkies, K. S., Haugstad, G., Norris, D. J., Aydil, E. S., Zhu, X. Y. *ACS Nano* **2009**, *3*, 1532–1538.
46. Sykora, M., Koposov, A., Y., McGuire, J., A., Schulze, R., K., Tretiak, O., Pietryga, J., M., Klimov, V., I. *ACS Nano* **2010**, *4*, 2021–2034.
47. Law, M., Beard, M., C., Choi, S., Luther, J., M., Hanna, M., C., Nozik, A., J. *Nano Lett.* **2008**, *8*, 3904–3910.
48. Dai, Q., Zhang, Y., Wang, Y., Wang, Y., Zou, B., Yu, W., W., Hu, M., Z. *J. Phys. Chem. C* **2010**, *114*, 16160–16167.
49. Peterson, J. J., Krauss, T. D. *Phys. Chem. Chem. Phys.* **2006**, *8*, 3851.
50. Stouwdam, J. W., Shan, J., van, V., Frank C. J. M., Pattantyus-Abraham, A. G., Young, J. F., Raudsepp, M. *J. Phys. Chem. C* **2007**, *111*, 1086–1092.
51. Blackburn, J. L., Chappell, H., Luther, J. M., Nozik, A. J., Johnson, J. C. *J. Phys. Chem. Lett.* **2011**, *2*, 599–603.
52. Law, M., Luther, J. M., Song, O., Hughes, B.K., Perkins, C. L., Nozik, A. J. *J. Am. Chem. Soc.* **2008**, *130*, 5974–5985.
53. Liu, Y., Gibbs, M., Perkins, C. L., Tolentino, J., Zarghami, M. H., Bustamante, J. J., Law, M. *Nano Lett.* **2011**, *11*, 5349–5355.
54. Tang, J., Brzozowski, L., Barkhouse, D. A., Wang, X., Debnath, R., Wolowiec, R., Palmiano, E., Levina, L., Pattantyus-Abraham, A. G., Jamakosmanovic, D., Sargent, E. H. *ACS Nano* **2010**, *4*, 869–878.
55. Schapotschnikow, P., van Huis, M., A., Zandbergen, H., W., Vanmaekelbergh, D., Vlugt, T., J. H. *Nano Lett.* **2010**, *10*, 3966–3971.

56. van Huis, M., A., Kunneman, L., T., Overgaag, K., Xu, Q., Pandraud, G., Zandbergen, H., W., Vanmaekelbergh, D. *Nano Lett.* **2008**, *8*, 3959–3963.
57. Lee, B., Podsiadlo, P., Rupich, S., Talapin, D. V., Rajh, T., Shevchenko, E. V. *J. Am. Chem. Soc.* **2009**, *131*, 16386–16388.
58. Mentzel, T. S., Porter, V. J., Geyer, S., MacLean, K., Bawendi, M. G., Kastner, M. A. *Phys. Rev. B* **2008**, *77*, 075316.
59. Lü, W., Yamada, F., Kamiya, I. *J. Vac. Sci. Technol. B* **2010**, *28*, C5E8.
60. Turyanska, L., Elfurawi, U., Li, M., Fay, M. W., Thomas, N. R., Mann, S., Blokland, J. H., Christianen, P. C., Patane, A. *Nanotech.* **2009**, *20*, 315604.
61. Groner, M. D., Fabreguette, F. H., Elam, J. W., George, S. M. *Chem. Mat.* **2004**, *16*, 639–645.
62. Hyde, G. K., McCullen, S. D., Jeon, S., Stewart, S. M., Jeon, H., Loboa, E. G., Parsons, G. N. *Biomed. Mater.* **2009**, *4*, 025001.
63. Klaus, J. W., Sneh, O., George, S. M. *Science* **1997**, *278*, 1934–1936.
64. Knez, M., Kadri, A., Wege, C., Gosele, U., Jeske, H., Nielsch, K. *Nano Lett.* **2006**, *6*, 1172–1177.
65. Knez, M., Niesch, K., Niinistoe, L. *Adv. Mater.* **2007**, *19*, 3425–3438.
66. Liang, X., King, D., M., Li, P., Weimer, A., W. *J. Am. Chem. Soc.* **2009**, *92*, 649–654.
67. Luo, Y., Slater, D., Han, M., Moryl, J., Osgood, R. M. *Appl. Phys. Lett.* **1997**, *71*, 3799–3801.
68. Meyer, J., Schneidenbach, D., Winkler, T., Hamwi, S., Weimann, T., Hinze, P., Ammermann, S., Johannes, H. H., Riedl, T., Kowalsky, W. *Appl. Phys. Lett.* **2009**, *94*, 233305.
69. Nanu, M., Schoonman, J., Goossens, A. *Adv. Mater.* **2004**, *16*, 453–456.
70. Pourret, A., Guyot-Sionnest, P., Elam, J., W. *Adv. Mater.* **2009**, *21*, 232.
71. Binnig, G., Gerber, C., Stoll, E., Albrecht, T. R., Quate, C. F. *Europhys. Lett.***1987**, *3*, 1281.
72. Binnig, G., Quate, C. F., Gerber, C. *Phys. Rev. Lett.* **1986**, *56*, 930.
73. Yablon, D. G. in *Scanning Probe Microscopy for Industrial Applications: Nanomechanical Characterization* (Wiley, 2013).
74. Hurley, D. C., Killgore, J. P. in *Scanning Probe Microscopy for Industrial Applications: Nanomechanical Characterization* (Wiley, 2013).
75. Jacobs, T. D. B., Mate, C. M., Turner, K. T., Carpick, R. W. in *Scanning Probe Microscopy for Industrial Applications: Nanomechanical Characterization* (Wiley, 2013).
76. Nanayakkara, S. U., Cohen, G., Jiang, C. S., Romero, M. J., Maturova, K., Al-Jassim, M., van de Lagemaat, J., Rosenwaks, Y., Luther, J. M. *Nano Lett.* **2013**, *13*, 1278–1284.
77. Hopster, H. *Magnetic Microscopy of Nanostructures* (Springer, 2005).
78. Kalinin, S. V., Gruverman, A. in *Scanning Probe Microscopy: Electrical and Electromechanical Phenomena at the Nanoscale* (Springer, 2007).
79. Hillier, A. C., Bard, A. J. *Rev. Sci. Instrum.* **1997**, *68*, 2082.
80. García, R., Perez, R. *Surf. Sci. Rep.* **2002**, *47*, 197–301.
81. Gui, C., Elwenspoek, M., Tas, N.,Gardeniers, J. G. E. *J. Appl. Phys.* **1999**, *85*, 7448.
82. Liu, Y., Gibbs, M., Puthussery, J., Gaik, S., Ihly, R., Hillhouse, H. W., Law, M. *Nano Lett.* **2010**, *10*, 1960–1969.
83. Gao, J., Jeong, S., Lin, F., Erslev, P. T., Semonin, O. E., Luther, J. M., Beard, M. C. *Appl. Phys. Lett.* **2013**, *102*, 043506.
84. Gao, J., Perkins, C., L., Luther, J., M., Hanna, M., C., Chen, H.-Y., Semonin, O., E., Nozik, A., J., Ellingson, R., J., Beard, M., C. *Nano Lett.* **2011**, *11*, 3263–3266.
85. Baumgardner, W. J., Whitham, K., Hanrath, T. *Nano Lett.* **2013**, *13*, 3225–3231.
86. Schmid, G. *Nanoparticles: From Theory to Application* (Wiley, 2011).
87. Klokkenburg, M., Houtepen, A. J., Koole, R., de Folter, J. W., Erne, B. H., van Faassen,

E.,Vanmaekelbergh, D. *Nano Lett.* **2007**, *7*, 2931–2936.
88. Cho, S. H., Lee, S., Ku, D. Y., Lee, T. S., Cheong, B., Kim, W. M., Lee, K. S. *Thin Solid Films* **2004**, *447-448*, 68–73.
89. Castro-Rodriguez, R., Oliva, A. I., Sosa, V., Caballero-Briones, F., Pena, J. L. *Appl. Surf. Sci.* **2000**, *161*, 340–346.
90. Kelley, T. W., Granstrom, E., Frisbie, C. D. *Adv. Mater.* **1999**, *11*, 261–264.
91. Balke, N., Bonnell, D., Ginger, D. S., Kemerink, M. *MRS Bull.* **2012**, *37*, 633–637.
92. Lee, D. T., Pelz, J. P., Bhushan, B. *Nanotech.* **2006**, *17*, 1484.
93. Coffey, D. C., Reid, O. G., Rodovsky, D. B., Bartholomew, G. P., Ginger, D. S. *Nano Lett.* **2007**, *7*, 738–744.
94. Maragliano, C., Lilliu, S., Dahlem, M. S., Chiesa, M., Souier, T., Stefancich, M. *Sci Rep.* **2014**, *4*, 4203.
95. Melitz, W., Shen, J., Kummel, A. C.,Lee, S. *Surf. Sci. Rep.* **2011**, *66*, 1–27.
96. Charrier, D. S., Kemerink, M., Smalbrugge, B. E., de Vries, T., Janssen, R. A. *ACS Nano* **2008**, *2*, 622–626.
97. Jacobs, H. O., Leuchtmann, P., Homan, O. J., Stemmer, A. *J. Appl. Phys.* **1998**, *84*, 1168–1173.
98. Krok, F., Sajewicz, K., Konior, J., Goryl, M., Piatkowski, P., Szymonski, M. *Phys. Rev. B* **2008**, *77*, 235427.
99. Zerweck, U., Loppacher, C., Otto, T., Grafström, S.,Eng, L. *Phys. Rev. B* **2005**, *71*,
100. Li, G., Mao, B., Lan, F., Liu, L. *Review of Scientific Instruments* **2012**, *83*, 113701.
101. Yu, Y. J., Zhao, Y., Ryu, S., Brus, L. E., Kim, K. S., Kim, P. *Nano Lett.* **2009**, *9*, 3430–3434.
102. Ellison, D. J., Kim, J. Y., Stevens, D. M., Frisbie, C. D. *J. Am. Chem. Soc.* **2011**, *133*, 13802–13805.
103. Hoppe, H., Glatzel, T., Niggemann, M., Hinsch, A., Lux-Steiner, M. C., Sariciftci, N. S. *Nano Lett.* **2005**, *5*, 269–274.
104. Ishii, H., Hayashi, N., Ito, E., Washizu, Y., Sugi, K., Kimura, Y., Niwano, M., Ouchi, Y., Seki, K. *Phys. Stat. Sol. (a)* **2004**, *201*, 1075–1094.
105. Koren, E., Hyun, J. K., Givan, U., Hemesath, E. R., Lauhon, L. J., Rosenwaks, Y. *Nano Lett.* **2011**, *11*, 183–187.
106. Xu, T., Venkatesan, S., Galipeau, D., Qiao, Q. *Solar Energy Materials and Solar Cells* **2013**, *108*, 246–251.
107. Chiesa, M., Burgi, L., Kim, J. S., Shikler, R., Friend, R. H., Sirringhaus, H. *Nano Lett.* **2005**, *5*, 559–563.
108. Doukkali, A., Ledain, S., Guasch, C., Bonnet, J. *Appl. Surf. Sci.* **2004**, *235*, 507–512.
109. Glatzel, T., Steigert, H., Sadewasser, S., Klenk, R., Lux-Steiner, M. C. *Thin Solid Films* **2005**, *480-481*, 177–182.
110. Jiang, C.-S., Moutinho, H. R., Friedman, D. J., Geisz, J. F., Al-Jassim, M. M. *J. Appl. Phys.* **2003**, *93*, 10035–10040.
111. Jiang, C. S., Ptak, A., Yan, B., Moutinho, H. R., Li, J. V., Al-Jassim, M. M. *Ultramicroscopy* **2009**, *109*, 952–957.
112. Moutinho, H. R., Dhere, R. G., Jiang, C.-S., Yan, Y., Albin, D. S., Al-Jassim, M. M. *J. Appl. Phys.* **2010**, *108*, 074503.
113. Yang, C., Pyekh, Y., Danyluk, S. *Solar Energy Materials and Solar Cells* **2012**, *102*, 167–172.
114. Zhang, Z., Hetterich, M., Lemmer, U., Powalla, M., Holscher, H. *Appl. Phys. Lett.* **2013**, *102*, 023903.
115. Wang, Z., Zhang, N., Brenneman, K., Wu, T. C., Jung, H., Biswas, S., Sen, B., Reinhardt, K.,

Liao, S., Stroscio, M. A., Dutta, M. in *Quantum Dot Devices* (Springer, 2012).
116. Kagan, C. R., Andry, P. *Thin-Film Transistors* (CRC Press, 2003).
117. Mole, P. J., Rorison, J. M., del Alamo, J. A., Lancefield, D. in *Properties of Crystalline Silicon* (INSPEC, 1999).
118. Ridley, B. A., Nivi, B., Jacobson, J. M. *Science* **1999**, *286*, 746–749.
119. Talapin, D. V., Murray, C. B. *Science* **2005**, *310*, 86–89.
120. Smits, E. C. P,, Mathijssen, S. G. J., Cölle, M., Mank, A. J. G., Bobbert, P. A., Blom, P. W. M., de B., Bert, de Leeuw, D. M. *Phys. Rev. B* **2007**, *76*, 125202.
121. Pingree, L. S., Rodovsky, D. B., Coffey, D. C., Bartholomew, G. P., Ginger, D. S. *J. Am. Chem. Soc.* **2007**, *129*, 15903–15910.
122. Bürgi, L., Sirringhaus, H., Friend, R. H. *Appl. Phys. Lett.* **2002**, *80*, 2913.
123. Sargent, E. H. *Nature Photonics* **2012**, *6*, 133–135.
124. Beard, M. C., Ellingson, R. J. *Laser & Photon. Rev.* **2008**, *2*, 377–399.
125. Wurfel, P. *Physics of Solar Cells: From Basic Principles to Advanced Concepts* (Wiley, 2009).
126. Dimova-Malinovska, D. **2010**, *Journal of Physics: Conference Series 253(1)*, 012007.
127. Tang, J., Sargent, E. H. in *Colloidal Quantum Dot Optoelectronics and Photovoltaics* (Cambridge, 2013).
128. Sze, S. M., Kwok, K. N. *Physics of Semiconductor Devices* (Wiley, 2006).
129. Ning, Z., Ren, Y., Hoogland, S., Voznyy, O., Levina, L., Stadler, P., Lan, X., Zhitomirsky, D., Sargent, E. H. *Adv. Mater.* **2012**, *24*, 6295–6299.
130. Tang, J., Kemp, K. W., Hoogland, S., Jeong, K. S., Liu, H., Levina, L., Furukawa, M., Wang, X., Debnath, R., Cha, D., Chou, K. W., Fischer, A., Amassian, A., Asbury, J. B., Sargent, E. H. *Nat. Mater.* **2011**, *10*, 765–771.
131. Ip, A. H., Thon, S. M., Hoogland, S., Voznyy, O., Zhitomirsky, D., Debnath, R., Levina, L., Rollny, L. R., Carey, G. H., Fischer, A., Kemp, K. W., Kramer, I. J., Ning, Z., Labelle, A. J., Chou, K. W., Amassian, A., Sargent, E. H. *Nat. Nanotechnol.* **2012**, *7*, 577–582.
132. Wang, X., Koleilat, G. I., Tang, J., Liu, H., Kramer, I. J., Debnath, R., Brzozowski, L., Barkhouse, D. A. R., Levina, L., Hoogland, S., Sargent, E. H. *Nature Photon.* **2011**, *5*, 480–484.
133. Sargent, E. H. *Nature Photon.* **2009**, *3*, 325–331.
134. Clifford, J. P., Johnston, K. W., Levina, L., Sargent, E. H. *Appl. Phys. Lett.* **2007**, *91*, 253117.
135. Piliego, C., Protesescu, L., Bisri, S. Z., Kovalenko, M. V., Loi, M. A. *Energy Environ. Sci.* **2013**, *6*, 3054.
136. Beard, M. C., Midgett, A. G., Law, M., Semonin, O. E., Ellingson, R. J., Nozik, A. J. *Nano Lett.* **2009**, *9*, 836–845.
137. Zhao, N., Osedach, T. P., Chang, L. Y., Geyer, S. M., Wanger, D., Binda, M. T., Arango, A. C., Bawendi, M. G., Bulovic, V. *ACS Nano* **2010**, *4*, 3743–3752.
138. Brown, P. R., Lunt, R. R., Zhao, N., Osedach, T. P., Wanger, D. D., Chang, L. Y., Bawendi, M. G., Bulovic, V. *Nano Lett.* **2011**, *11*, 2955–2961.
139. Barkhouse, D. A., Debnath, R., Kramer, I. J., Zhitomirsky, D., Pattantyus-Abraham, A. G., Levina, L., Etgar, L., Gratzel, M., Sargent, E. H. *Adv. Mater.* **2011**, *23*, 3134–3138.
140. Kramer, I. J., Sargent, E. H. *Chem. Rev.* **2014**, *114*, 863–882.
141. Talapin, D. V., Lee, J. S., Kovalenko, M. V., Shevchenko, E. V. *Chem. Rev.* **2010**, *110*, 389–458.
142. Mora-Sero, I., Bertoluzzi, L., Gonzalez-Pedro, V., Gimenez, S., Fabregat-Santiago, F., Kemp, K. W., Sargent, E. H., Bisquert, J. *Nat. Commun.* **2013**, *4*, 2272.
143. Urban, J., J., Milliron, D. J. in *Colloidal Quantum Dot Optoelectronics and Photovoltaics*

(Cambridge, 2013).
144. Choi, J. J., Lim, Y.-F., Santiago-Berrios, M. B., Oh, M., Hyun, B.-R., Sung, L., Bartnik, A. C., Goedhart, A., Malliaras, G. G., Abruna, H. D., Wise, F.W., Hanrath, T. *Nano Lett.* **2009**, *9*, 3749–3755.
145. Willis, S. M., Cheng, C., Assender, H. E., Watt, A. A. *Nano Lett.* **2012**, *12*, 1522–1526.
146. Deng, X., Schiff, E. A. *in Amorphous silicon based solar cells*, (Wiley, 2003).
147. Chenvidhya, D., Kirtikara, K., Jivacate, C. *Solar Energy Materials and Solar Cells* **2005**, *86*, 243–251.
148. Rockett, A. in *The Materials Science of Semiconductors* (Springer, 2007).
149. Li, J. V., Halverson, A. F., Sulima, O. V., Bansal, S., Burst, J. M., Barnes, T. M., Gessert, T. A., Levi, D. H. *Solar Energy Materials and Solar Cells* **2012**, *100*, 126–131.
150. Bozyigit, D., Volk, S., Yarema, O., Wood, V. *Nano Lett.* **2013**, *13*, 5284–5288.
151. Pingree, L. S. C., Reid, O. G., Ginger, D. S. *Adv. Mater.* **2009**, *21*, 19–28.
152. Jiang, C.-S., Friedman, D. J., Geisz, J. F., Moutinho, H. R., Romero, M. J., Al-Jassim, M. M. *Appl. Phys. Lett.* **2003**, *83*, 1572–1574.
153. Jiang, C.-S., Moutinho, H. R., Romero, M. J., Al-Jassim, M. M., Xu, Y. Q., Wang, Q. *Thin Solid Films* **2005**, *472*, 203–207.
154. Lee, J., Kong, J., Kim, H., Kang, S.-O.,Lee, K. *App. Phys. Lett.* **2011**, *99*, 243301.
155. Saive, R., Scherer, M., Mueller, C., Daume, D., Schinke, J., Kroeger, M., Kowalsky, W. *Adv. Funct. Mater.* **2013**, *23*, 5854–5860.
156. Mathijssen, S. G., Smits, E. C., van Hal, P. A., Wondergem, H. J., Ponomarenko, S. A., Moser, A., Resel, R., Bobbert, P. A., Kemerink, M., Janssen, R. A., de Leeuw, D. M. *Nat. Nanotechnol.* **2009**, *4*, 674–680.
157. Nichols, J. A., Gundlach, D. J., Jackson, T. N. *Appl. Phys. Lett.* **2003**, *83*, 2366.
158. Rodovsky, D. B., Reid, O. G., Pingree, L. S., Ginger, D. S. *ACS Nano* **2010**, *4*, 2673–2680.
159. van Reenen, S., Matyba, P., Dzwilewski, A., Janssen, R. A., Edman, L., Kemerink, M. *J. Am. Chem. Soc.* **2010**, *132*, 13776–13781.
160. Jiang, C.-S., Noufi, R., Ramanathan, K., AbuShama, J. A., Moutinho, H. R., Al-Jassim, M. M. *Appl. Phys. Lett.* **2004**, *85*, 2625–2627.
161. Visoly-Fisher, I., Cohen, S. R., Cahen, D., Ferekides, C. S. *Appl. Phys. Lett.* **2003**, *83*, 4924–4926.
162. Saraf, S., Rosenwaks, Y. *Surface Science* **2005**, *574*, L35–L39.
163. Arango, A. C., Johnson, L. R., Bliznyuk, V. N., Schlesinger, Z., Carter, S. A., Hörhold, H.-H. *Adv. Mater.* **2000**, *12*, 1689–1692.
164. Zhang, J., Gao, J., Miller, E. M., Luther, J. M., Beard, M. C. *ACS Nano* **2014**, *8*, 614–622.

APPENDIX A

Supporting Information for Chapter 2

Reproduced with permission from *ACS Nano*, **2011**, *5* (10), pp 8175–8186.

DOI 10.1021/nn2033117

Supporting Information
for
The Photothermal Stability of PbS Quantum Dot Solids

Rachelle Ihly, Jason Tolentino, Yao Liu, Markelle Gibbs, Matt Law
Department of Chemistry, University of California, Irvine, Irvine, CA 92697
email: matt.law@uci.edu

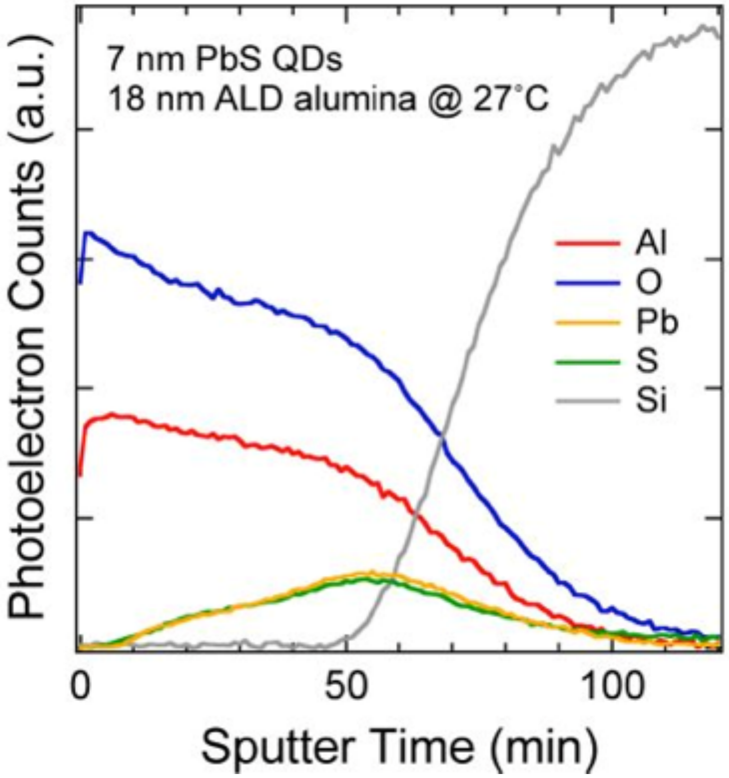

Supporting Figure 1. X-ray photoelectron spectroscopy depth profile of an ALD-infilled PbS QD film. Alumina appears throughout the film. XPS was performed using a modified Physical Electronics 5600 XPS with monochromatic Al Kα radiation and a pass energy of 29 eV.

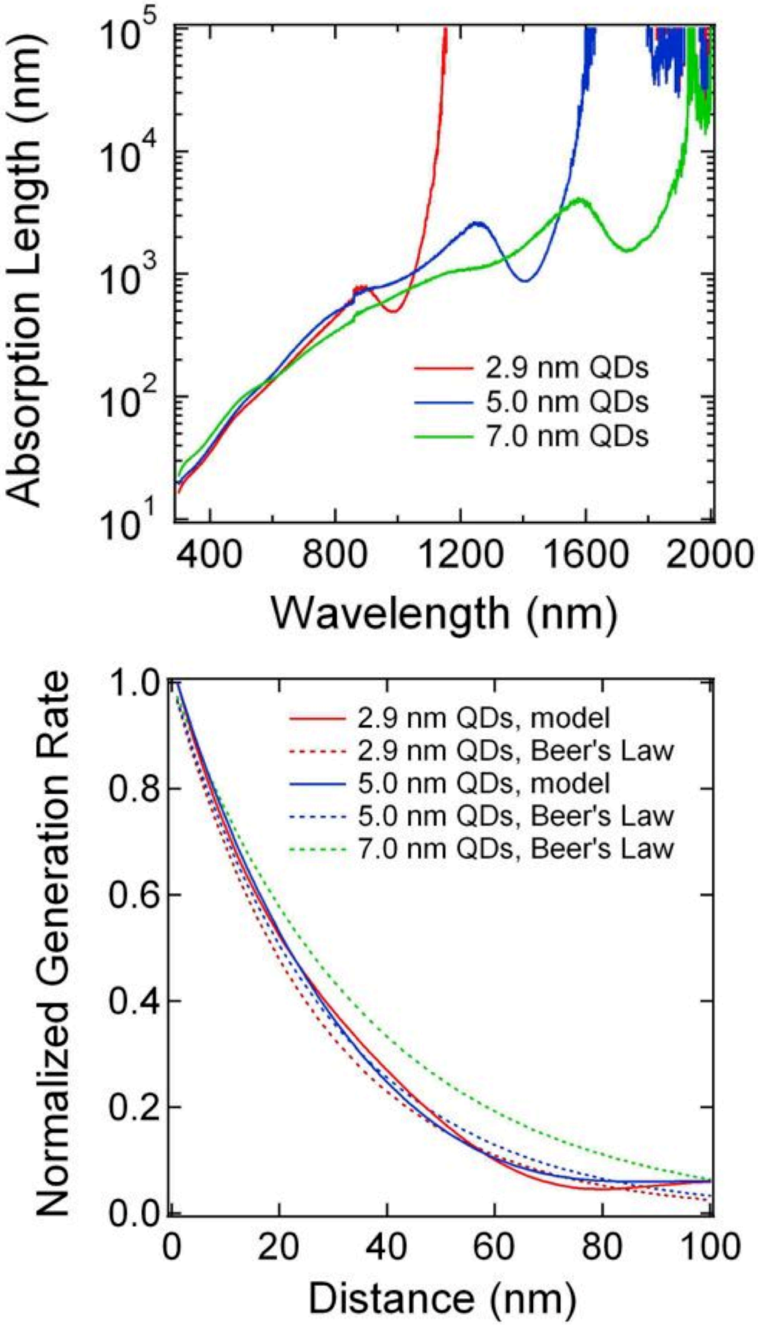

Supporting Figure 2. (*top*) Absorption lengths for EDT-treated PbS QD films as determined from integrating sphere measurements. (*bottom*) Absorption profiles for 365 nm light as calculated from a 2 × 2 scattering matrix model described in detail elsewhere.[1] Solid curves are modeling results for 100-nm thick films of 2.9 nm and 5.0 nm QDs on glass, while dashed lines are simple exponential decay profiles using absorption lengths determined from integrating sphere measurements. No model for 7.0 nm QDs is presented here because *n* & *k* values for the large QDs were not measured. The model assumes a planar air/glass/QD film/air dielectric stack with light incident through the glass substrate. It accounts for multiple reflections in the glass.

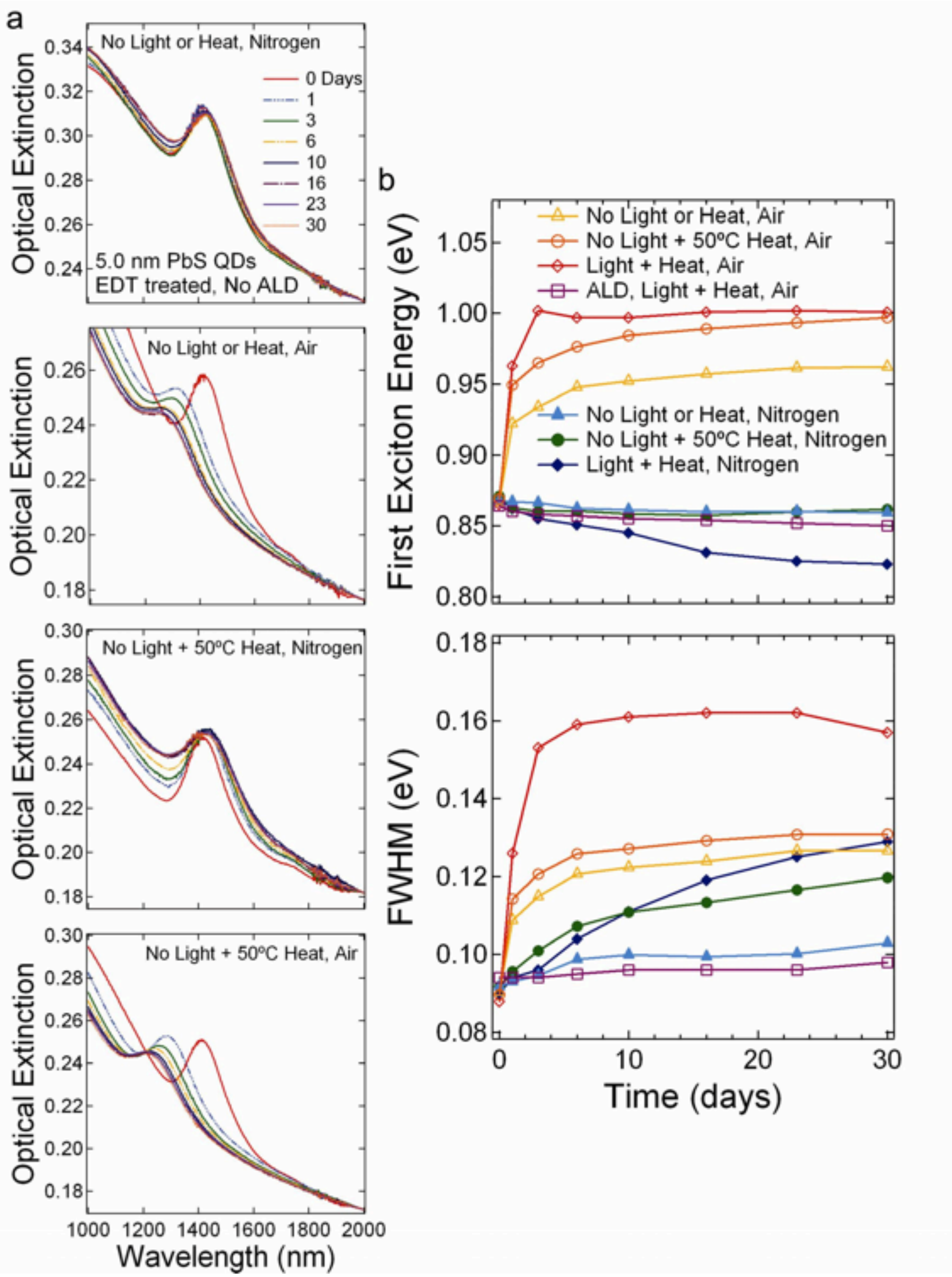

Supporting Figure 3. Controls for 5.0 nm PbS QD films. (a) Typical absorption spectra as a function of time for films in nitrogen or air either without UV light and heat or with heat alone (50°C). The traces in each graph are offset to overlay at $\lambda = 2000$ nm. (b) Time traces of the peak energy and width for all of the treatments explored in this study.

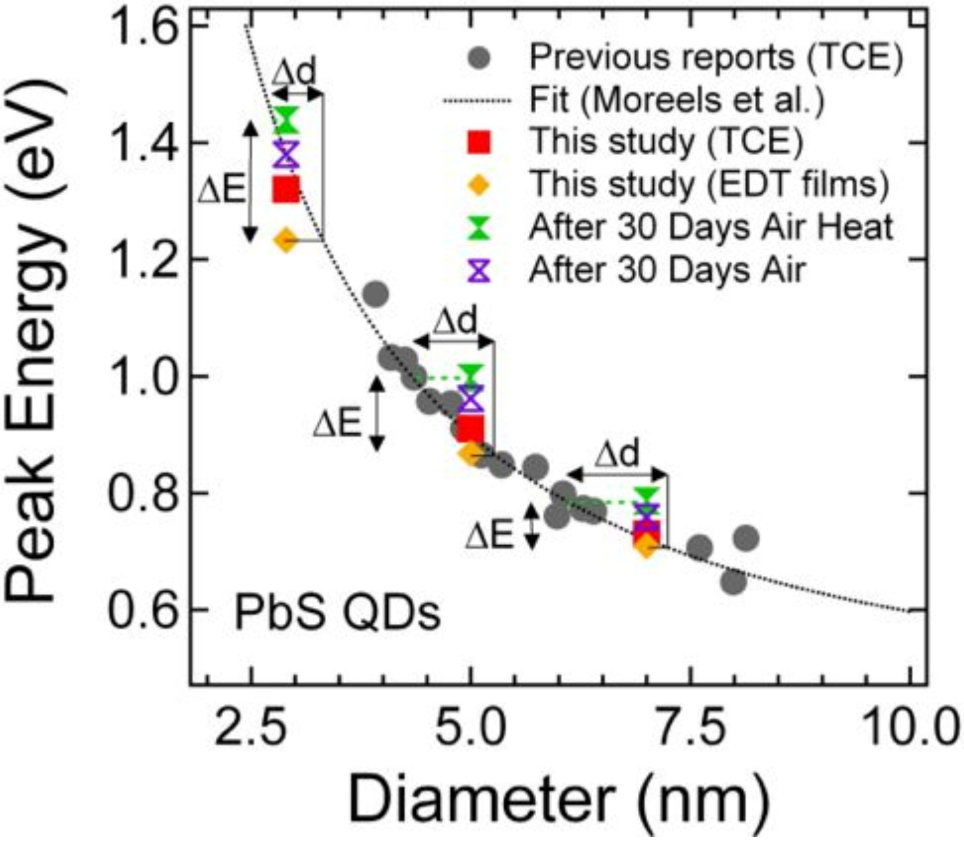

Supporting Figure 4. PbS QD sizing curve used to determine diameter changes upon thermal soaking at 50°C in air. Gray circles are oleate-capped PbS QDs in tetrachloroethylene (TCE) solution as reported by Moreels *et al.*[2] Red squares are the three QD samples used in this study, also in TCE. The dotted line is a fit to the solution data as reported by Moreels *et al.*:

$$E_g(eV) = 0.41 + \frac{1}{0.0252d^2 + 0.283d}$$

The first exciton redshifts upon formation of EDT-treated thin films (orange diamonds). After 30 days of thermal soaking in air, the exciton energy of the films blueshifts by 207 meV, 129 meV, and 77 meV for the small, medium, and large QDs, respectively (green hourglasses). These energy changes, denoted by ấE, correspond to an effective decrease of the PbS core diameter by 0.5 nm, 0.8 nm, and 1.1 nm for the small, medium, and large QDs, respectively (denoted by ấd in the figure). These estimates of ấd are lower limits because they assume (*i*) the QDs undergo no sintering and (*ii*) the effective bandgap of the oxide shell (composed of PbO, $PbSO_4$, and other species) is similar to that of oleate. Neither assumption is realistic: ripening and sintering occur simultaneously with oxidation, and the bandgap of the oxide shell is considerably smaller than that of oleate. Thus the oxide shells are likely thicker than suggested here.

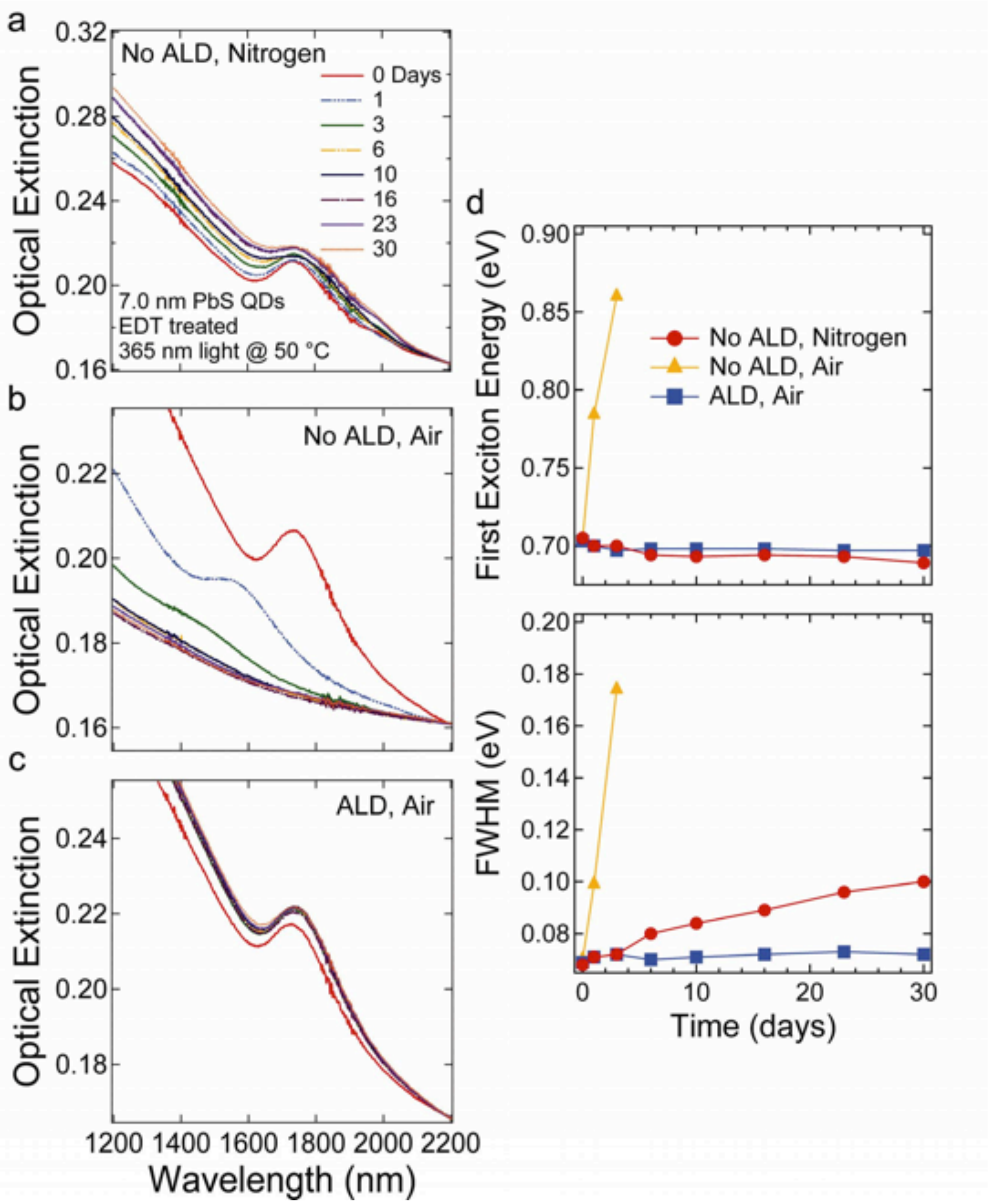

Supporting Figure 5. UV photothermal soaking of films of 7.0 nm PbS QDs in air and nitrogen. Typical optical absorption spectra as a function of time exposed to UV light (1.4 mW cm^{-2} @ 365 nm) and heat (50°C) for an EDT-treated QD film in (a) nitrogen and (b) air, as well as (c) an ALD-infilled film in air (18 nm alumina deposited at 27°C). The traces in each graph are offset to overlay at $\lambda = 2200$ nm. (d) Time traces of the first exciton peak energy and peak width for the three films. The excitonic peak of unprotected films soaked in air was completely washed out after just four days of photothermal testing. In contrast, ALD-infilled films exhibit only a slight redshift – comparable to the films soaked in nitrogen – over the first 30 days of photothermal soaking, and zero peak broadening (compared with >100 meV and ~30 meV broadening for unprotected films in air and nitrogen, respectively).

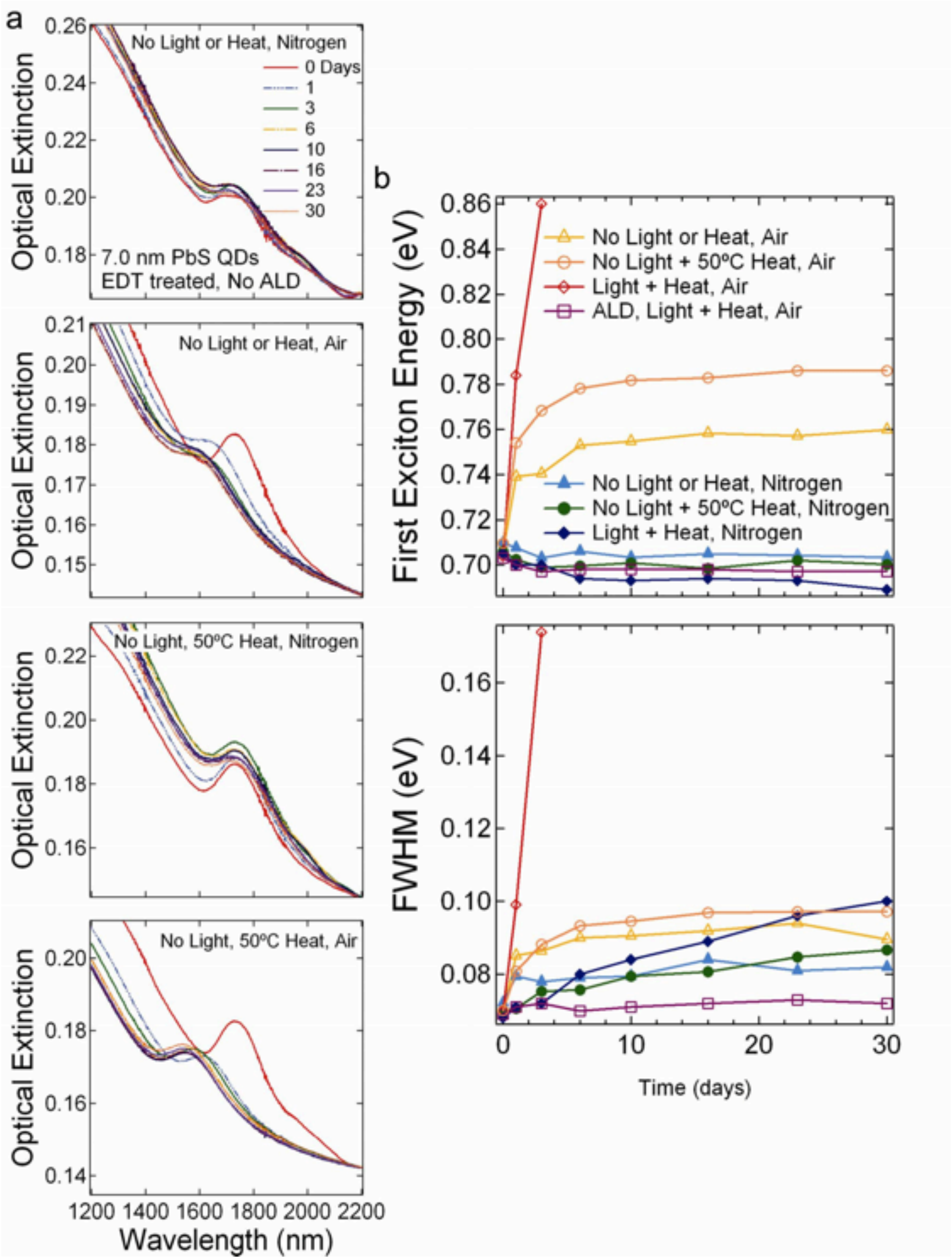

Supporting Figure 6. Controls for 7.0 nm PbS QD films. (a) Typical absorption spectra as a function of time for films in nitrogen or air either without UV light and heat or with heat alone (50°C). The traces in each graph are offset so as to overlay at $\lambda = 2200$ nm. (b) Time traces of the peak energy and width for all treatments explored in this study.

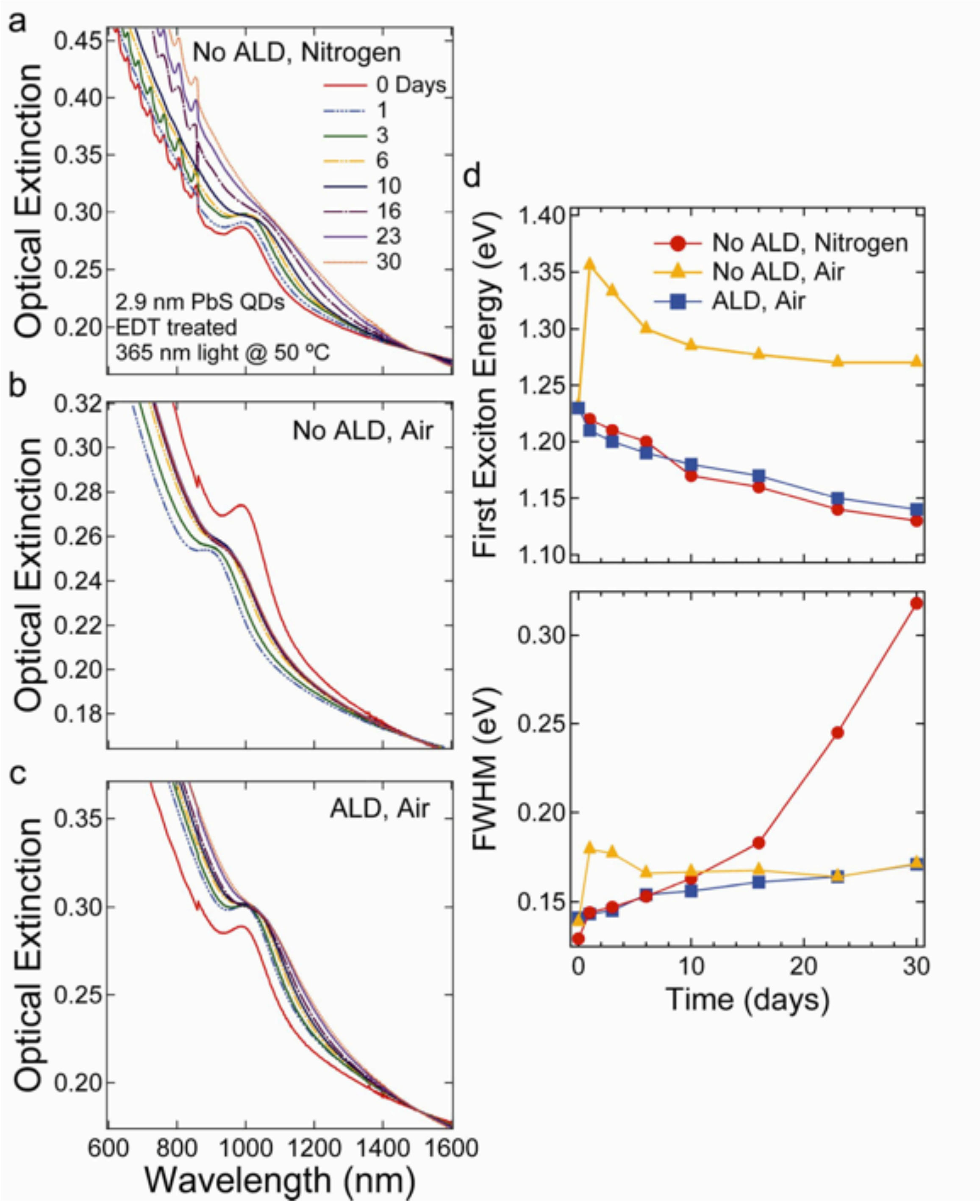

Supporting Figure 7. UV photothermal soaking of films of 2.9 nm PbS QDs in air and nitrogen. Typical optical absorption spectra as a function of time exposed to UV light (1.4 mW cm^{-2} @ 365 nm) and heat (50°C) for an EDT-treated QD film in (a) nitrogen and (b) air, as well as (c) an ALD-infilled film in air (18 nm alumina deposited at 27°C). The traces in each graph are offset to overlay at λ = 1500 nm. The oscillations in the upper panel are due to etaloning within the sample cell. (d) Time traces of the first exciton peak energy and peak width for the three films.

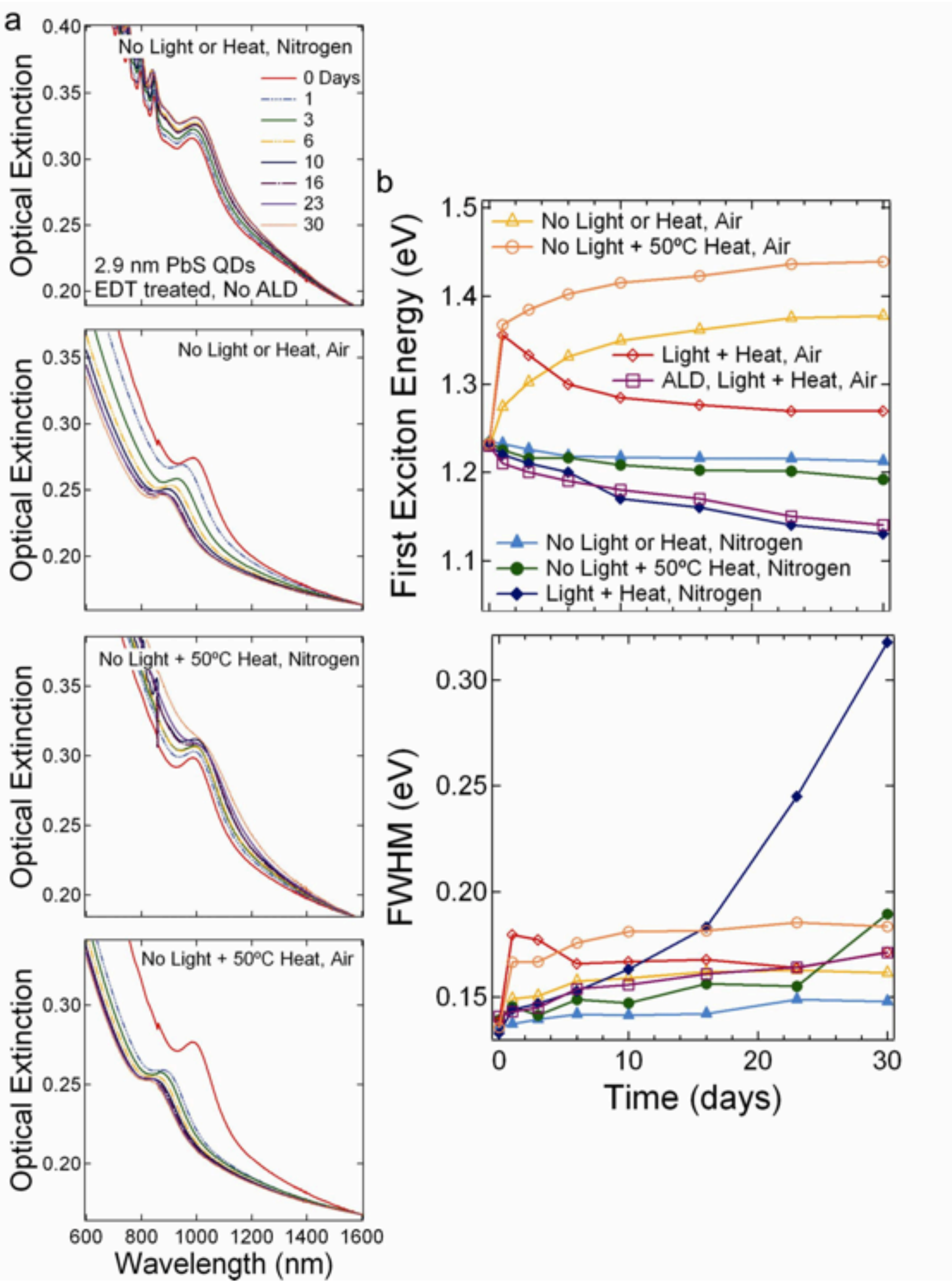

Supporting Figure 8. Controls for 2.9 nm PbS QD films. (a) Typical absorption spectra as a function of time for films in nitrogen or air either without UV light and heat or with heat alone (50°C). The traces in each graph are offset so as to overlay at $\lambda = 1600$ nm. (b) Time traces of the peak energy and width for all treatments explored in this study.

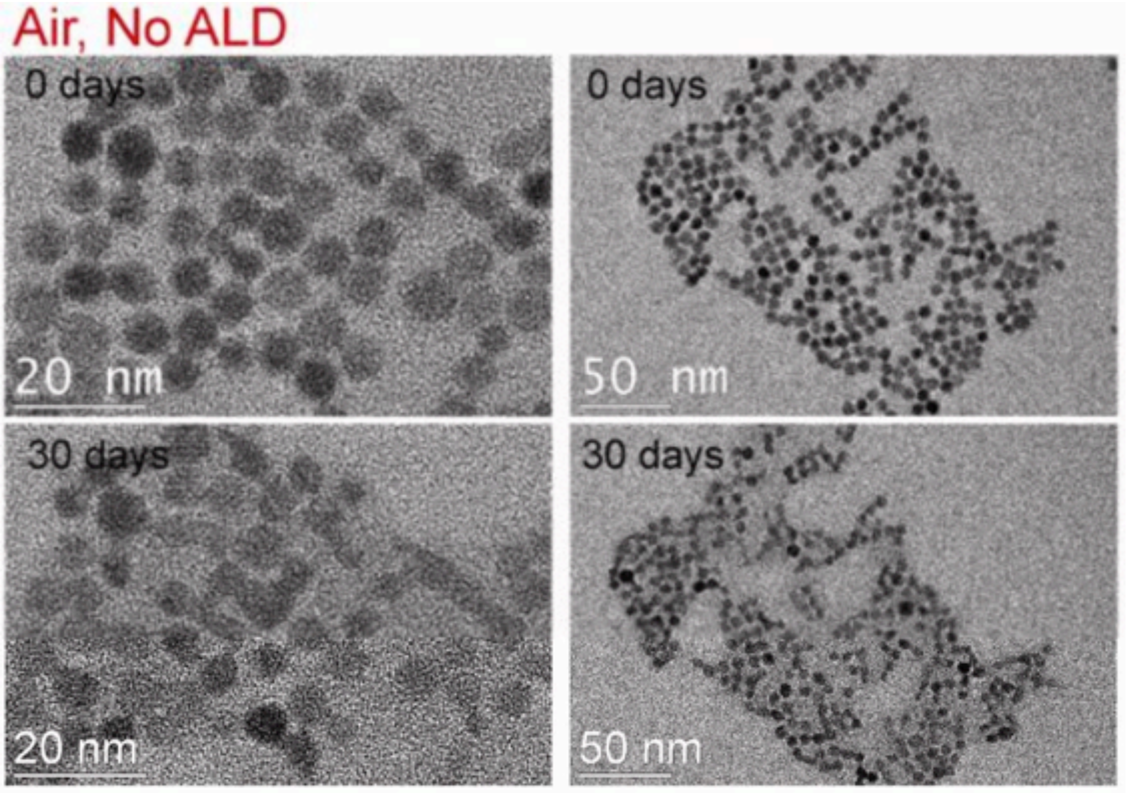
Air, No ALD
0 days
20 nm
0 days
50 nm
30 days
20 nm
30 days
50 nm

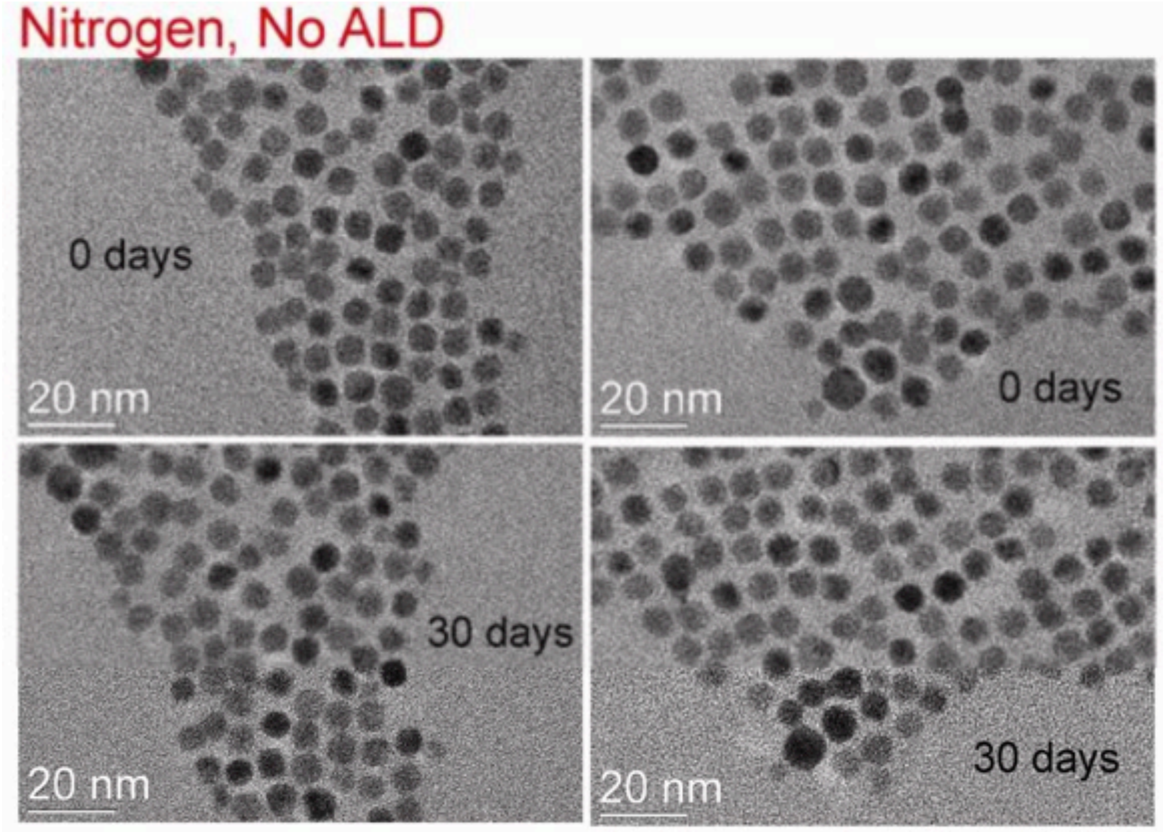

Supporting Figure 9. Additional TEM images of 7 nm QD monolayers before and after photothermal soaking.

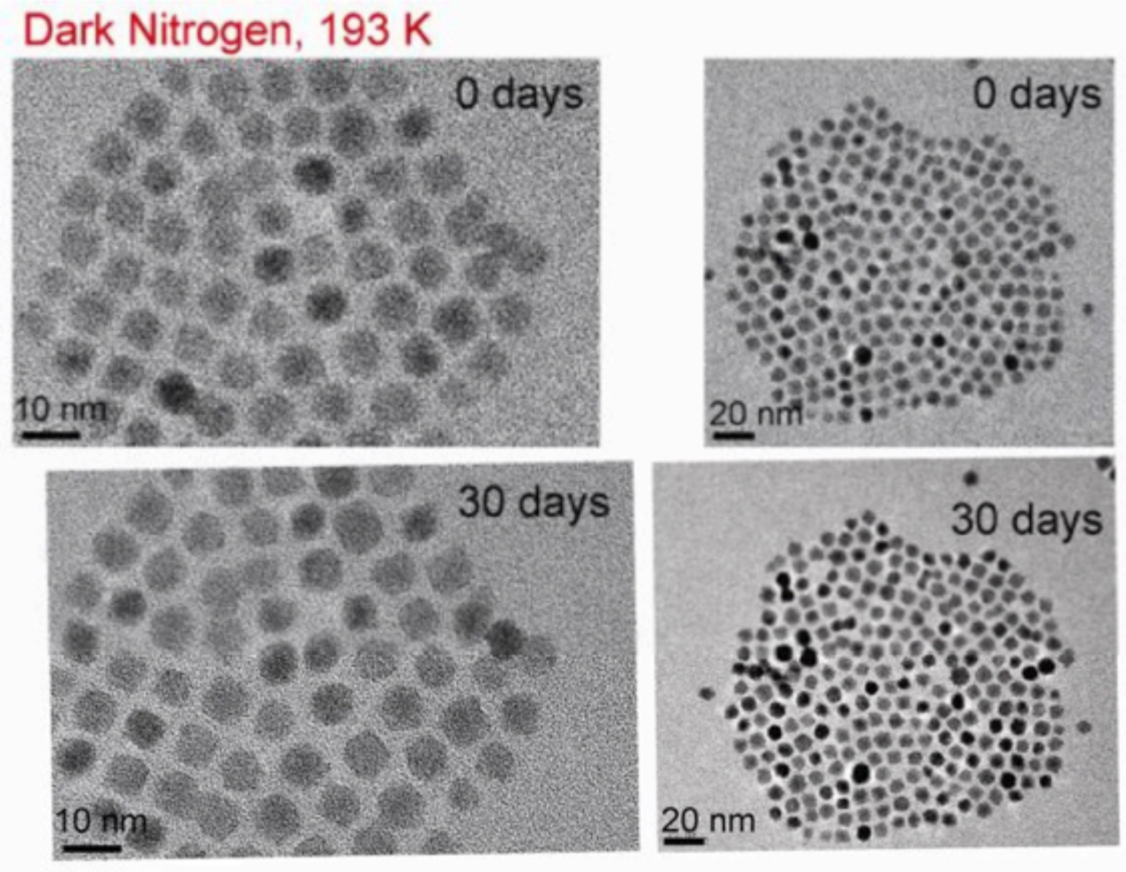
Dark Nitrogen, 193 K
0 days
10 nm
0 days
20 nm
30 days
10 nm
30 days
20 nm

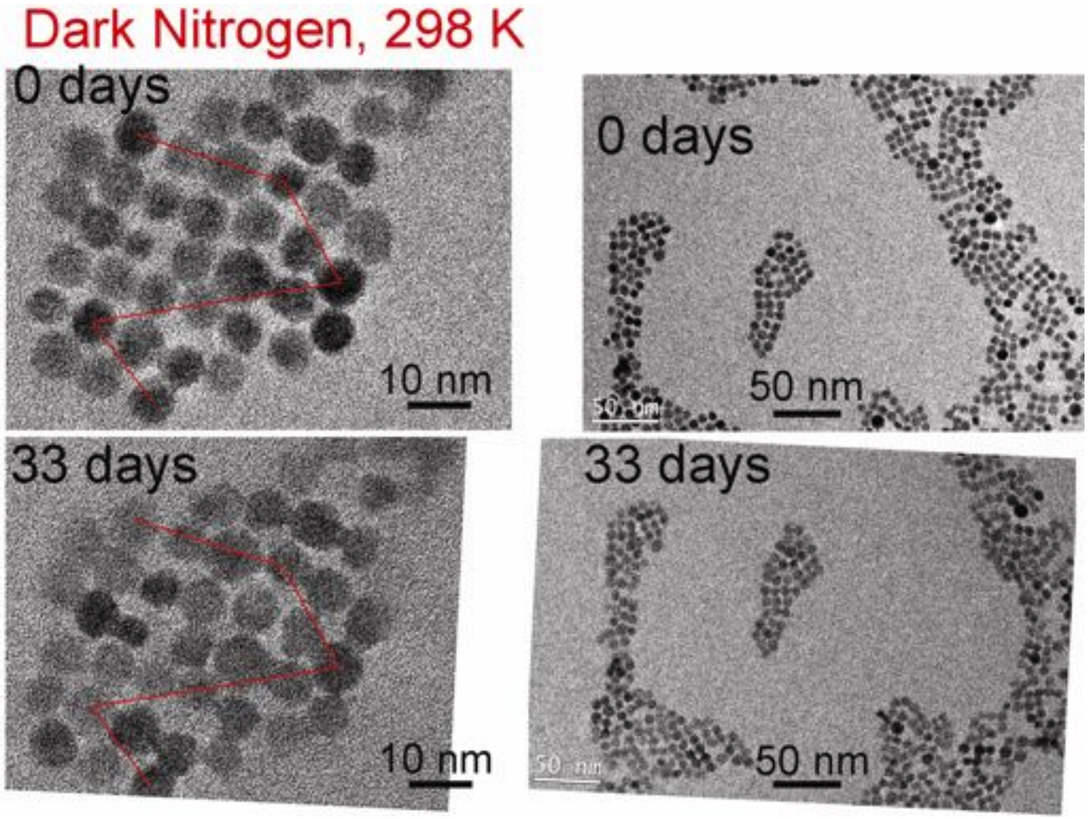
Dark Nitrogen, 298 K
0 days
10 nm
0 days
50 nm
33 days
10 nm
33 days
50 nm

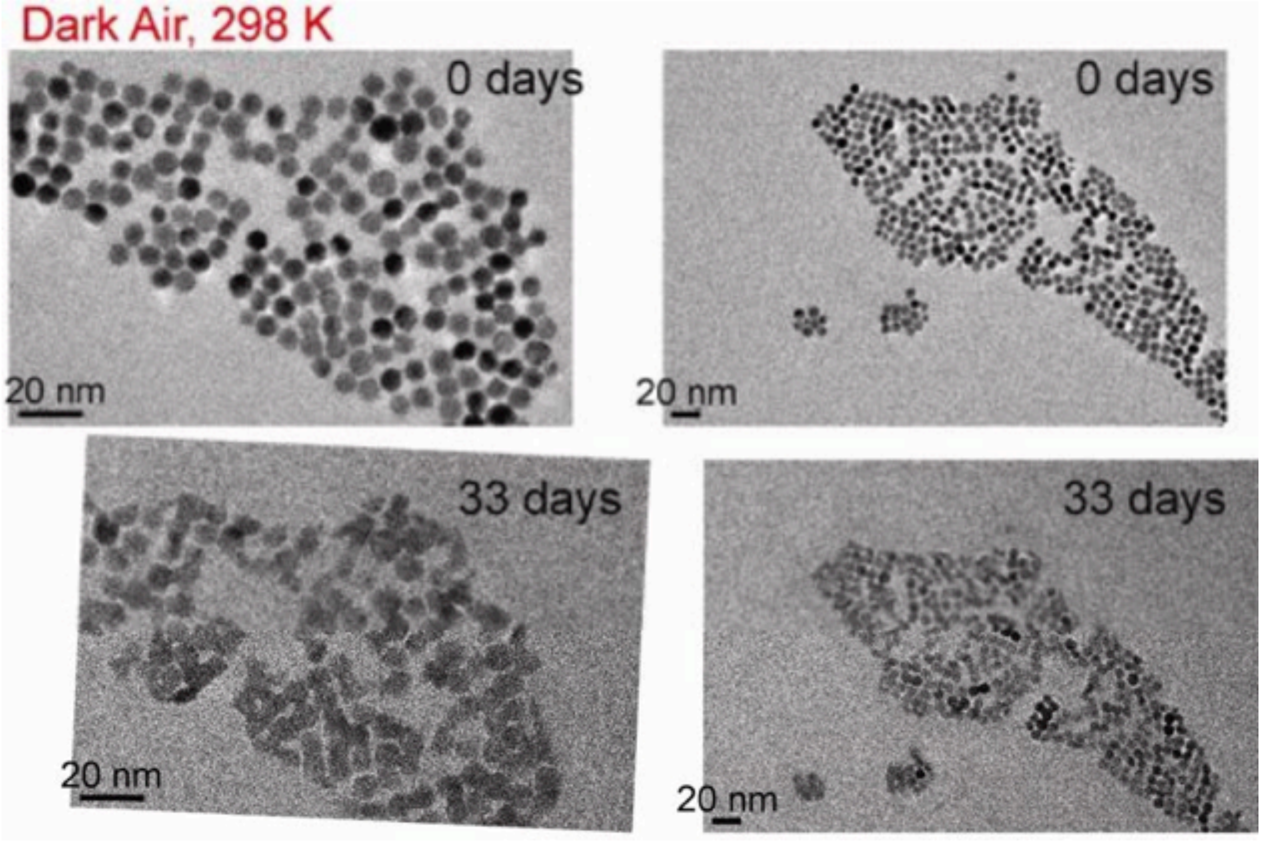

Supporting Figure 10. *Ex situ* TEM imaging of 7 nm QDs. These are control samples aged for one month in dark nitrogen at 193 K (*top*), dark nitrogen at room temperature (*middle*), and dark air at room temperature (*bottom*). Two locations are shown for each sample. The 193 K nitrogen sample does not change with age, while the QDs aged at 298 K in nitrogen seem subtly more diffuse and the air-aged QDs show dramatic morphological changes. Electron beam damage was negligible in these experiments.

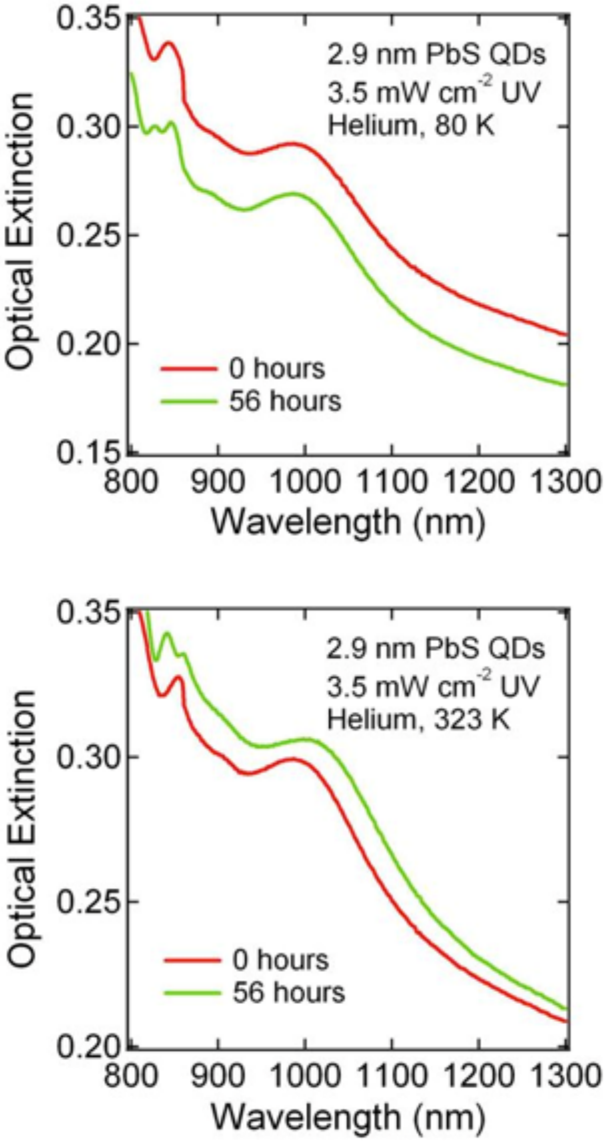

Supporting Figure 11. Photothermal soaking of 3 nm QD films in helium at 80 K and 323 K. The high-temperature film shows a redshift of the first exciton. The features at ~850 nm are interference fringes from the optical cell used in the measurements.

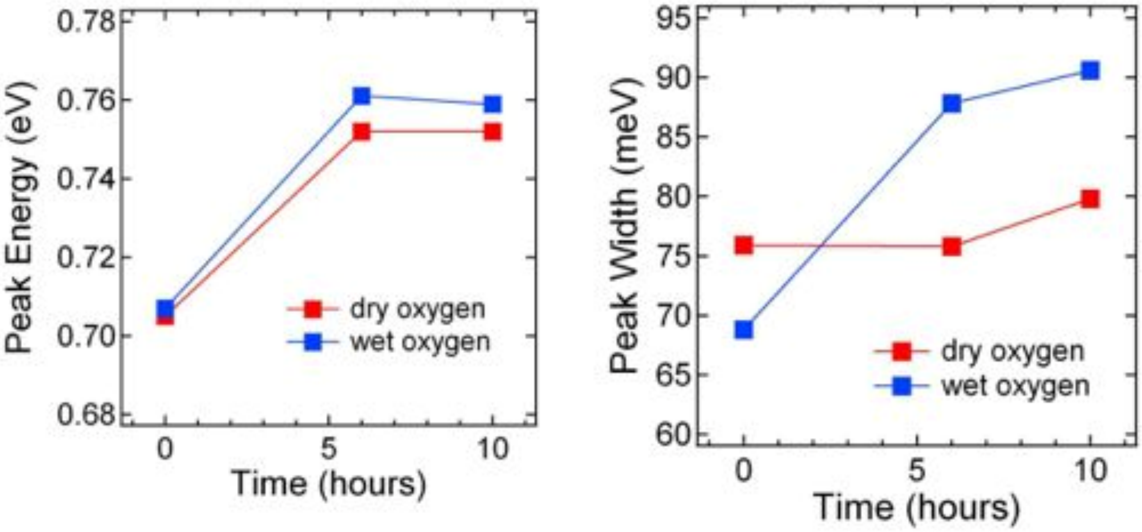

Supporting Figure 12. Comparative aging of 7 nm QD films in dry and wet oxygen. Peak energy and peak width are shown for two films UV soaked in an environmental chamber. UV soaking in wet nitrogen for similar times caused no changes in optical spectra.

References

(1) Law, M.; Beard, M. C.; Choi, S.; Luther, J. M.; Hanna, M. C.; Nozik, A. J. *Nano Lett.* **2008**, *8*, 3904-3910.

(2) Moreels, I.; Lambert, K.; Smeets, D.; De Muynck, D.; Nollet, T.; Martins, J. C.; Vanhaecke, F.; Vantomme, A.; Delerue, C.; Allan, G.; Hens, Z. *ACS Nano* **2009**, *3*, 3023-3030.

APPENDIX B

Supporting Information for Chapter 5

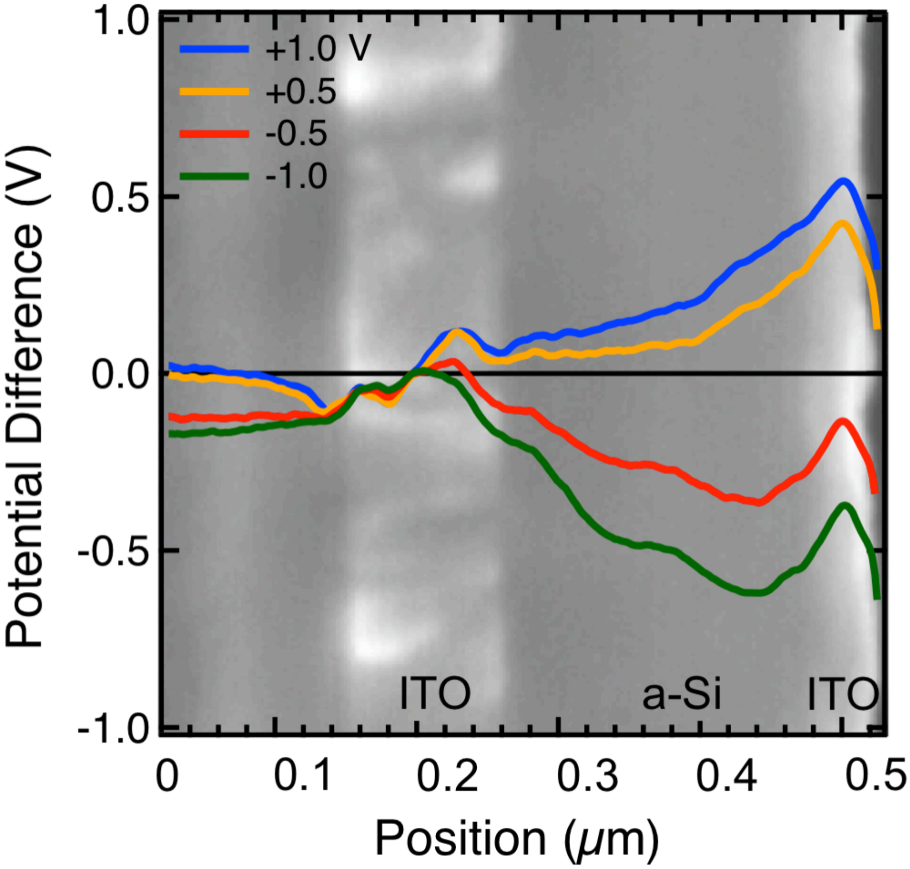

Supporting Figure 1. SKPM profiling of a *p-i-n* amorphous silicon solar cell cross-section. The potential is uniformly distributed throughout the entire amorphous silicon layer (a-Si).

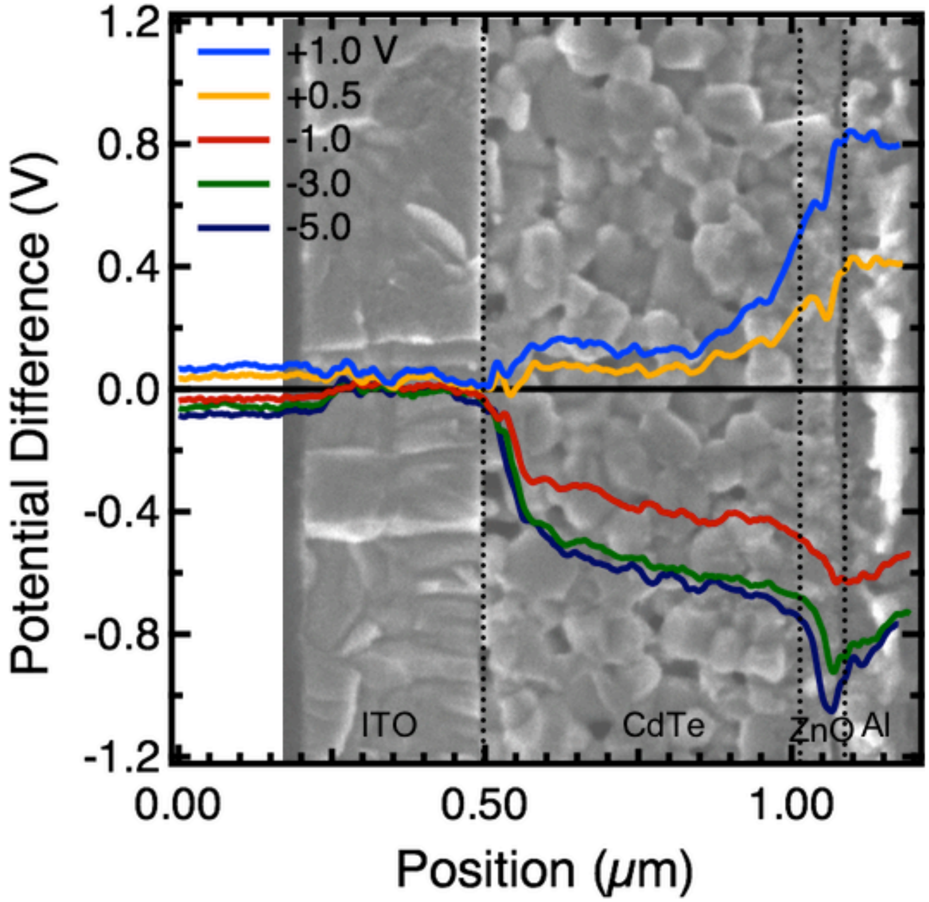

Supporting Figure 2. SKPM profiling of a CdTe/ZnO heterojunction solar cell cross-section. The device stack consists of the following: ~300 nm ITO, ~500 nm bulk CdTe, ~60 nm ZnO, and ~100 nm of Al. Dashed lines have been added for clarity to demarcate interfaces. The sloping at the CdTe/ZnO junction in forward bias locates the p-n heterojunction. The sloped region potential of the CdTe layer represents the depletion region.

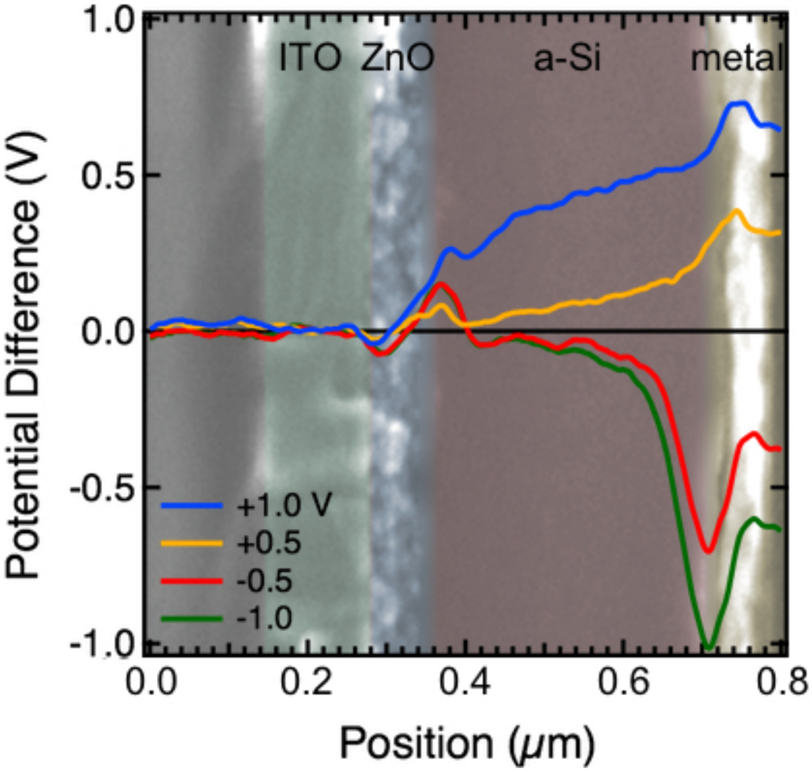

Supporting Figure 3. SKPM profiling of a ZnO/a-Si heterojunction solar cell cross-section. The PbS QD layer was substituted for a ~200-nm thick intrinsic amorphous silicon layer. The ZnO NC layer was ~ 65 nm and the metal contact consists of 15 nm MoOx and ~100 nm Al. The potential drop is primarily located near the contacts rather than the a-Si layer (except at an applied voltage of +1.0 V).